eXPRESS Polymer Letters Vol.8, No.11 (2014) 790
Available online at www.expresspolymlett.com
DOI: 10.3144/expresspolymlett.2014.81

Editorial corner – a personal view
Polymer matrix hybrid composites: The efficient way of improved performance

L. Mészáros[*]

Department of Polymer Engineering, Faculty of Mechanical Engineering, Budapest University of Technology and Economics, Műegyetem rkp. 3., H-1111, Budapest, Hungary

The research of hybrid composites is a promising and innovative subject in the field of materials science. Hybrid systems by definition contain at least two, structurally different, units performing the same task, but which together exhibit some synergy with respect to a simple combination of these units.

What is the main difference between a commonly used micro fibre reinforced polymer composite and a hybrid one? In the former one usually two separated phases are present namely the matrix (responsible for reinforcement's embedding and toughness) and the reinforcing material (providing the desired strength). The result of this combination is a high strength engineering material with acceptable toughness. At hybrid composites a third phase is also present therefore three basic types of hybrid systems can be envisioned. One is when the matrix is hybridised. For instance there is an intensive research on rubber filled thermoset resins (DOI: 10.1007/s10853-012-6564-2); but the combination of two resins could also be effective (DOI: 10.3311/PPme.7237). At this combination the purpose is usually to increase the mentioned moderate toughness. The second way of hybridization is when there are at least two kinds of reinforcing materials (e.g. DOI: 10.1177/0731684413516393) and the third one when both the matrix and the reinforcing material are hybridised (DOI: 10.1016/j.radphyschem.2011.11.015).

What are the main difficulties that obstruct the extensive use of this type of materials? One is that hybrid structures contain at least three phases, which makes the correlation between the structure and the mechanical properties much more complex compared to the well-known two phase systems. Additionally in case of hybrid matrix, the formed morphology depends on several parameters and also the reinforcing material has to be considered. The cost of hybrid composite production due to their complexity is also higher compared to general purpose composites, as typically additional technological steps are necessary. As hybrid composites are relatively new group of materials their long term performance and cyclic behaviour have to be examined, too. It should also be mentioned that at the end of the life cycle the recycling of the hybrid parts can be carried out usually on low level (energy recovery) as the separation of constituent materials is not easy. Only one exception is available, when all of the components are from biodegradable materials. These materials will have great future in the field of biotechnology especially as human implants.

Significant part of the research has to address solving of the above mentioned problems in order to make these hybrid materials available for everyday use. In the near future detailed investigation is needed on their structural and mechanical behaviour and it is also relevant to manage their reproducible production and recycling.

Dr. László Mészáros
Member of Executive Editorial Board

[*]Corresponding author, e-mail: meszaros@pt.bme.hu

eXPRESS Polymer Letters Vol.8, No.11 (2014) 791–808
Available online at www.expresspolymlett.com
DOI: 10.3144/expresspolymlett.2014.82

Polyhydroxyalkanoate (PHA): Review of synthesis, characteristics, processing and potential applications in packaging

E. Bugnicourt[1], P. Cinelli[2], A. Lazzeri[2], V. Alvarez[3]*

[1]Innovació i Recerca Industrial i Sostenible (IRIS), Parc Mediterrani de la Tecnologia Avda. Carl Friedrich Gauss No. 11, 08860 Castelldefels (Barcelona), Spain
[2]UdR Consortium INSTM - Department of Civil and Industrial Engineering, University of Pisa, Largo Lucio Lazzarino 1, 56126 Pisa, Italy
[3]INTEMA, Composite Materials Group (CoMP), Engineering Faculty, National University of Mar del Plata, Juan B. Justo 4302 (B7608FDQ) Mar del Plata, Argentina

Received 5 February 2014; accepted in revised form 4 June 2014

Abstract. Polyhydroxyalkanoates (PHAs) are gaining increasing attention in the biodegradable polymer market due to their promising properties such as high biodegradability in different environments, not just in composting plants, and processing versatility. Indeed among biopolymers, these biogenic polyesters represent a potential sustainable replacement for fossil fuel-based thermoplastics. Most commercially available PHAs are obtained with pure microbial cultures grown on renewable feedstocks (i.e. glucose) under sterile conditions but recent research studies focus on the use of wastes as growth media. PHA can be extracted from the bacteria cell and then formulated and processed by extrusion for production of rigid and flexible plastic suitable not just for the most assessed medical applications but also considered for applications including packaging, moulded goods, paper coatings, non-woven fabrics, adhesives, films and performance additives. The present paper reviews the different classes of PHAs, their main properties, processing aspects, commercially available ones, as well as limitations and related improvements being researched, with specific focus on potential applications of PHAs in packaging.

Keywords: *biodegradable polymers, biopolymers, polyhydroxyalkanoates (PHAs), polyhydroxybutyrate*

1. Introduction

Biopolymers or organic plastics are a form of plastics derived from renewable biomass sources such as vegetable oil, starch, proteins etc, unlike fossil-fuel plastics which are derived from petroleum. Biopolymers provide the dual advantages of conservation of fossil resources and reduction in CO_2 emissions, which make them an important innovation of sustainable development.

In recent years more and more biopolymers have been studied by researchers revealing a large range of possible sources from which they can be obtained and an increasing range of applications that bio plastic produced from them can fulfil. The possible sources range from different types biomass (Figure 1) including proteins (from animal and vegetal sources which are gaining interest due to their high functionality and excellent properties) [1] lipids and polysaccharides (e.g. starch and cellulose based biopolymers).

Others include bio-based polymers obtained from bio-derived monomers, e.g. from corn, which are then polymerized through standard routes. This is the case for biopolyesters such as polylactic acid

*Corresponding author, e-mail: alvarezvera@gmail.com

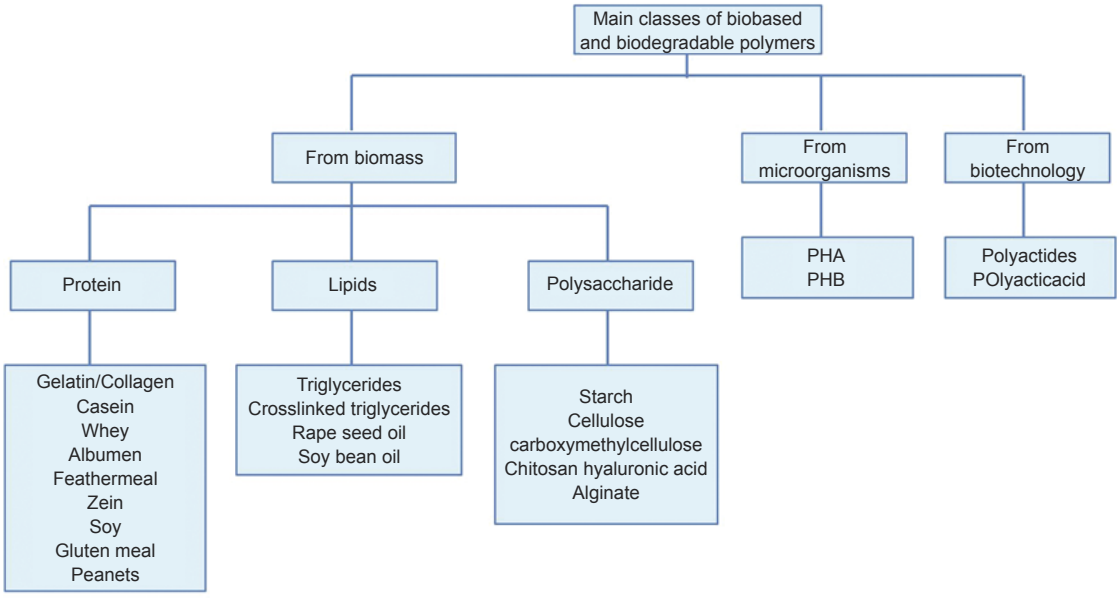

Figure 1. Different classes of polymers which are biobased and biodegradable (therefore not including biodegradable plastics from petrochemical resources and non biodegradable partly or fully biosourced plastics)

(PLA), until recently the most widely available biopolymer on the market, and set to be out ranked by bio-based polyethylene therephtalate (PET) or polyethylene (PE), among others, also obtained via a similar synthesis route. In contrast, polyhydroxyalkanoates (PHAs) are biogenic polyesters that can be naturally accumulated in microbial cultures.

Among this latter category, obtained via so called bio-refineries, *algae* serve as an excellent pathway for plastic production owing to their numerous advantages such as high yield and the ability to grow in a range of environments. Algae biopolymers mainly evolved as a by-product of algae biofuel production, where companies were exploring alternative sources of revenue in addition to those obtained from the biofuels. Moreover the use of *algae* opens up the possibility of utilizing carbon, neutralizing greenhouse gas emissions from factories or power plants. Algae based plastics have been a recent trend in the era of bioplastics compared to traditional methods of utilizing feedstock, such as starch from corn and potatoes, in polymers production, and plastic formulations.

Various processes for the cultivation of algae and production of biopolymers exist. Fundamentally, they comprise two stages: a first stage, in which algae growth is initiated and a second stage where the biopolymer accumulation is promoted. Although increasing research on the use of microalgae for such production, e.g. PHA, most studies are still at the academic level and have not yet penetrated the industry [2].

While polymers synthesized by (micro) algae are in their infancy, once they are moved into commercialization they are likely to find applications in a wide range of industries. Other possible routes for the use of algae derived monomers for subsequently synthesizing PLA are also being investigated and composites including algae derived natural fibres in their formulations are now commercially available.

Bioplastics are generating increasing interest, for industries and their market is rising as a result of technological advances and cost reductions. The advantages of bioplastics over traditional plastics are unprecedented, provided that they are used in situations in which they enable improved functionality and generate extra benefits. Biopolymers, from which bioplastics are produced, are generally more sustainable materials than their petrochemical-based counterparts, and, as previously mentioned, they can be produced from a wide range of renewable resources including more and more wastes and non-food competing sources as opposed to early biopolymers which diverted full corn fields for the production of starch as raw material for polymers production, that coupled with the production of ethanol.

The practical side of the use of biopolymers is related to the economic advantage for industries and municipalities. These consist of the saving of raw materials and the reduction in costs when the products are

finally discarded. Renewable biologically degradable products also contribute to a sustainable economy. This means that the agricultural sector obtains the possibility to get a rising percentage of its additional turnover from non-food products. After the disposal of the products, the recovered materials can be taken back by the agriculture as certificate quality-compost with economical (and ecological) advantages.

Packaging is the biggest polymer processing industry with the food sector being its principal customer. Despite environmental problems, the European polymer packaging market is increasing in the order of millions of tons per year. In the wake of future laws in relation to reducing the weight and volume of these products, cheap and biodegradable polymeric products are receiving growing attention in this market [3]. The materials used for this application often have short service time, so they end up mostly in landfills and stay there for over 100 years ([4–8]). When products, such as bags and bottles, are discarded, it is not possible in several cases, to collect them, and can end up clogging sewers and drains, and polluting streets, beaches and scenery, having a very costly impact on waste management. Plastic pollution is creating significant environmental and economic burdens since plastics deplete natural fuels (energy) and other natural resources [9]. The use of biodegradable plastics can serve as a response to this issue. This idoneous solution is well reflected by the volume of bioplastics altogether going to packaging and bottle applications nowadays, which is far greater than the average for standard plastics.

Efforts allowing the development of tailored solutions for this sector are therefore extremely relevant. Other applications include household/consumer/catering products, medical disposable devices, etc.

In such a context, although they still occupy a very limited market share, PHAs are gaining attention among biodegradable polymers due to their promising properties such as high biodegradability in different environments, not just in composting plants, and versatility. Indeed, PHAs can be then formulated and processed for use in many applications, including packaging, moulded goods, paper coatings, nonwoven fabrics, adhesives, films and performance additives. As opposed to other biopolymers, for example due to their good thermomechanical and barrier properties, PHAs offer great potential for packaging applications. Their properties, capacities for deriving a range of compounds with variable behaviour, processability, as well as the state of academic developments and current shortcomings, commercially available products and applications are reviewed hereafter.

2. Polyhydroxyalkanoate polymers

Due to their previously discussed benefits, interest in biodegradable polymers produced from renewable resources has increased significantly in recent years. Polyhydroxyalkanoate polymers are naturally produced by bacteria in general cultivated on agricultural raw materials. They can be processed to make a variety of useful products, where their biodegradability and naturalness are quite beneficial in particular for application in single use packaging and agriculture.

Poly(3-hydroxybutyrate) (PHB), Figure 2a, is a homopolymer of 3-hydroxybutyrate and is the most widespread and best characterized member of the polyhydroxy-alkanoate family. Other members of family are displayed in Figures 2b and 2c.

Poly-3-hydroxybutyrate (PHB) is a linear polyester of D (-)-3-hydroxybutyric acid which was first discovered in bacteria by Lemoigne in 1925. It is accumulated in intracellular granules by a wide variety of Gram-positive and Gram-negative organisms under conditions of a nutrient limitation other than the carbon source [10]. The molecular weight of PHB differs depending on the organism, conditions of growth and method of extraction, and can vary from about 50 000 to well over a million. The polymer possesses the important properties of thermoplasticity and biodegradability in compost and different environments comprising marine water, and, in consequence, has attracted considerable commercial interest.

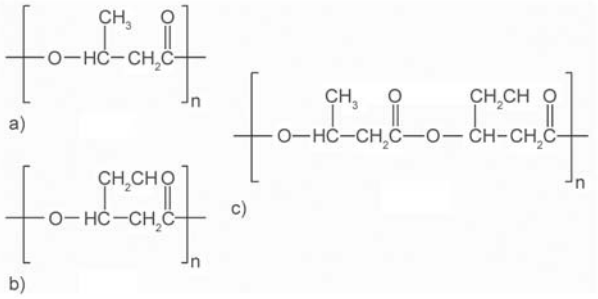

Figure 2. Chemical structure of some polyhydroxyalkanoates, a) PH3B, b) PHV, c) PHBV

PHB is apparently produced by microorganisms (such as *Ralstonia eutrophus* or *Bacillus megaterium*) in response to conditions of physiological stress and can be produced either by pure culture than mixed culture of bacteria [11]. The polymer is primarily a product of carbon assimilation (from glucose or starch) and is employed by microorganisms as a form of energy storage molecule to be metabolized when other common energy sources are not available. Microbial biosynthesis of PHB starts with the condensation of two molecules of acetyl-CoA to give acetoacetyl-CoA, which is subsequently reduced to hydroxybutyryl-CoA. This latter compound is then used as a monomer to polymerize PHB.

Biologically produced, polyhydroxybutyrate (PHB) is a semicrystalline isotactic stereo regular polymer with 100% R configuration that allows a high level of degradability [12]. PHB is presented here as an example of how new technology, derived from nature but not exploited until recently, can contribute to meeting societal needs for plastics and a clean environment.

2.1. General properties of polyhydroxyalkanoates

PHAs polymers are thermoplastic and they differ in their properties depending on their chemical composition (homo-or copolyester, contained hydroxy fatty acids). Some grades of additivated PHB are similar in their material properties to polypropylene (PP), and offer good resistance to moisture and aroma barrier properties. Polyhydroxybutyric acid synthesized from pure PHB is relatively brittle (i.e. elongation at break typically below 15%) and stiff (i.e. *E* modulus above 1 GPa). For example, mechanical properties of specimen prepared with PHB Biomer LoT13 without any additive were reported (original data from the authors). PHB is a fragile material due to re-crystallization with ageing at room temperature as will be extensively reported in following sections. Thus mechanical properties change with time and, as reported in the example, samples stored at room temperature for 60 days have lower values for elongation at break than samples stored for 30 days. For these reasons, efforts in compounding PHB are mainly focused on the search of plasticizers and nucleating agents capable of reducing the crystallization process and improving flexibility and elongation in the final product. Figure 3 shows the stress/strain of PHB (H) samples stored at 50% RH for respectively 30 (HC30d) and 60 days (HC60d), and stored at low temperature (HR) (5°C).

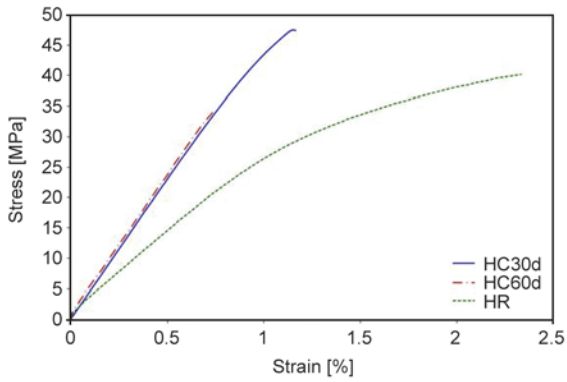

Figure 3. Stress/strain of PHB (H) samples stored at 50% RH for respectively 30 (HC30d) and 60 days (HC60d), and stored at low temperature (HR) (5°C)

Some of the general characteristics of PHAs are summarized in the following paragraphs:

- Water insoluble and relatively resistant to hydrolytic degradation.
- Good ultra-violet resistance but poor resistance to acids and bases.
- Soluble in chloroform and other chlorinated hydrocarbons.
- Biocompatible and hence suitable for medical applications.
- Sinks in water, facilitating its anaerobic biodegradation in sediments.
- Nontoxic.
- Less 'sticky' than traditional polymers when melted.

The average properties of PHA's are summarised in Table 1.

Table 1. Range of typical properties of PHA's

Property* [units]	Values
T_g [°C]	2
T_m [°C]	160–175
X_{cr} [%]	40–60
E [GPa]	1–2
σ [MPa]	15–40
ε [%]	1–15
WVTR [g·mm/m^2·day]	2.36
OTR [cc·mm/m^2·day]	55.12

*T_g: glass transition temperature, T_m: melting temperature, X_{cr}: crystallinity degree, *E*: Young's modulus, σ: tensile strength, ε: elongation at break, WVTR: water vapour transmission rate; OTR: oxygen transmission rate.

2.2. Thermal and mechanical properties of polyhydroxyalkanoates

Isostatic PHB displays a number of properties comparable to petroleum-based polymers (e.g., polypropylene), such as high melting temperature (175°C) and relatively high tensile strength (30–35 MPa). However, pure PHB has had only limited use mainly because of its intrinsic brittleness (presenting low strain at break) and the narrow processing window of this plastic. Indeed, the elongation at break is very different between PHB (5%) and PP (400%). PHB/V (polyhydroxybutyrate/valerate) is also brittle, its elongation at break is less than 15%, its modulus and fracture stress are 1.2 GPa and 25 MPa [13]. There are many reasons for the brittleness of PHB and PHB/V: the secondary crystallization of the amorphous phase takes place during storage at room temperature; the glass transition temperature (T_g) of PHB is close to room temperature; PHB has a low nucleation density, therefore large spherulites exhibit inter-spherulitic cracks. Several authors ([14, 15]) have examined secondary crystallization, which occurs during storage time at room temperature. Due to its natural origin, PHB is free of heterogeneities, like catalyst residues or other impurities that can act as heterogeneous nuclei, promoting the onset of crystallization [16]. This affects the crystallization kinetics of the polymer, which often starts from homogeneous nuclei, unless specific nucleating agents are added. The slow crystallization kinetics of PHB permits to tune the crystallinity level, which, in turn, is expected to affect also the rigid amorphous chains coupled with the crystals. By the addition of a nucleating agent, the number of small spherulites increases. It is reported that the rigid amorphous fraction of low-molar-mass PHB of 5 kDa is only 5–10%, and at best half of that of high-molar-mass PHB of almost 500 kDa, despite identical crystallinity. The larger rigid amorphous fraction and higher degree of reversible melting and crystallization in PHB of high molar mass, consistently and independently, is attributed to enhanced covalent coupling of crystals and amorphous structure, and/or de-coupling of segments of macromolecules which traverse between phases, respectively [17]. Molecule segments in the amorphous phase exhibit a reduced mobility if they are covalently connected with the crystalline phase.

This part of the amorphous phase is commonly named rigid amorphous fraction (RAF) that was reported to be around 20–30% of the overall sample mass ([17–19]), The kinetics of vitrification of the RAF of PHB was quantified upon quasi-isothermal cold crystallization at 22.8°C, and it was found that the whole RAF of PHB is established during crystallization [20] In a recent study, it was proven that the physical state of the amorphous layer in contact with the growing crystals influences the mechanism of crystallization of PHB. During heating of an initially amorphous PHB, the rigid amorphous fraction, which is established simultaneously with formation of the crystals during the first stage of cold crystallization, slows down further crystal growth, which can proceed only upon further increase of the temperature, when complete mobilization of the RAF is achieved [19].

On addition of plasticizers, the molecular motion is enhanced, and the glass transition is lowered. To achieve high elongation at break and a higher flexibility for modified/formulated PHB, the glass transition temperature must reach lower value than the testing temperature. The elongation and impact strength depend on the T_g as well as the morphology. In the blends, the nucleation rate and spherulite size depend on the cooling rate and nucleation density, i.e., fast cooling after melting increases the crystallization rate. That forms fine spherulites and suppresses crystallinity. This is required for the achievement of the necessary mechanical properties.

Moreover, PHB thermally decomposes at temperatures just above its melting point. A short exposure of PHB to temperature near 180°C could induce a severe degradation accompanied by production of the degraded products of olefinic and carboxylic acid compounds, e.g., crotonic acid and various oligomers: through the random chain scission reaction that involves a cis-elimination reaction of b-CH and a six-member ring transition ([21–23]).

The very low resistance to thermal degradation seems to be the most serious problem related to the processing of PHB. The main reaction involves chain scission, which results in a rapid decrease in molecular weight [24]. The most common mechanisms are summarised in Figure 4.

During processing, the degradation of the chains may be reduced by the addition of a lubricant that prevents the degradation of the chains in processing, so that the material can be processed at 170–180°C, because PHB is sensitive to high processing temperatures. This leads to a decrease in the molec-

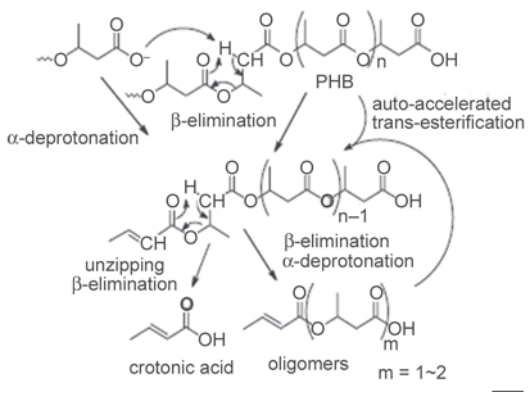

Figure 4. Mechanism of thermal degradation for PHB

ular weight, as well as a reduction in the melt viscosity. The crystallization temperature shifts to lower values, and crystallization takes longer.

In the study of thermal properties of PHB by differential scanning calorimetry (DSC) a double melting peak is reported in the literature [25] and attributed to a bimodal distribution of crystallite size resulting from changes in molecular weight due to random scission of long PHB chains that takes place at high temperatures, i.e. to the decrease in the molecular weight. PHB is also known to present irregularly shaped exotherm peaks during crystallization [26]. When the number of growing spherulites is low, the evolution of latent heat is very sensitive to every act of nucleation as well as to the space limitations in the process of growth, resulting in non-monotonous development of latent heat, with sudden increases and decreases in crystallization rates. This results in non-conventional DSC exotherms, under given crystallization conditions, characterized by spikes or shoulders associated to nucleation of new spherulites. In dynamic mechanical thermal analysis (DMTA) curves, PHB has two processes, the main one associated with glass transition reflects the motions in connection with the chains in the amorphous regions while the peak at higher temperature reflects the chain mobility between the crystalline melting and amorphous process; it depends on the thickness of the lamellae [27]. Other authors also reported that PHB possesses relaxations at 20°C and 100–150°C ([28, 29]).

One of the main approaches to improve the properties of PHB is the production of derivatives based on PHB via the biosynthesis of copolyesters containing PHB units with other 3-hydroxyalkanoates units [30], such as poly (3-hydroxybutyrate-*co*-hydroxyvalerate) (PHBV) [31] or poly (3-hydroxybutyrate-*co*-3-hydroxyhexanoate) [32], with different molar ratios of hydroxycarboxylic acids. This approach has been investigated extensively [33] because it can effectively improve mechanical properties [34] and lower the melting point, avoiding degradation during processing. However, blends with other biodegradable polymers and composites based on PHB that exclude any synthetic component are also very convenient as industrial materials due to their easier processability and lower cost ([35, 36]).

As reported above, the addition of plasticizers is considered as a relatively simple route to modify the thermal and mechanical properties of polymers. Blending polymers with plasticizers may modify the physical properties of polymers and a decrease in processing temperature can be achieved. Thus PHB is commonly blended with plasticizers and nucleation agents that lead to a lower glass temperature and lower crystallinity due to the formation of numerous, small and imperfect crystallites.

2.3. Blending of PHB with other polymers or plasticizers

Blending PHAs and in particular PHB with other polymers, or with plasticizers, may offer opportunities to improve processability by lowering the processing temperature and reducing the brittleness of PHAs based plastics. So far many blends containing PHB/PHAs have been studied and also many types of plasticizers have been proposed ([37, 38]).

The literature reports the use as plasticizers from materials that are cheap and readily available on the market, and generally also of natural origin, such as oxypropylated glycerin (or laprol), glycerol, glycerol triacetate, 4-nonylphenol, 4,40-dihydroxydiphenylmethane, acetyl tributyl citrate, salicylic ester, acetylsalicylic acid ester, soybean oil, epoxidized soybean oil, dibutyl phthalate, triethyl citrate, dioctyl phthalate, dioctyl sebacate, acetyl tributyl citrate, di-2-ethylhexylphthalate, tri(ethylene glycol)-bis(2-ethylhexanoate), triacetine, and fatty alcohols with or without glycerol fatty esters, polyethylene glycol (PEG) as well as low molecular weight polyhydroxybutyrate since PHAs with medium chain length are elastomers with low melting point and a relatively lower degree of crystallinity ([39, 40]).

Blends produced by solvent cast polyethylene glycol resulted well compatible with PHB [30] and miscibility was reported by study with DSC for low

content of polyethylene glycol (2–5%) in PHB [41]. The thermal properties of blends of PHB with PEG400 in different proportions (2, 5, 10, 40%) prepared by the casting of polymer solutions in chloroform was investigated (Parra 06). In these blends there was an increase in the elongation at break by up to about four times versus the original elongation at break of PHB and a reduction in the tensile strength. In this paper, DSC thermograms also show two melting peaks for PHB, lightly lowered by PEG addition. This behaviour was attributed to a plasticizing effect of PEG that weakened the intermolecular forces between the adjacent polymer chains. Consequently, there was a change in free volume that reduced the melting temperatures of the system. These authors classified PEG400 as a plasticizer for PHB, due to a reduction in melting temperature of PHB in PHB/PEG blends.

Poly(3-hydrobutyrate) plasticized was prepared with dioctyl (o-)phthalate (DOP), dioctyl sebacate (DOS), and dioctyl sebacate (ATBC)(exploit) [42]. It was shown, from the DSC measurements, that only the addition of ATBC leads to an obvious decline in T_g and improves other thermal characteristics. However, it does little to improve the mechanical properties. They have also demonstrated that blending with P(3/4HB) notably improves the mechanical properties of PHB, with a good elongation at break reaching e.g. 10%. The melt flow index (MFI) test has revealed that the addition of stabilizer antioxidant 1010 and the addition of Poly (3-hydroxybutyrate-*co*-hydroxyhexanoate) PHBHHx and P(3/4HB) both enhance the thermal stability of PHB and stabilize the MFI value. A combination of ATBC, antioxidant 1010, and PHBPHBHHx or poly (3-hydrobutyrate-*co*-4-hydrobutyrate) P(3/4HB) could widen the PHB processing window.

Preliminary studies of PHB blended with PEG by extrusion outlined in this process as not having an efficient effect as a plasticizer of PEG in PHB ([2]). Tests have been reported with PHB, and polyethylene glycol PEG 400, and PEG 1500 prepared by extrusion and injection moulding for production of composites with wood fibres. It was observed that the PEG addition makes processing easier having a lubricant effect on melted PHB/wood formulations, but the PEG was not efficiently blended with PHB and with time leached to the surface and reduced its possible plasticizing effect. Moreover in these studies, the presence of PEG 1500 melting peak was observed in all the samples based on PHB with PEG 1500 suggesting that PEG 1500 is not completely compatible with PHB, as confirmed by separation observed in the samples with ageing.

In the preparation of nanocomposites of PHB with cellulose nanowhiskers (CNW) prepared through the previous dispersion of CNWs in polyethylene glycol (PEG) and subsequent incorporation of the PEG/nano whiskers dispersions into the biopolymer, it was observed that for CNW concentrations up to 0.45 wt%, the CNWs were covered by PEG, and the interaction between the PHB and the CNWs occurred preferentially with PEG ([43]). The adhesion of PEG to the natural fibres can explain the lubricating effect of PEG in the preparation of composites with PHB and natural fibres.

Acetyl tributyl citrateate is also reported as a plasticizer for PHB. It is derived from naturally occurring citric acid and non-toxic [25]. Acetyl tributyl citrateate had a weak positive influence on thermal properties of PHB in the melt, but samples with PHB should be rapidly cooled down below the melting temperature in order to obtain the best processing conditions for the desired degree of crystallization. The use of glycerol, tributyrin, triacetin, acetyltriethylcitrate, acetyltributylcitrate as plasticizers, and saccharin have been reported as nucleation agents [13]. Lubricants were glycerolmonostearate, glyceroltristearate, 12-hydroxystearate and 12-hydroxystearic acid.

The copolymer, PHB-*co*-HV (poly-3-hydroxybutyrate-*co*-3-hydroxyvalerate), exhibits increased Temperature of crystallization (T_c) as compared to the homopolymer PHB. Increasing the molecular fraction of HV monomer in the PHB-*co*-HV initially led to a decrease in the melting temperature (T_m) of the copolymer from 175.4°C to a min. of 168.5°C, at 20 mol% of HV, as it is shown in Figure 5 [44].

Subsequently, increases in the fractions of HV indicate a typical isodimorphic relationship. In a recent paper [45] two nucleating agents, heptane dicarboxylic derived HPN-68L and ULTRATALC 609, were tested to increase the T_c and reduce the time for crystallization necessary for injection moulding. HPN-68L decreased the Temperature of decomposition (T_{dec}) of the homopolymer and all copolymers by almost 50°C. However, the use of ULTRATALC609 as a nucleating agent slightly enhanced the T_{dec} and had a negligible effect on the T_{ms} of all

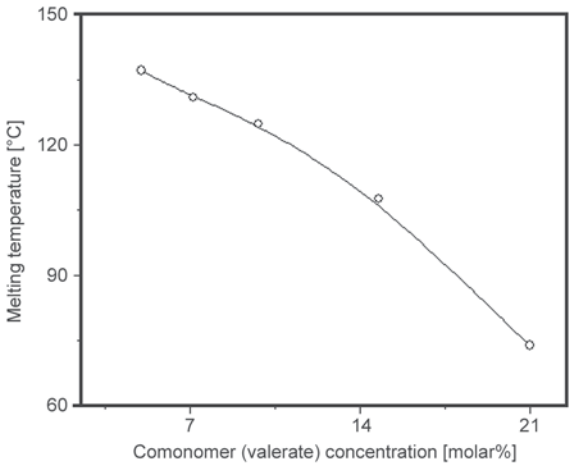

Figure 5. Effect of co monomer content [mol%] on the melting temperature of PHB-V copolymers

polymers. Also, PHB and PHB-*co*-HV with 5 wt% of talc exhibited higher T_c than polymers without ULTRATALC609. A careful comparison of T_c, T_m and T_{dec}, for PHB-*co*-HV with 20 mol% of HV indicated that this copolymer is the best option for injection moulding, with a high T_{dec}.

Organo-modified montmorillonite (OMMT) clay as nanofiller has been used in blends with PHB/V) and acetyl tri-Bu citrate as a plasticizer [46]. These nano-biocomposites show an intercalated/exfoliated structure of the nanoadditive with good mechanical and barrier properties, and an appropriated biodegradation kinetic. The presence of the OMMT clay did not influence significantly the transition temperatures. However, the filler not only acted as a nucleating agent which enhanced the crystallization, but also as a thermal barrier, improving the thermal stability of the biopolymer. Vinyl acetate homopolymer or copolymer and optionally polyvinyl alcohol are also proposed for the toughening of PHAs blends [47]. Figures 6a and 6b show the effect of different filler content on the tensile properties (modulus and strength) of PHB [2, 48].

A good strategy to modify properties of PHB/PHAs in the solid-state is blending the polyester with a second polymeric component [49]. This route has been broadly explored, testing as the other blend component a vast range of thermoplastic polymers ([50–55]). Besides changing degree of crystallinity and width of the processing window, blending also offers the opportunity oflowerng production costs, that is at present the major problem for large-scale applications of bacterial polymers based plastics. P(3HB) has been found to be miscible with various polymers, including poly(ethylene oxide) ([56]), poly(epichlorohydrin) ([57]) and poly(vinyl acetate) PVAc) [58], polyepsiol caprolactone ([54, 59]). Among polymers considered for blending with PHB there are also highly substituted cellulose esters and Tri-substituted cellulose butyrate ([60–63]).

The study of systems with immiscible binary blends with P(3HB) are also important in controlling the profile of biodegradation [64]. P(3HB)/poly(propiolactone), P(3HB)/poly(ethylene adipate) and P(3HB)/poly(3-hydroxybutyric acid-*co*-hydroxyvaleric acid) blends showed that they degrade faster than the pure components and the acceleration occurred due to the phase-separated structure [64].

Wood flour and lignin from different sources were used as fillers for the preparation of composite materials [65]. Natural fibres such as wood fibres act as load bearing constituents in the composite materials. Advantages of fibres derived from renewable resources on conventional reinforcements such as glass and aramid fibres are their relative cheapness, their ability to be recycled, and the fact that

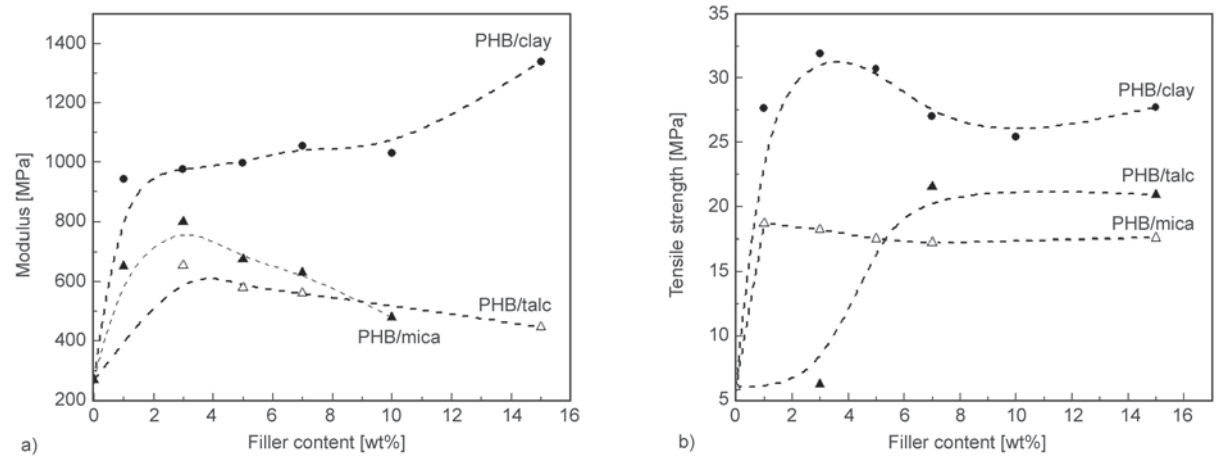

Figure 6. Effect of different filler contents on the tensile properties of PHB: a) modulus and b) strength

they can compete well with them in terms of strength per weight of material [66].

3. Processing considerations

Depending on the molecular weight of the polymer but also on the comonomer content, different processing techniques can be used (Figure 7).

PHB as a powder can be blended with additives by mixing in a Brabender (kneader) at 170–180°C and 50 rpm for 5 minutes or in a single screw extruder at a temperature in the range of 145°C (zone 1), 160°C (zone 2) and 170°C (zone 3) with 4 mm die and screw speed of 20 rpm. The strand (thread) is generally cooled in water and cut using a pelletizer. Then, the mixed material (granulates) can be compression moulded in a hydraulically heated press, commonly from 170–180°C between two sheets of Teflon for 2–5 minutes without pressure and an additional 1–3 minutes with pressure (50 bar). After moulding, the samples are cooled between cold metal plates with water. Plasticizers like glycerol, tributyrin, triacetin, acetyltriethylcitrate, acetyltributylcitrate are used in most cases. In addition, lubricants like glycerolmonostearate, glyceroltristearate, 12-hydroxystearat, and 12-hydroxystearicacid can also be used.

The different technologies that can be used for converting PHB are introduced below before an extensive discussion of the specificity of their use for processing PHB.

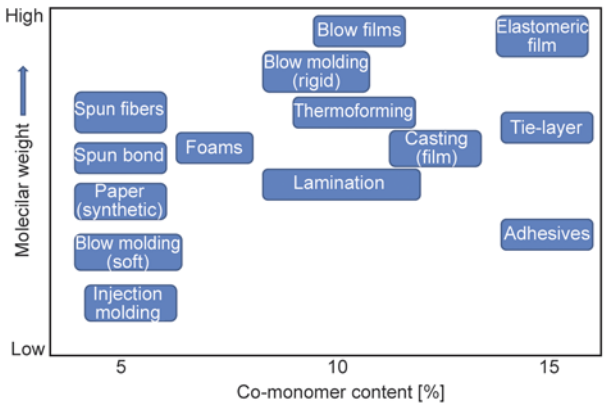

Figure 7. Adequate processing technique of different PHB copolymers, as a function of polymer molecular weight and co monomer content

3.1. Melting behaviour of PHB

PHB is a highly crystalline (60–70% crystallinity) and linear polymer and the crystallization speed is fast between 80 and 100°C but slow below 60°C or above 130°C so that the material then remains amorphous and sticky for hours. The sharp transition fluid/solid can be used to achieve very fast processing speeds. In order to obtain this it is better to melt the material right behind the filling zone and to lower its temperature towards the die. The typical viscosity for this kind of materials is similar to PP with a MFI: 30–40 g/10 min.

3.2. Pre-cleaning screw and barrel

As most materials left over in the machine after the last run have high viscosity at 130°C, they will not be displaced by the low viscous PHB. Such materials can be replaced by adding a coloured batch of a low melting temperature polymer such as PCL (polycaprolactone) or a high MFI PP.

3.3. Drying

All PHB based resins contain bound water and not only surface bound water. It is necessary to dry the pellets. Best results are obtained in dry air dryers e.g. for over 2 h at 80°C. The pellets regain the original humidity within 30 minutes after they are removed from the dryer.

4. Processing techniques and conditions

PHAs can be processed mainly via injection moulding, extrusion and extrusion bubbles into films and hollow bodies.

The thermal, rheological, mechanical and barrier properties of PHBV from various manufacturers were characterized with different valerate contents and molecular weights [67]. The use of co-polymers were chosen in order to improve the flexibility for potential packaging applications, it leads to decrease of the glass transition and melting temperatures. In addition, *the HV broadens the processing window since there is improved melt stability at lower processing temperatures*. They have observed that the complex viscosity decreased with increasing temperature due to a decrease in molecular weights of the samples. These results suggest that processing the co-polymer below 160°C would be beneficial with low screw speed. The mechanical results indicate all PHBV materials had high elastic modulus and flexural strength with low tensile strength and elongation at break. The water vapour transmission rate (WVTR) results indicated the polymer to be very hydrophilic, resulting in higher water transmission rates. The difference in valerate

content showed two melting transitions for non-commercially available PHBV co-polymers (Aldrich 5, 12 and Tianan 20%), suggesting an immiscible blend between the PHB homo-polymer and HV co-monomer. However, the thermogravimetric analysis (TGA) curves showed minimal separation between the PHB homo-polymer and PHV plasticizing units. The rheological data showed that the Tianan 5% polymer was thermally stable in the melting temperatures. However, Aldrich 5, 12% and Tianan 20% PHBV polymers were thermally unstable at temperatures higher than 160°C. This instability can be attributed to the breakdown of the polymer chain via the random chain scission process, resulting in lower molecular weight that led to decreasing complex viscosity at higher testing temperatures. The PHBV materials were brittle with high elastic modulus and low tensile strength, thus making it a strong and hard material. In addition, commercially available Tianan 5% had higher modulus of elasticity, while lower tensile strength and elongation at break compared to conventional thermoplastic used for packaging. Moreover, the water vapour transmission rate was very high compared to thermoplastic used for packaging, which is due to the wide range of processing conditions, HV units, and molecular weights.

The barrier properties of PHA are also important, the WVTR and Oxygen Transmission rate (OTR) for PHA compared with other polymers are included in Table 2.

A series of resorbable polyhydroxyacids by size exclusion chromatography (SEC), viscosity measurements, and differential scanning calorimetry (DSC) in order to understand the effect of the injection moulding process on the molecular weight and thermal properties of the polymers [68]. The studied polymers were polylactides (PLA), polyhydroxybutyrate (PHB) and poly-hydroxybutyrate-*co*-valerate (PHB/VA) (5–22% VA content). All polylactides underwent extensive degradation, in the range of 50–88%, and an increase in molecular weight distribution (MWD) following injection moulding at temperatures ranging from 130 to 215°C. In contrast to the polylactides, the decrease in molecular weight of the PHB and PHB/VA polymers after injection moulding at temperatures from 135 to 160°C was less drastic, in the range of 4–53%. This was accompanied by a decrease of the MWD. No evidence for low molecular weight non-volatile degradation products was observed. Injection moulding led to a decrease in the melting temperature and the heat of melting of PLA. Conversely, the moulding process did not significantly affect the melting temperature and heat of melting of polyhydroxybutyrate/valerates.

Table 2. Barrier properties (water and oxygen) of PHA and other polymers

Permeant	PHA	LDPE	HDPE	PET	Nylon
Water	5–19	1.2	0.5	1.3	25
Oxygen	23–29	250–840	30–250	5	3

WVTR in g-mil (100 cm^2-day) at 38°C, 90% RH
O_2 in cc-mil (100 cm^2-day) at 25°C 0% RH

Although the incorporation of nanoclay could be interesting in order to improve the properties of PHB and blends, their effect on the processing, degradation and, as such, final molecular weight has to be taken into account.

As reported in [69], the thermal- and thermo-mechanical degradation of the PHB and PHBV, in the presence of ammonium surfactants, commonly used as clay organo-modifiers. TGA degradation data of PHBV demonstrated that all surfactants have an effect on the polymer degradation and that this effect was more pronounced when the initial molecular weight of the polymer was low; indicating that the degradation mechanisms of both PHBV and the surfactant in the blend are interdependent and that the influence depends on the specific surfactant. The same conclusions were found by analysing the thermo-mechanical behaviour and, in all cases, the effect of surfactants is higher for neat PHBV. By studying the molecular weight after processing, they analysed on the one hand the degradation effect of each surfactant with S-Bz appearing as the most degrading surfactant. On the other hand, as the molecular weight decreased, the torque values were reduced. Interesting results regarding thermo-mechanical behaviour of some systems (PHBV + S-EtOH and PHBV4 +S-EtOH) were found because the torque, and thus the shear rate, was stable during the first 10 minutes of processing while the decrease in the molecular weight was limited. Therefore, this surfactant seems the most appropriate to prepare PHBV-based nanocomposites with organomodified clays exhibiting an adequate compromise between high shear rate, required to exfoliate layered silicates, and limited polymer degradation that could affect the material properties.

5. Comparison of the biodegradation of PHA with other biopolymers

PHAs are degraded upon exposure to soil, compost, or marine sediment. PHB can be biodegraded in both aerobic and anaerobic environments, without forming any toxic products [70]. Biodegradation is dependent on a number of factors such as microbial activity, moisture, temperature, pH of the environment, and the exposed surface area, molecular weight polymer composition, nature of monomer unit and crystallinity ([71, 72]). PHB, polypropiolactone (PPL) and PCL degraders are widely distributed in different environments ([73–75]). Majority of the strains that are able to degrade PHB belong to different taxa such as Gram-positive and Gram-negative bacteria, Streptomyces and fungi [74]. It has been reported that 39 bacterial strains of the classes Firmicutes and Proteobacteria can degrade PHB, PCL, and PBS, but not PLA [75]. The population of aliphatic polymer-degrading microorganisms in different ecosystems was found to be in the following order: PHB = PCL > PBS > PLA [70].

Copolymers containing PHB monomer units have been found to be degraded more rapidly than either PHB or 3HB-*co*-3HV copolymers.

Chowdhury reported for the first time the PHB-degrading microorganisms from Bacillus, Pseudomonas and Streptomyces species [76] From then on, several aerobic and anaerobic PHB-degrading microorganisms have been isolated from soil (Pseudomonas lemoigne, Comamonas sp. Acidovorax faecalis, Aspergillus fumigates and Variovorax paradoxus), activated and anerobic sludge (Alcaligenes faecalis, Pseudomonas, Illyobacter delafieldi), seawater and lakewater (Comamonas testosterone, Pseudomonas stutzeri) [77]. Microorganisms secrete enzymes that break down the polymer into its molecular building blocks, called hydroxyacids, which are utilized as a carbon source for growth. The principal enzyme for the degradation of PHB and oligomers derived from the polymer is PHB depolymerise. Studies on the extracellular PHB depolymerase of Alcaligenes faecalis have indicated it to be an endo-type hydrolase. Other prominent organisms in which PHB depolymerase has been identified and worked upon are Rhodospirillum rubrum, B. megaterium, A. beijerinckii, and Pseudomonas lemoignei [78].

The percentage of PHB-degrading microorganisms in the environment was estimated to be 0.5–9.6% of the total colonies [75]. Majority of the PHB-degrading microorganisms were isolated at ambient or mesophilic temperatures and very few of them were capable of degrading PHB at higher temperature. Composting at high temperature is one of the most promising technologies for recycling biodegradable plastics and thermophilic microorganisms that could degrade polymers play an important role in the composting process [79]. Thus, microorganisms which are capable of degrading various kinds of polyesters at high temperatures are of interest. A thermophilic Streptomyces sp. Isolated from soil can degrade not only PHB but also PES, PBS and poly[oligo (tetramethylene succinate)-*co*-(tetramethylene carbonate)] (PBS/C). This actinomycete has higher PHB-degrading activity than thermotolerant and thermophilic Streptomyces strains from culture collections [80]. A thermotolerant Aspergillus sp. was able to degrade 90% of PHB film after five days cultivation at 50°C [81] Furthermore, several thermophilic polyester degrading actinomycetes were isolated from different ecosystems. Out of 341 strains, 31 isolates were PHB, PCL and PES degraders and these isolates were identified as members of the genus Actinomadura, Microbispora, Streptomyces, Thermoactinomyces and Saccharomonospora [82].

The miscibility, morphology and biodegradability of PHB blends with PCL, polybutylene adipate (PBA), and poly(vinyl acetate) (PVAc) were investigated. PHB/PCL and PHB/PBA blends were immiscible in the amorphous state while PHB/PVAc are miscible. Enzymatic degradation of these blends was carried out using PHB depolymerase from Alcaligenes feacalis T1. Results showed that the weight loss of the blends decreased linearly with increase in the amount of PBA, PVAc or PCL [64].

In blends of PHB/PLA the spherulites of the blends decreased with an increase in the content of the PLA and the rate of enzymatic surface erosion also decreased with increasing PLA content in the blend. It was evident that polymer blends containing PHB usually showed improved properties and biodegradability when compared with pure PHB [83].

Biodegradation of PHA under aerobic conditions results in carbon dioxide and water, whereas in anaerobic conditions the degradation products are carbon dioxide and methane. PHA are compostable over a wide range of temperatures, even at a maximum of around 60°C with moisture levels at 55%. Studies have shown that 85% of PHA was degraded

in seven weeks ([84, 85]). PHA has been reported to degrade in aquatic environments (Lake Lugano, Switzerland) within 254 days even at temperatures not exceeding 6°C [84].

6. Market aspects of polyhydroxyalkanoates

6.1. Industrial production of polyhydroxyalkanoates

In the industrial production of PHA, the polyester is extracted and purified from the bacteria by optimising the conditions of microbial fermentation of sugar or glucose. In the 1980s, Imperial Chemical Industries developed poly (3-hydroxybutyrate-*co*-3-hydroxyvalerate) obtained via fermentation that was named 'Biopol'. It was sold under the name 'Biopol' and distributed in the U.S. by Monsanto and later Metabolix.

As a raw material for the fermentation, carbohydrates such as glucose and sucrose can be used, but also vegetable oil or glycerine from biodiesel production. Researchers in industry are working on methods with which transgenic crops will be developed that express PHA synthesis routes from bacteria to produce PHA as energy storage in their tissues [21]. Different research efforts also deal with the valorisation of wastes as non-food competing sources for cultivating a range of bacteria with the purpose of obtaining PHA biopolymers with improved sustainability. For example ongoing research deals with the growth of cyanobacteria in olive mill wastewaters to produce PHAs including their possible genetic modification to increase the yield in PHA [2]. Another group of researchers at Micromidas is working to develop methods of producing PHA from municipal wastewater. Figure 8 shows the biodegradation of PHB on the marine environment compared with other polymers.

6.2. Commercial products

Commercial ventures scaling up PHA production using fermentation processes include Telles, USA; Biomer Biotechnology Co., Germany; PHB Industrial, Brazil; Mitsubishi Gas Chemical, Japan; Kaneka, Japan; Biomatera, Italy; Jiangsu Nantian Group, China; Tianan Biologic Material, China; and Lianyi Biotech, China.

Table 3 summarises the most known commercially available polyhydroxyalkanoates.

The thermal and mechanical properties of materials described in the previous table, obtained from their respective technical datasheets, are summarised in Table 4.

Table 3. Commercial polyhydroxyalkanoates: names, producer, origin and products

Commercial name	Producer	Country	Product
Biomer	Biomer	Germany	Biomer P209 Biomer P226 Biomer P240
Minerv-PHA	Bio-on	Italy	MINERV-PHA™
Biogreen	Mitshubishi Gas	Japan	Biogreen
Biocycle	PHB Industrial	Brazil	BIOCYCLE 1000 BIOCYCLE 18BC-1 BIOCYCLE 189C-1 BIOCYCLE 189D-1
Ecogen	Tianan Biological Material Poly-one	China	ENMAT Y1000 ENMAT Y1000P ENMAT Y3000 ENMAT Y3000P
Mirel	Metabolix	USA	Mirel P4001 Mirel P4010 Mirel P5001 Mirel P5004 Mirel M2100 Mirel M2200 Mirel M4100
Nodax	P&G Chemicals	USA/Japan	Nodax™
Metabolix	Telles LLC	USA	Mvera™ B5011 Mvera™ B5010
Jiangsu Nantian	Jiangsu Nantian Group	China	P(3HB)
Goodfellow	Goodfellow Cambridge Ltd	UK	Polyhydroxyalkaonate – Biopolymer (PHA) Polyhydroxybutyrate/Polyhydroxyvalerate 12% – Biopolymer (PHB88/PHV12)
Tepha [86]	Tepha Inc	USA	P(4HB)

Table 4. Thermal and mechanical properties of commercial polyhydroxyalkanoates

Product	Thermal properties			Mechanical Properties		
	T_m [°C]	X_{cr} [%]	T_g [°C]	E [GPa]	σ [MPa]	ε [%]
Biomer P209	–	30–40	–	0.84–1.20	15–20	600–1200
Biomer P226	–	60–70	–	1.14–1.90	24–27	6–9
Biomer P240	–	60–70	–	≈1.85	28	≈11
BIOCYCLE 1000	170–175	–	117	2.2 (Flex)	32	4.0
BIOCYCLE 18BC-1	165–170	–	117	2.4 (Flex)	25	2.2
BIOCYCLE 189C-1	165–170	–	121	2.6 (Flex)	30	2.2
BIOCYCLE 189D-1	165–170	–	125	3.8 (Flex)	36	2.0
ENMAT Y1000	170-176	–	–	2.8–3.5	39	2
Mirel P4001	–	–	110	1.90 (Flex)	20	5
Mirel P4010	–	–	–	1.45 (Flex)	10	10
Mirel P5001	–	–	–	0.30–0.32	20	404–463
Mirel P5004	170	–	–	0.3–0.4	25–30	400–500
Mirel M2100	170	–	–	–	–	–
Mirel M2200	165–170	30–60	–	–	–	–
Mirel M4100	160–170	40–60	–	–	–	–
	164–166	27–45	–	–	–	–

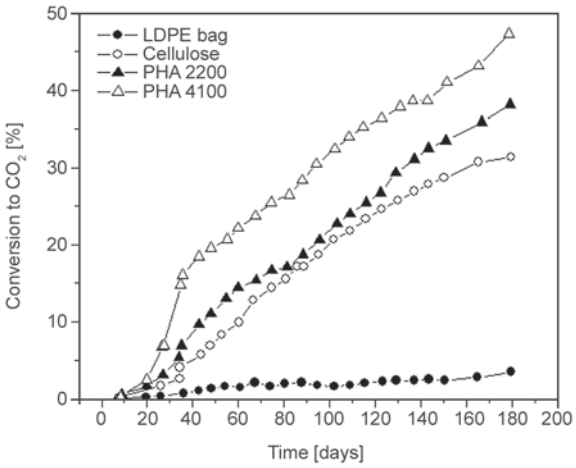

Figure 8. Biodegradation of PHB on the marine environment compared with other polymers. Faster biodegradation for PHA can be observed.

7. Conclusions

Overall, the reviewed literature highlights PHA is a very promising polymer for a wide range of applications. For example, it has better barrier properties (OTR and WVTR) and mechanical strength than other more widespread bioplastics such as PLA. In spite of its intrinsic brittleness, a lot of progress reported here has been made recently through the formulation of PHB with tailored additives and blends leading to greatly improved mechanical profiles, as well as suitable processability via extrusion or injection moulding, among others. These advances will improve its capacity to penetrate markets such as food packaging. Nevertheless, limitations still persist such as the elevated cost of commercial PHA, limited market availability and the use of refined/food competing feedstock. As such different research studies are ongoing regarding the improvement of the yield of PHA by e.g. genetic modification of the bacteria or the use of waste for their growth. Finally, further improvements could allow even more flexible grades of PHAs or transparent ones through the control of its crystallisation to be obtained (Table 5). This range of interesting properties and processability open up a bright future for PHB in applications ranging from surgical sutures, tissue engineering [87] and agricultural foils to packaging for the storage of food products [88]. Like PVC and PET, it exhibits good barrier properties [89], and can be used in the packaging industry as a biodegradable plastic for contributing to solving environmental pollution problems [90]. Due to these interesting properties, PHB is expected to be a good candidate to substitute [91] PP and PE, but also PET in certain applications.

In medicine, PHB is compatible with the blood and tissues of mammals. The monomer of PHB is a normal metabolic in the human blood. As the body reabsorbs PHB it could be used as a surgical implant, in surgery, as seam threads for the healing of wounds and blood vessels. In pharmacology, PHB can be used as microcapsules in therapy or as materials for cell and tablet packaging. It can also be used for packaging applications for deep drawing articles in the food industry, for example, bottles, laminated foils, fishnets, flowerpots, sanitary goods, fast foods, disposable cups, agricultural foils and fibres in textiles.

Table 5. Challenge and Prospects of PHAs

PHAS challenges	PHAs prospects
High cost of production and extraction	– Reduction in cost related to the use of substrate for bacteria growth coming from by products or waste materials. – Increase PHAs production by use of mixed culture or modified bacteria or microalgae. – Optimisation of PHA extraction processes.
Quality of PHA	– Optimisation of the quality and uniformity of PHAs produced in mixed culture.
Mechanical properties	– Better understanding of PHAs kinetics of crystallization and proper choice of additives (nucleating agents, plasticizers) to achieve stability in mechanical properties, and improvement in elongation at break.
Production of blends and composites	– Optimisation in the use of PHAs in blends with other biodegradable polymers achieving a reduction in cost of the final product while still maintaining the outstanding properties of PHAs in terms of barrier properties, Modulus, high biodegrability in different environments.
Blends with natural additives	– PHAs in processing are very sensitve to water presence, but proper drying of natural additives and proper choice of compatibilizers is promising for the preparation of blends of PHAs and natural polymers (starch, proteins, etc.) which can achieve the production of plastic items with high biodegradability, for example also in marine environment.

Nevertheless, further improvements are still needed to allow a broader market introduction of PHAs. One of the main limitations in the application of PHB for the production of single use items is based on its relatively high cost (7–10 Euro/kg) when compared to other polymers. Further investigations and efforts must be undertaken by scientists in order to reduce the production costs of these PHAs and increase the industrial sustainability and commercialisation of PHAs [92]. The use of natural fillers with high availability and low cost allows the production of bio-composite more suited for their application in, for example, packaging and agriculture. In addition, the use of waste feedstock for the culture of the microorganisms accumulating PHAs is also prompted as a route to lead to their greater economic viability and sustainability.

Acknowledgements

Authors acknowledge the financial support from the European Community's Seventh Framework Programme (FP7/2007-2013) under NMP grant agreement No. 280604.

References

[1] Bugnicourt E., Schmid M., Nerney O. M., Wildner J., Smykala L., Lazzeri A., Cinelli P.: Processing and validation of whey-protein-coated films and laminates at semi-industrial scale as novel recyclable food packaging materials with excellent barrier properties. Advances in Materials Science and Engineering, **2013**, 496207/1–496207/10 (2013). DOI: 10.1155/2013/496207

[2] Cinelli P., Lazzeri A., Anguillesi I., Bugnicourt E.: OliPHA a novel and efficient method for the production of polyhydroxyalkanoate polymer-based packaging from olive oil waste water. in 'Proceedings of 3rd International Conference on industrial and hazardous waste management. Chania, Crete, Greece' p8 (2012).

[3] Lepoittevin B., Devalckenaere M., Pantoustier N., Alexandre M., Kubies D., Calberg C., Jérôme R., Dubois P.: Poly(ε-caprolactone)/clay nanocomposites prepared by melt intercalation: Mechanical, thermal and rheological properties. Polymer, **43**, 4017–4023 (2002). DOI: 10.1016/S0032-3861(02)00229-X

[4] Biron M.: The plastics industry: Economic overview. in 'Thermoplastics and thermoplastic composites' (ed.: Biron M.) William Andrew Publishing, Norwich, 31–153 (2013).

[5] Dikgang J., Leiman A., Visser M.: Analysis of the plastic-bag levy in South Africa. Resources, Conservation and Recycling, **66**, 59–65 (2012). DOI: 10.1016/j.resconrec.2012.06.009

[6] Meneses J., Corrales C. M., Valencia M.: Synthesis and characterization of biodegradable polymers from cassava starch (in Spanish). Revista EIA, **8**, 57–67 (2007).

[7] Mutha N. H., Patel M. K., Premnath V.: Plastics materials flow analysis for India. Resources, Conservation and Recycling, **47**, 222–244 (2006). DOI: 10.1016/j.resconrec.2005.09.003

[8] Mulder K. F.: Sustainable consumption and production of plastics? Technological Forecasting and Social Change, **58**, 105–124 (1998). DOI: 10.1016/S0040-1625(97)00129-7

[9] Varsha Y. M., Savitha R.: Overview on polyhydroxyalkanoates: A promising biopol. Journal of Microbial and Biochemical Technology, **3**, 99–105 (2011). DOI: 10.4172/1948-5948.1000059

[10] Dawes E. A., Senior P. J.: The role and regulation of energy reserve polymers in micro-organisms. Advances in Microbial Physiology, **10**, 135–266 (1973).

[11] Laycock B., Halley P., Pratt S., Werker A., Lant P.: The chemomechanical properties of microbial polyhydroxyalkanoates. Progress in Polymer Science, **38**, 536–583 (2013).
DOI: 10.1016/j.progpolymsci.2012.06.003

[12] Noda I., Marchessault R. H., Terada M.: Polymer data handbook. Oxford University Press, London (1999).

[13] El-Hadi A., Schnabel R., Straube E., Müller G., Henning S.: Correlation between degree of crystallinity, morphology, glass temperature, mechanical properties and biodegradation of poly (3-hydroxyalkanoate) phas and their blends. Polymer Testing, **21**, 665–674 (2002).
DOI: 10.1016/S0142-9418(01)00142-8

[14] de Köning G. J. M., Lemstra P. J.: Crystallization phenomena in bacterial poly[(*R*)-3-hydroxybutyrate]: 2. Embrittlement and rejuvenation. Polymer, **34**, 4089–4094 (1993).
DOI: 10.1016/0032-3861(93)90671-V

[15] Holmes P. A.: Applications of PHB – a microbially produced biodegradable thermoplastic. Physics in Technology, **16**, 32–41 (1985).
DOI: 10.1088/0305-4624/16/1/305

[16] Di Lorenzo M. L., Raimo M., Cascone E., Martuscelli E.: Poly(3-hydroxybutyrate)-based copolymers and blends: Influence of a second component on crystallization and thermal behavior. Journal of Macromolecular Science Part B: Physics, **40**, 639–667 (2001).
DOI: 10.1081/mb-100107554

[17] Androsch R.: Surface structure of folded-chain crystals of poly(*R*-3-hydroxybutyrate) of different chain length. Polymer, **49**, 4673–4679 (2008).
DOI: 10.1016/j.polymer.2008.08.026

[18] Wunderlich B.: Reversible crystallization and the rigid–amorphous phase in semicrystalline macromolecules. Progress in Polymer Science, **28**, 383–450 (2003).
DOI: 10.1016/S0079-6700(02)00085-0

[19] Di Lorenzo M. L., Gazzano M., Righetti M. C.: The role of the rigid amorphous fraction on cold crystallization of poly(3-hydroxybutyrate). Macromolecules, **45**, 5684–5691 (2012).
DOI: 10.1021/ma3010907

[20] Schick C., Wurm A., Mohamed A.: Dynamics of reversible melting revealed from frequency dependent heat capacity. Thermochimica Acta, **392–393**, 303–313 (2002).
DOI: 10.1016/S0040-6031(02)00116-8

[21] Doi Y., Mukai K., Kasuya K., Yamada K.: Biodegradation of biosynthetic and chemosynthetic polyhydroxyalkanoates. Studies in Polymer Science, **12**, 39–51 (1994).

[22] Grassie N., Murray E. J., Holmes P. A.: The thermal degradation of poly(-(D)-β-hydroxybutyric acid): Part 1 – Identification and quantitative analysis of products. Polymer Degradation and Stability, **6**, 47–61 (1984).
DOI: 10.1016/0141-3910(84)90016-8

[23] Grassie N., Murray E. J., Holmes P. A.: The thermal degradation of poly(-(D)-β-hydroxybutyric acid): Part 2 – Changes in molecular weight. Polymer Degradation and Stability, **6**, 95–103 (1984).
DOI: 10.1016/0141-3910(84)90075-2

[24] Mohanty A. K., Misra M., Drzal L. T.: Sustainable biocomposites from renewable resources: Opportunities and challenges in the green materials world. Journal of Polymers and the Environment, **10**, 19–26 (2002).
DOI: 10.1023/a:1021013921916

[25] Erceg M., Kovačić T., Klarić I.: Thermal degradation of poly(3-hydroxybutyrate) plasticized with acetyl tributyl citrate. Polymer Degradation and Stability, **90**, 313–318 (2005).
DOI: 10.1016/j.polymdegradstab.2005.04.048

[26] Di Lorenzo M. L., Sajkiewicz P., La Pietra P., Gradys A.: Irregularly shaped DSC exotherms in the analysis of polymer crystallization. Polymer Bulletin, **57**, 713–721 (2006).
DOI: 10.1007/s00289-006-0621-4

[27] Donth E. J.: Relaxation and thermodynamics in polymers. Akademie Verlag, Berlin (1992).

[28] Scandola M., Ceccorulli G., Doi Y.: Viscoelastic relaxations and thermal properties of bacterial poly(3-hydroxybutyrate-*co*-3-hydroxyvalerate) and poly(3-hydroxybutyrate-*co*-4-hydroxybutyrate). International Journal of Biological Macromolecules, **12**, 112–117 (1990).
DOI: 10.1016/0141-8130(90)90062-F

[29] Mitomo H., Barham P. J., Keller A.: Temperature dependance of mechanical properties of poly(β-hydroxybutyrate-β-hydroxyvalerate). Polymer Communications, **29**, 112–115 (1988).

[30] Zhang L., Deng X., Zhao S., Huang Z.: Biodegradable polymer blends of poly(3-hydroxybutyrate) and hydroxyethyl cellulose acetate. Polymer, **38**, 6001–6007 (1997).
DOI: 10.1016/S0032-3861(97)00158-4

[31] Ahmed T., Marçal H., Lawless M., Wanandy N. S., Chiu A., Foster L. J. R.: Polyhydroxybutyrate and its copolymer with polyhydroxyvalerate as biomaterials: Influence on progression of stem cell cycle. Biomacromolecules, **11**, 2707–2715 (2010).
DOI: 10.1021/bm1007579

[32] Qiu Y-Z., Han J., Guo J-J., Chen G-Q.: Production of poly(3-hydroxybutyrate-*co*-3-hydroxyhexanoate) from gluconate and glucose by recombinant *Aeromonas hydrophila* and *Pseudomonas putida*. Biotechnology Letters, **27**, 1381–1386 (2005).
DOI: 10.1007/s10529-005-3685-6

[33] Caballero K. P., Karel S. F., Register R. A.: Biosynthesis and characterization of hydroxybutyrate-hydroxycaproate copolymers. International Journal of Biological Macromolecules, **17**, 86–92 (1995).
DOI: 10.1016/0141-8130(95)93522-Y

[34] Zhao K., Deng Y., Chen J. C., Chen G-Q.: Polyhydroxyalkanoate (PHA) scaffolds with good mechanical properties and biocompatibility. Biomaterials, **24**, 1041–1045 (2003).
DOI: 10.1016/S0142-9612(02)00426-X

[35] Avella M., Martuscelli E., Raimo M.: Review: Properties of blends and composites based on poly(3-hydroxy) butyrate (PHB) and poly(3-hydroxybutyrate-hydroxyvalerate) (PHBV) copolymers. Journal of Materials Science, **35**, 523–545 (2000).
DOI: 10.1023/A:1004740522751

[36] Scaffaro R., Dintcheva N. T., Marino R., La Mantia F. P.: Processing and properties of biopolymer/polyhydroxyalkanoates blends. Journal of Polymers and the Environment, **20**, 267–272 (2012).
DOI: 10.1007/s10924-011-0385-2

[37] Innocentini-Mei L. H., Bartoli J. R., Baltieri R. C.: Mechanical and thermal properties of poly(3-hydroxybutyrate) blends with starch and starch derivatives. Macromolecular Symposia, **197**, 77–88 (2003).
DOI: 10.1002/masy.200350708

[38] Shen L., Haufe J., Patel M.: Product overview and market projection of emerging bio-based plastics. PRO-BIP 2009, Final report, Utrecht (2009).

[39] Hong S-G., Hsu H-W., Ye M-T.: Thermal properties and applications of low molecular weight polyhydroxybutyrate. Journal of Thermal Analysis and Calorimetry, **111**, 1243–1250 (2013).
DOI: 10.1007/s10973-012-2503-3

[40] Parra D. F., Fusaro J., Gaboardi F., Rosa D. S.: Influence of poly (ethylene glycol) on the thermal, mechanical, morphological, physical–chemical and biodegradation properties of poly (3-hydroxybutyrate). Polymer Degradation and Stability, **91**, 1954–1959 (2006).
DOI: 10.1016/j.polymdegradstab.2006.02.008

[41] Rodrigues J. A. F. R., Parra D. F., Lugão A. B.: Crystallization on films of PHB/PEG blends. Journal of Thermal Analysis and Calorimetry, **79**, 379–381 (2005).
DOI: 10.1007/s10973-005-0069-z

[42] Wang L., Zhu W., Wang X., Chen X., Chen G-Q., Xu K.: Processability modifications of poly(3-hydroxybutyrate) by plasticizing, blending, and stabilizing. Journal of Applied Polymer Science, **107**, 166–173 (2008).
DOI: 10.1002/app.27004

[43] de O. Patrício P. S., Pereira F. V., dos Santos M. C., de Souza P. P., Roa J. P. B., Orefice R. L.: Increasing the elongation at break of polyhydroxybutyrate biopolymer: Effect of cellulose nanowhiskers on mechanical and thermal properties. Journal of Applied Polymer Science, **127**, 3613–3621 (2013).
DOI: 10.1002/app.37811

[44] Modi S. J.: Assessing the feasibility of poly-(3-hydroxybutyrate-*co*-3-hydroxyvalerate) (PHBV) and poly-(lactic acid) for potential food packaging applications. PhD Thesis, Ohio State University, Colombus (2010).

[45] Zhu C., Nomura C. T., Perrotta J. A., Stipanovic A. J., Nakas J. P.: The effect of nucleating agents on physical properties of poly-3-hydroxybutyrate (PHB) and poly-3-hydroxybutyrate-*co*-3-hydroxyvalerate (PHB-*co*-HV) produced by *Burkholderia cepacia* ATCC 17759. Polymer Testing, **31**, 579–585 (2012).
DOI: 10.1016/j.polymertesting.2012.03.004

[46] Corrêa M. C. S., Branciforti M. C., Pollet E., Agnelli J. A. M., Nascente P. A. P., Avérous L.: Elaboration and characterization of nano-biocomposites based on plasticized poly(hydroxybutyrate-*co*-hydroxyvalerate) with organo-modified montmorillonite. Journal of Polymers and the Environment, **20**, 283–290 (2012).
DOI: 10.1007/s10924-011-0379-0

[47] Whitehouse R. S.: Toughened polyhydroxyalkanoate compositions. WO 2011031558 A3, World Patent (2011).

[48] Harasawa I., Hariki Y., Maeda K., Nakamura K.: Method for cultivating algae and a covering material used therefor. U.S. Patent 4235043 A, USA (1980).

[49] Yu L., Dean K., Li L.: Polymer blends and composites from renewable resources. Progress in Polymer Science, **31**, 576–602 (2006).
DOI: 10.1016/j.progpolymsci.2006.03.002

[50] Scandola M., Ceccorulli G., Pizzoli M.: Miscibility of bacterial poly(3-hydroxybutyrate) with cellulose esters. Macromolecules, **25**, 6441–6446 (1992).
DOI: 10.1021/ma00050a009

[51] Scandola M., Focarete M. L., Adamus G., Sikorska W., Baranowska I., Świerczek S., Gnatowski M., Kowalczuk M., Jedliński Z.: Polymer blends of natural poly(3-hydroxybutyrate-*co*-3-hydroxyvalerate) and a synthetic atactic poly(3-hydroxybutyrate). Characterization and biodegradation studies. Macromolecules, **30**, 2568–2574 (1997).
DOI: 10.1021/ma961431y

[52] Choi H. J., Kim J., Jhon M. S.: Viscoelastic characterization of biodegradable poly(3-hydroxybutyrate-*co*-3-hydroxyvalerate). Polymer, **40**, 4135–4138 (1999).
DOI: 10.1016/S0032-3861(98)00627-2

[53] Avella M., Martuscelli E., Raimo M.: The fractionated crystallization phenomenon in poly(3-hydroxybutyrate)/poly(ethylene oxide) blends. Polymer, **34**, 3234–3240 (1993).
DOI: 10.1016/0032-3861(93)90396-R

[54] Gassner F., Owen A. J.: Physical properties of poly(β-hydroxybutyrate)-poly(ε-caprolactone) blends. Polymer, **35**, 2233–2236 (1994).
DOI: 10.1016/0032-3861(94)90258-5

[55] Abe H., Doi Y., Kumagai Y.: Synthesis and characterization of poly[(*R,S*)-3-hydroxybutyrate-*b*-6-hydroxyhexanoate] as a compatibilizer for a biodegradable blend of poly[(*R*)-3-hydroxybutyrate] and poly(6-hydroxyhexanoate). Macromolecules, **27**, 6012–6017 (1994).
DOI: 10.1021/ma00099a012

[56] Choi H. J., Kim J. H., Kim J., Park S. H.: Mechanical spectroscopy study on biodegradable synthetic and biosynthetic aliphatic polyesters. Macromolecular Symposia, **119**, 149–155 (1997).
DOI: 10.1002/masy.19971190115

[57] Paglia E. D., Beltrame P. L., Canetti M., Seves A., Marcandalli B., Martuscelli E.: Crystallization and thermal behaviour of poly (D(−) 3-hydroxybutyrate)/poly(epichlorohydrin) blends. Polymer, **34**, 996–1001 (1993).
DOI: 10.1016/0032-3861(93)90220-5

[58] Sharma R., Ray A. R.: Polyhydroxybutyrate, its copolymers and blends. Journal of Macromolecular Science Part C: Polymer Reviews, **35**, 327–359 (1995).
DOI: 10.1080/15321799508009640

[59] Duarte M. A. T., Hugen R. G., Sant'Anna Martins E., Pezzin A. P. T., Pezzin S. H.: Thermal and mechanical behavior of injection molded poly(3-hydroxybutyrate)/poly(ε-caprolactone) blends. Materials Research, **9**, 25–28 (2006).
DOI: 10.1590/S1516-14392006000100006

[60] Ceccorulli G., Pizzoli M., Scandola M.: Effect of a low-molecular-weight plasticizer on the thermal and viscoelastic properties of miscible blends of bacterial poly(3-hydroxybutyrate) with cellulose acetate butyrate. Macromolecules, **26**, 6722–6726 (1993).
DOI: 10.1021/ma00077a005

[61] Pizzoli M., Scandola M., Ceccorulli G.: Crystallization kinetics and morphology of poly(3-hydroxybutyrate)/cellulose ester blends. Macromolecules, **27**, 4755–4761 (1994).
DOI: 10.1021/ma00095a016

[62] Park J. W., Doi Y., Iwata T.: Unique crystalline orientation of poly[(*R*)-3-hydroxybutyrate]/cellulose propionate blends under uniaxial drawing. Macromolecules, **38**, 2345–2354 (2005).
DOI: 10.1021/ma0481611

[63] Gazzano M., Mazzocchetti L., Pizzoli M., Scandola M.: Crystal orientation switching in spherulites grown from miscible blends of poly(3-hydroxybutyrate) with cellulose tributyrate. Journal of Polymer Science Part B: Polymer Physics, **50**, 1463–1473 (2012).
DOI: 10.1002/polb.23147

[64] Kumagai Y., Doi Y.: Enzymatic degradation of binary blends of microbial poly(3-hydroxybutyrate) with enzymatically active polymers. Polymer Degradation and Stability, **37**, 253–256 (1992).
DOI: 10.1016/0141-3910(92)90167-4

[65] Singh S., Mohanty A. K.: Wood fiber reinforced bacterial bioplastic composites: Fabrication and performance evaluation. Composites Science and Technology, **67**, 1753–1763 (2007).
DOI: 10.1016/j.compscitech.2006.11.009

[66] Avérous L., Le Digabel F.: Properties of biocomposites based on lignocellulosic fillers. Carbohydrate Polymers, **66**, 480–493 (2006).
DOI: 10.1016/j.carbpol.2006.04.004

[67] Modi S., Koelling K., Vodovotz Y.: Assessment of PHB with varying hydroxyvalerate content for potential packaging applications. European Polymer Journal, **47**, 179–186 (2011).
DOI: 10.1016/j.eurpolymj.2010.11.010

[68] Gogolewski S., Jovanovic M., Perren S. M., Dillon J. G., Hughes M. K.: The effect of melt-processing on the degradation of selected polyhydroxyacids: Polylactides, polyhydroxybutyrate, and polyhydroxybutyrate-*co*-valerates. Polymer Degradation and Stability, **40**, 313–322 (1993).
DOI: 10.1016/0141-3910(93)90137-8

[69] Bordes P. H., Pollet E., Avérous L.: Effect of clay organomodifiers on degradation of polyhydroxyalkanoates. Polymer Degradation and Stability, **94**, 789–796 (2009).
DOI: 10.1016/j.polymdegradstab.2009.01.027

[70] Tokiwa Y., Calabia B. P., Ugwu C. U., Aiba S.: Biodegradability of plastics. International Journal of Molecular Sciences, **10**, 3722– 3742 (2009).
DOI: 10.3390/ijms10093722

[71] Boopathy R.: Factors limiting bioremediation technologies. Bioresource Technology, **74**, 63–67 (2000).
DOI: 10.1016/S0960-8524(99)00144-3

[72] Lee S. Y.: Plastic bacteria? Progress and prospects for polyhydroxyalkanoate production in bacteria. Trends in Biotechnology, **14**, 431–438 (1996).
DOI: 10.1016/0167-7799(96)10061-5

[73] Nishida H., Tokiwa Y.: Distribution of poly(β-hydroxybutyrate) and poly(ε-caprolactone)aerobic degrading microorganisms in different environments. Journal of Environmental Polymer Degradation, **1**, 227–233 (1993).
DOI: 10.1007/bf01458031

[74] Mergaert J., Swings J.: Biodiversity of microorganisms that degrade bacterial and synthetic polyesters. Journal of Industrial Microbiology, **17**, 463–469 (1996).
DOI: 10.1007/bf01574777

[75] Suyama T., Tokiwa Y., Ouichanpagdee P., Kanagawa T., Kamagata Y.: Phylogenetic affiliation of soil bacteria that degrade aliphatic polyesters available commercially as biodegradable plastics. Applied and Environmental Microbiolology, **64**, 5008–5011 (1998).

[76] Chowdhury A. A.: Poly-β-hydroxybuttersaure abbauende bakterien und exo-enzyme. Archives of Microbiology, **47**, 167–200 (1963).

[77] Lee S. Y.: Bacterial polyhydroxyalkanoates. Biotechnology and Bioengineering, **49**, 1–14 (1996).
DOI: 10.1002/(SICI)1097-0290(19960105)49:1<1::AID-BIT1>3.0.CO;2-P

[78] Reddy C. S. K., Ghai R., Rashmi, Kalia V. C.: Polyhydroxyalkanoates: An overview. Bioresource Technology, **87**, 137–146 (2003).
DOI: 10.1016/S0960-8524(02)00212-2

[79] Tokiwa Y., Iwamoto A., Koyama M., Kataoka N., Nishida H.: Biological recycling of plastics containing ester bonds. Makromolekulare Chemie, Macromolecular Symposia, **57**, 273–279 (1992).
DOI: 10.1002/masy.19920570125

[80] Calabia B. P. T., Tokiwa Y.: Microbial degradation of poly(d-3-hydroxybutyrate) by a new thermophilic *Streptomyces* isolate. Biotechnology Letters, **26**, 15–19 (2004).
DOI: 10.1023/B:BILE.0000009453.81444.51

[81] Sanchez J., Tsuchii A., Tokiwa Y.: Degradation of polycaprolactone at 50°C by a thermotolerant *Aspergillus* sp. Biotechnology Letters, **22**, 849–853 (2000).
DOI: 10.1023/a:1005603112688

[82] Tseng M., Hoang K-C., Yang M-K., Yang S-F., Chu W.: Polyester-degrading thermophilic actinomycetes isolated from different environment in Taiwan. Biodegradation, **18**, 579–583 (2007).
DOI: 10.1007/s10532-006-9089-z

[83] Koyama N., Doi Y.: Miscibility of binary blends of poly[(*R*)-3-hydroxybutyric acid] and poly[(*S*)-lactic acid]. Polymer, **38**, 1589–1593 (1997).
DOI: 10.1016/S0032-3861(96)00685-4

[84] Johnstone B.: A throw away answer. Far Eastern Economic Review, **147**, 62–63 (1990).

[85] Brandl H., Gross R., Lenz R., Fuller R.: Plastics from bacteria and for bacteria: Poly(β-hydroxyalkanoates) as natural, biocompatible, and biodegradable polyesters. Advances in Biochemical and Engineering Biotechnology, **41**, 77–93 (1990).

[86] Rizk S., Connelly D. W., Bernasconi M., Carter A. J., Martin D. P., Williams S. F.: Injection molding of poly-4-hydroxybutyrate. U.S. Patent 20130309166, USA (2013).

[87] Misra S. K., Ohashi F., Valappil S. P., Knowles J. C., Roy I., Silva S. R. P., Salih V., Boccaccini A. R.: Characterization of carbon nanotube (MWCNT) containing P(3HB)/bioactive glass composites for tissue engineering applications. Acta Biomaterialia, **6**, 735–742 (2010).
DOI: 10.1016/j.actbio.2009.09.023

[88] Bucci D. Z., Tavares L. B. B., Sell I.: PHB packaging for the storage of food products. Polymer Testing, **24**, 564–571 (2005).
DOI: 10.1016/j.polymertesting.2005.02.008

[89] Miguel O., Fernandez-Berridi M. J., Iruin J. J.: Survey on transport properties of liquids, vapors, and gases in biodegradable poly(3-hydroxybutyrate) (PHB). Journal of Applied Polymer Science, **64**, 1849–1859 (1997).
DOI: 10.1002/(sici)1097-4628(19970531)64:9<1849::aid-app22>3.0.co;2-r

[90] Chen G-Q.: Biofunctionalization of polymers and their applications. Biofunctionalization of Polymers and their Applications, **125**, 29–45 (2011).
DOI: 10.1007/10_2010_89

[91] Kosior E., Messias R., Fowler P.: Lightweight compostable packaging: Literature review. The Waste and Resources Action Programme, Banbury (2006).

[92] Bhatt R., Patel K., Trivedi U.: Biodegradation of poly (3-hydroxyalkanoates). in 'A handbook of applied biopolymer technology: Synthesis, degradation and applications' (eds.: Sharma S. K., Mudhoo A.) The Royal Society of Chemistry Publishing, London, 311–331 (2011).
DOI: 10.1039/9781849733458-00311

eXPRESS Polymer Letters Vol.8, No.11 (2014) 809–822
Available online at www.expresspolymlett.com
DOI: 10.3144/expresspolymlett.2014.83

Preparation and characterization of EPDM/silica nanocomposites prepared through non-hydrolytic sol-gel method in the absence and presence of a coupling agent

T. H. Mokhothu[1], *A. S. Luyt*[1*], *M. Messori*[2]

[1]Department of Chemistry, University of the Free State (Qwaqwa Campus), Private Bag X13, 9866 Phuthaditjhaba, South Africa
[2]Department of Engineering 'Enzo Ferrari', University of Modena and Reggio Emilia, Via Vignolese 905/A – 41125 Modena, Italy

Received 21 March 2014; accepted in revised form 4 June 2014

Abstract. Ethylene propylene diene monomer (EPDM) rubber composites containing *in situ* generated silica particles was prepared through a non-hydrolytic sol-gel (NHSG) method with silicon tetrachloride as precursor. The silica particles were homogenously dispersed in the EPDM matrix, but there were agglomerates at high silica contents. The swelling experiments showed a decrease in the crosslinking density of the vulcanized rubber due to the presence of the silica particles for both the composites prepared in the presence and absence of a coupling agent, bis-[-3-(triethoxysilyl)-propyl]-tetrasulfide (TESPT). Unlike the composites prepared through a hydrolytic sol-gel (HSG) method with TEOS as precursor, the TESPT did not seem to take part in the sol-gel reaction. The presence of TESPT influenced the interaction and dispersion of the silica particles in the EPDM matrix, which gave rise to increased thermal stability of the EPDM when compared to the composites prepared in the absence of TESPT. However, ethylene chloride and TESPT evaporated from the samples at temperatures below the EPDM decomposition range. The values of the Nielsen model parameters, that gave rise to a good agreement with the experimentally determined Young's modulus values, indicated improved dispersion and reduced size of the silica aggregates in the EPDM matrix. There was also good agreement between the storage modulus and Young's modulus values. The filler effectiveness (Factor C) indicated a mechanical stiffening effect and a thermal stability contribution by the filler, while the damping reduction (DR) values confirmed that the EPDM interacted strongly with the well dispersed silica particles and the polymer chain mobility was restricted. The tensile properties, however, were in some cases worse than those for the samples prepared through the HSG method in the presence of TEOS.

Keywords: *polymer composites, EPDM, silica, non-hydrolytic sol-gel*

1. Introduction

The incorporation of inorganic oxides such as silica and/or titania into rubber matrices prepared by the conventional sol-gel routes led to materials with enhanced properties when compared to both unfilled rubbers and rubbers filled with traditionally prepared particles. The sol-gel process is a chemical technique initially employed to prepare high purity inorganic oxides such as glasses and ceramic materials. The advantage of the sol-gel route is that it allows fine control of particle size and distribution owing to the low temperature conditions, and it is therefore suitable for organic materials to be introduced into the process. The most widely used sol-gel route is the hydrolytic process, which involves hydrolysis and condensation of the precursors (metal oxide) to form oxide networks. The hydrolytic sol-gel process is generally divided into two steps:

*Corresponding author, e-mail: LuytAS@qwa.ufs.ac.za

the first step hydrolysis, which produces hydroxyl groups, and the second step condensation, which involves the polycondensation of hydroxyl groups and residual alkoxyl groups to form a three-dimensional network. The inorganic oxide can be directly grown in the organic matrix leading to the formation of organic-inorganic hybrid structures composed of metal oxide and organic phases intimately mixed with each other. The main drawback of the hydrolytic route is the low miscibility of the sol-gel aqueous system, which limits the dispersion of the filler in the polymer [1–3]. The inorganic oxide prepared in the hydrolytic sol-gel way also has low purity and crystallinity.

An alternative method to prepare organic-inorganic material is the non-hydrolytic sol-gel (NHSG) process, which can be used to produce metal oxides of high purity and crystallinity. Moreover, the NHSG route features different reactions and reaction conditions, which significantly affect the texture, homogeneity and surface chemistry of the resulting oxide [4–6]. In the past 20 years, several non-hydrolytic synthesis methods of oxides and mixed oxides have been described, involving the reaction of precursors (alkoxides, chlorides, acetylacetonates) with oxygen donors (ethers, alcohols, ketones) [4–10]. The main non-hydrolytic routes involve the reaction of a metal chloride with either a metal alkoxide or organic ether, acting as oxygen donors [7–9] as described in Figure 1.

On the other hand, the formation of alkyl halide and/or alkyl ethers as by-products and the potential incompatibility with oxygen containing species have to be taken into account as possible negative aspects. The possibility of preparing polymers reinforced with metal oxides generated *in situ* by a non-hydrolytic sol-gel process, has been reviewed by several authors in recent publications [2, 3]. The authors focused on poly(methyl methacrylate) (PMMA)/titanium dioxide (TiO_2) and epoxy resin/titanium dioxide (TiO_2) nanocomposites. In both investigations benzyl alcohol (BzOH) was used as an oxygen donor and titanium(IV)chloride ($TiCl_4$) as a precursor. In both cases, improvements in the mechanical and functional properties were observed, independent of the chosen polymer matrix. This was due to the improved interfacial interactions between the organic and inorganic phases brought about by the non-hydrolytic sol-gel route. Morselli *et al*. [1] investigated the non-hydrolytic sol-gel synthesis of PMMA/TiO_2 nanocomposites, starting from titanium(IV)chloride as a titania (TiO_2) precursor and benzyl alcohol as an oxygen donor. The *in situ* generated titania did not have any negative effect on the PMMA molecular weight and thermal stability, and a significant increase in both the glass transition temperature and the storage modulus was observed for all the PMMA nanocomposites.

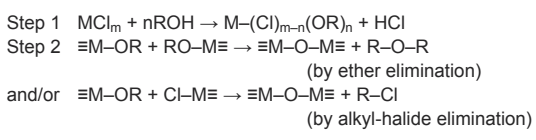

Figure 1. Non-hydrolytic sol-gel reaction scheme

However, the use of the NHSG processes to prepare filled polymers is not widely reported in literature, and most reports are limited to rigid thermoplastics [1, 2] and thermosets [3]. In the present work silica nano-particles were *in situ* generated by using an NHSG process from silicon tetrachloride ($SiCl_4$) as silica precursor and tert-butanol (*t*-BuOH) as oxygen donor in the presence of EPDM rubber dissolved in toluene. The low boiling point of *t*-BuOH allows the use of mild conditions during solvent elimination, in which polymer chain degradation and/or plasticizing effects can be avoided for the composites prepared by the sol-gel reaction. Moreover, the *t*-BuOH is not only used as an oxygen donor, but due to the alkyl group steric effect, it can also act as a capping agent, and therefore, as a particle size and phase controller. This approach is expected to reduce the filler-filler interaction and give rise to improved thermal, mechanical and thermomechanical properties, as well as a better morphology and improved crosslinking.

2. Experimental

2.1. Materials

Silicon tetrachloride (SiCl4), tert-butanol (*t*-BuOH), tin(II)2-ethylhexanoate, dicumyl peroxide, bis-[-3-(triethoxysilyl)-propyl]-tetrasulfide (TESPT) and toluene were all supplied by Sigma-Aldrich (Milan, Italy). The materials were used as received without further purification. Ethylene propylene diene monomer rubber (EPDM), Polimeri Europa Dutral® TER 4038, density 0.91 g·cm^{-3}, was provided by ATG Italy (Castel d'Argile, BO, Italy).

2.2. Preparation of EPDM/SiO_2 nanocomposites in the absence and presence of TESPT

The EPDM/SiO_2 nanocomposites were prepared by dissolving EPDM rubber in toluene (3 g/100 mL) at room temperature, and a coupling agent (TESPT) was added (4 wt% with respect to EPDM) to the EPDM solution for composites prepared in the presence of TESPT. The non-hydrolytic sol-gel (NHSG) system was prepared as follows: a given amount of $SiCl_4$ was added drop-wise to *t*-BuOH under vigorous stirring at room temperature for 15 minutes, followed by addition of tin(II)2-ethylhexanoate (1:25:0.04 mol ratio). The resulting sol was mixed with a previously prepared EPDM and EPDM-TESPT solutions in round-bottom flasks and heated in an oil bath at 70°C for 24 hours in order to complete the NHSG reaction for the conversion of $SiCl_4$ to SiO_2. The solutions were cooled to room temperature, followed by the addition of dicumyl peroxide (DCP) (4 wt% with respect to EPDM) under stirring. The reaction mixtures were taken to a rotating evaporator to eliminate about 90% of the volatile substances (toluene, unreacted *t*-BuOH and by-products of the NHSG reaction). The samples with and without TESPT (90/10 w/w EPDM/SiO_2 and 80/20 w/w EPDM/SiO_2) were obtained by casting the solutions in Petri dishes, dried overnight and later vulcanized by compression at 160°C for 20 min. The same route was used to prepare TESPT containing EPDM samples as a control for FTIR analysis. In this case no other chemical was added.

2.3. Characterization methods

The transmission electron microscopy (TEM) images were obtained using a 200 kV FEI Tecnai20 transmission electron microscope fitted with Gatan Tridiem. The EPDM silica filled samples were mounted on cryo-pins and frozen in liquid nitrogen. 100–150 nm sections were cut at –100°C using a Reichert Ultra-Cut S ultra-microtome chuck, collected on copper grids and viewed.

Fourier-transform infrared (FTIR) spectra of the pure EPDM and its silica filled nanocomposites were obtained using a Perkin Elmer Spectrum 100 FTIR spectrophotometer. The samples were analyzed over a range of 600–4000 cm^{-1} with a resolution of 4 cm^{-1} using an attenuated total reflectance (ATR) detector. All the spectra were averaged over 16 scans.

The crosslinking degree was determined through equilibrium swelling tests by immersing at least three rectangular specimens for each composition in 15 mL of toluene at room temperature for several hours, and the mean values are reported. The solvent was replaced hourly after each measurement to eliminate all uncross-linked fractions, such as unvulcanized EPDM chains, which could lead to incorrect values of the swelling ratio. The swelling experiments were done over a period of 24 hours until a constant mass was reached. Equilibrium swelling was determined until the swollen mass (m_s) reached a constant value, after which the samples were dried to constant mass (dried mass (m_d)) and the absolute swelling ratio (q) was evaluated according to Equation (1):

$$q = \frac{m_s}{m_d} \tag{1}$$

The absolute extractable fraction (f), where m_0 is the mass of the sample before immersion in toluene, was determined using Equation (2):

$$f = \frac{m_0 - m_d}{m_0} \cdot 100 \tag{2}$$

The values of q and f were both normalised to the actual EPDM weight. Their values were determined using Equations (3) and (4):

$$q_{EPDM} = \frac{q}{c_{EPDM}} \tag{3}$$

$$f_{EPDM} = \frac{f}{c_{EPDM}} \tag{4}$$

where c_{EPDM} is the mass fraction of EPDM present in the composites. The gel content was determined using Equations (5) to (7), where m_{EPDM} is the mass of EPDM without silica.

$$m_{EPDM} = m_0 \cdot c_{EPDM} \tag{5}$$

$$\% \text{ Extraction } = \frac{m_0 - m_d}{m_{EPDM}} \cdot 100 \tag{6}$$

$$\% \text{ Gel} = 100 - \% \text{ Extraction} \tag{7}$$

Thermogravimetric analysis (TGA) was performed with a Perkin Elmer STA6000 simultaneous thermal analyzer. The analysis was done under flowing nitrogen at a constant flow rate of 20 $mL \cdot min^{-1}$, and the samples (20–25 mg) were heated from 25 to 600°C at a heating rate of 10°C·min^{-1}.

The TGA-FTIR analyses were performed in a Perkin Elmer STA6000 simultaneous thermal analyser from Waltham, Massachusetts, U.S.A. The analyses were done under flowing nitrogen at a constant flow rate of 20 mL·min^{-1}. Samples (20–25 mg) were heated from 30 to 600°C at 10°C·min^{-1}. The furnace was linked to the FTIR (Perkin Elmer Spectrum 100) with a gas transfer line. The volatiles were scanned over a 400–4000 cm^{-1} wavenumber range at a resolution of 4 cm^{-1}. The FTIR spectra were recorded in the transmittance mode at 250°C during the thermal degradation process.

The tensile properties of the samples were determined using a Hounsfield H5KS tensile tester at a crosshead speed of 100 mm·min^{-1} and 20 mm gauge length at ambient temperature. The samples were rectangular shaped with a width of 12 mm and a thickness varying between 0.47 and 0.67 mm. At least five specimens were tested for each composition, and the mean values are reported. For comparison, Young's modulus was predicted according to Nielsen's theoretical model [11–17].

The dynamic mechanical analysis (DMA) of the samples was done in a Perkin Elmer Diamond DMA dynamic mechanical analyzer. Rectangular shaped samples with dimensions of 40 mm length, 10 mm width and thickness varying between 0.47 and 0.67 mm thick were tested in the tensile mode, while heated under nitrogen flow from –100 to 100°C at a heating rate of 3°C·min^{-1}, and at a frequency of 1 Hz.

3. Results and discussion

The TEM micrographs and the particle size distribution graphs (determined from an average of 40 particles per sample) of the EPDM/silica composites prepared in the absence and presence of TESPT are shown in Figures 2 and 3. The 90/10 w/w EPDM/SiO_2 composite prepared in the absence of TESPT shows homogeneously and fairly well dispersed silica particles, but with clear evidence of particle agglomeration. Much larger agglomerates are visible for the 80/20 w/w EPDM/SiO_2 sample prepared in the absence of TESPT, indicating increased particle-particle interaction (Figure 2b). The particle size distribution determined from the visible particles confirms the presence of larger particles for the composites prepared without TESPT (Figure 3a). The introduction of TESPT during synthesis reduced the particle-particle interaction, giving rise to reduced particle agglomeration and observably better dispersion (Figures 2c and 2d, and Figure 3b). Well dispersed and non-agglomerated particles are even visible in the 80/20 w/w EPDM/SiO_2 sample (Figure 2d). In our case the *in situ* synthesis using the non-hydrolytic route seems to have overcome the problems we experienced by using the hydrolytic route, in which the low miscibility of the sol-gel aqueous system gave rise to more agglomeration and reduced dispersion of the silica particles [1–4]. The larger agglomerates at higher silica contents is the result of an increase in coalescence of the growing silica particles when increasing the amount of *in situ* formed dispersed phase. The silica particles may also have agglomerated in the suspension, because the hydrophilic silica particles have a tendency to associate via hydrogen bonding [16–20]. When comparing the particle size distribution results with those obtained during our previous study on the same system, but with the samples prepared by an HSG method in the absence and presence of a coupling agent [16, 17], smaller particles were observed in the present study. This confirms that the NHSG route was able to produce smaller filler particles in the rubber matrix than the HSG route.

The FTIR spectra of all the investigated samples are shown in Figure 5. In the nanocomposites the EPDM can be identified by two strong peaks around 2920 and 2850 cm^{-1} assigned to the C–H stretching vibrations (Figure 5a). More peaks are observed at 721, 1376 and 1464 cm^{-1} and are assigned to CH_2 stretching, and CH_3 and CH_2 bending respectively [16, 17]. The SiO_2 in the nanocomposites can be identified from strong stretching vibrations of the siloxane (Si–O–Si) bond at 1085 cm^{-1}, a small asymmetric stretch peak of Si–O–C at 802 cm^{-1}, and a small peak at 938 cm^{-1} assigned to Si–O stretching, indicating the presence of some silanol (Si–OH) groups, which was confirmed by comparing the FTIR spectrum of SiO_2 in Figure 5a with those of the nanocomposites. The broad peak at 3340 cm^{-1} in the SiO_2 spectrum could be assigned to the stretching vibrations of –OH groups as a result of unreacted silanols (–Si–OH). Similar peaks are observed for the EPDM/SiO_2 composites, but without the –OH peak (Figure 5a). We observed and explained the same peaks in our previous study on the hydrolytic sol-gel (HSG) synthesis at long reaction times [16], and the peaks were the result of grafted and/or unreacted fractions of TEOS such as the ethoxysilane (–Si–OC_2H_5) and silanol groups (–Si–OH) due to unhydrolyzed silica

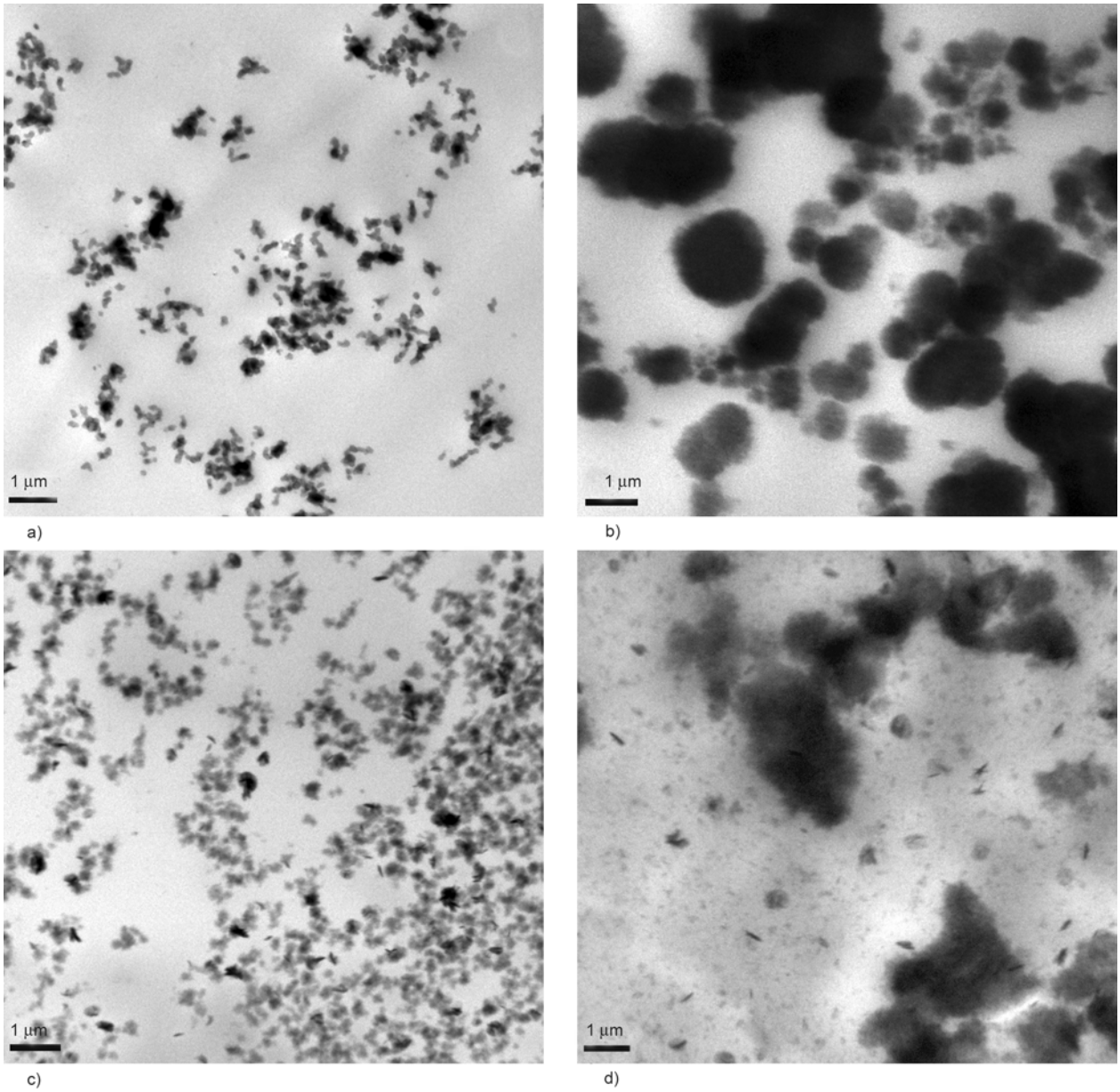

Figure 2. TEM micrographs of composites without TESPT (a) 90/10 w/w and (b) 80/20 w/w EPDM/SiO_2, and with TESPT (c) 90/10 w/w and (d) 80/20 w/w EPDM/SiO_2

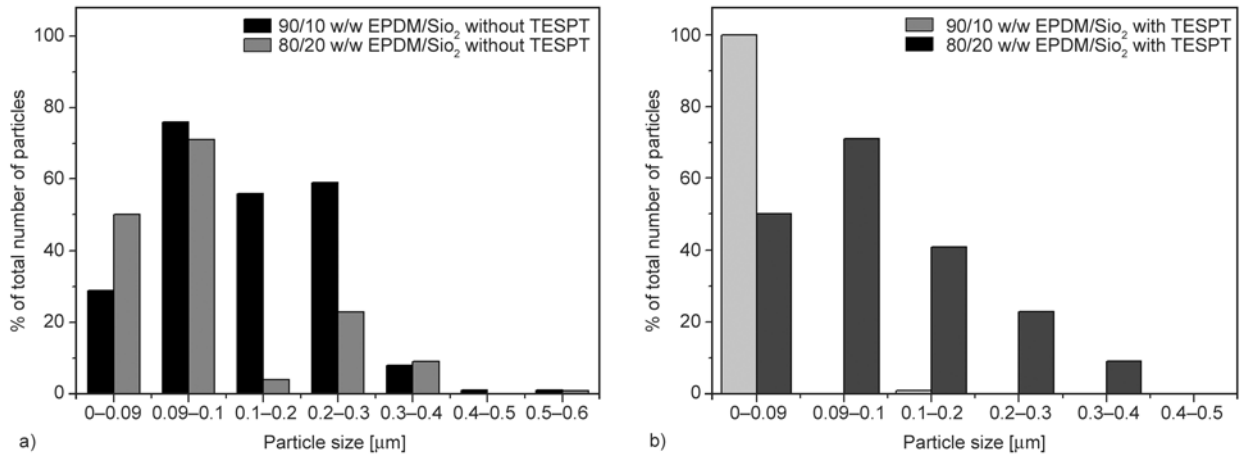

Figure 3. Particle size distribution graphs of EPDM/SiO_2 composites prepared in the (a) absence and (b) presence of TESPT

that reacted with dicumyl peroxide (DCP) during vulcanization. The NHSG process is divided into two steps. The first step involves the reaction of a metal halide or a metal alkoxide with an organic oxygen donor (such as an alcohol or ether). The second step (condensation) can follow different pathways depending on the alkoxide used. One of the most used condensation reactions occurs through alkyl halide elimination and/or ether elimination as indicated in Figure 1 [1, 5, 6, 21–23]. However, tertiary alcohols can lead to the *in situ* formation of hydroxyl groups, which react in a second step with a chloride group according to Figure 4. The alcohol route has been much less investigated for the preparation of oxides and mixed oxides than the alkoxide and ether routes [5].

In this study a tertiary alcohol (*t*-BuOH) was used and according to Figure 4, the alcohol has reacted further to form silanol groups and this could explain the presence of the small peak at 938 cm^{-1} in the nanocomposite spectra, which is the result of silanol groups that did not react further to form siloxane groups (Si–O–Si), and that may have grafted to the rubber chains by reacting with the DCP during vulcanization (Figure 5a).

The spectrum of EPDM-TESPT in Figure 5b contains a combination of the peaks observed for EPDM in Figure 5a and TESPT in Figure 5b with no new peaks or obvious peak shifts. TESPT therefore clearly did not react with EPDM under the preparation conditions used. The FTIR spectrum of the 80/20 w/w EPDM/SiO_2 prepared in the presence of TESPT shows that most of the silanols (Si–OH) reacted to form Si–O–Si bonds, with the accompanying reduction in the number of free –OH groups. This means that the silanols completely reacted to form silica links (Figure 5b). This spectrum also shows peaks around 1390, 1167 and 780 cm^{-1}, that were the characteristic peaks observed for TESPT in Figure 5b. Unlike the composites prepared through the hydrolytic sol-gel (HSG) route with TEOS as precursor [17], the TESPT did not seem to take part in the sol-gel reaction, and probably accumulated at the EPDM-silica interface.

The equilibrium swelling and gel content results for the EPDM/SiO_2 composites with and without TESPT are shown in Table 1. The equilibrium swelling test shows a decrease in the crosslink density with increasing filler content of the EPDM/ SiO_2 composites with and without TESPT. This can be observed from the absolute swelling ratio (q and q_{EPDM}) values that increase with increasing silica content, the increasing values of the extractable fraction (f and f_{EPDM}), and the decreasing gel content values. The presence of the NHSG *in situ* generated silica particles in the EPDM inhibited the crosslinking of the rubber chains during vulcanization. The reason for this observation is that increasing amounts of DCP were used for the grafting of silanol onto the rubber chains and therefore less DCP was available to initiate the crosslinking of the rubber chains. The FTIR results also confirm this explanation, especially for composites without TESPT (10 and 20 w/w EPDM/SiO_2). From the swelling and extraction results it is

Step 1 M–Cl + ROH → M–OH + R–Cl
Step 2 M–Cl + M–OH → M–O-M + H–Cl

Figure 4. *In situ* formation of hydroxyl groups during the non-hydrolytic sol-gel process

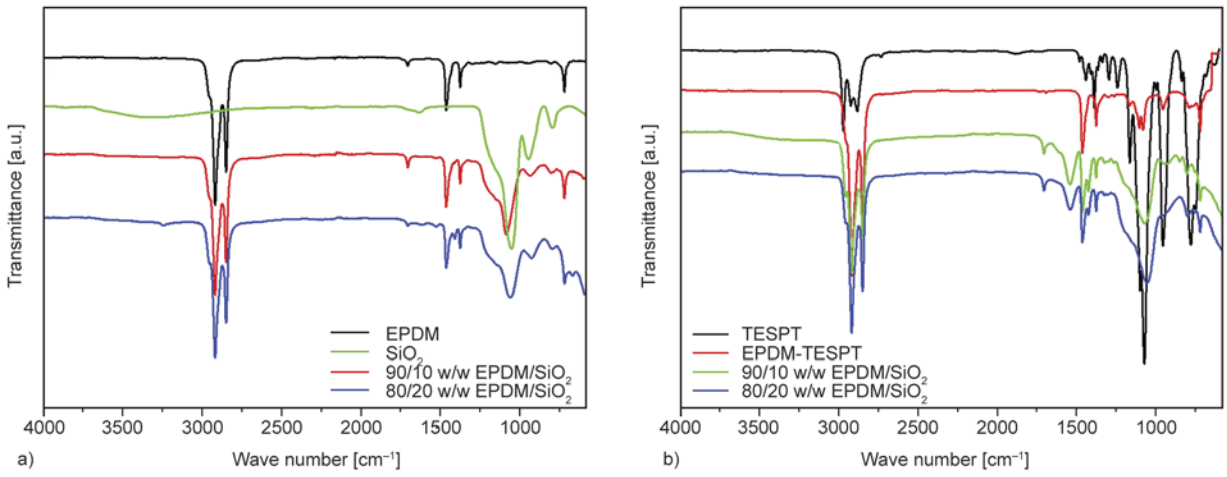

Figure 5. FTIR spectra of (a) EPDM, SiO_2 and the EPDM/SiO_2 composites, and (b) TESPT, EPDM-TESPT, and EPDM/SiO_2 with TESPT composites

Table 1. Swelling and extraction results of EPDM and the EPDM/SiO_2 composites

Samples (w/w)	Q	q_{EPDM}	f [%]	f_{EPDM} [%]	Gel [%]
EPDM	2.7±0.0	2.7±0.0	4.2±5.5	4.2±5.5	95.8±5.5
Composites without TESPT					
90/10 EPDM/SiO_2	3.1±0.1	3.4±0.1	7.9±0.5	8.7±0.5	91.2±0.5
80/20 EPDM/SiO_2	6.5±0.0	7.7±0.0	13.1±1.3	15.4±1.5	83.7±1.6
Composites with TESPT					
90/10 EPDM/SiO_2	3.2±0.0	3.5±0.1	7.8±0.8	8.6±0.9	91.3±0.9
80/20 EPDM/SiO_2	2.7±0.0	3.1±0.0	9.8±0.4	11.5±0.5	87.8±0.5

The absolute swelling ratio (q) and extractable fraction (f), and their values normalized with respect to the EPDM content (q_{EPDM}, and f_{EPDM})

clear that the *in situ* generation of silica particles through the sol-gel process led to a hindering effect on the vulcanization process, which limited the extent of crosslinking of the EPDM phase, as already observed and explained for the same material prepared through HSG synthesis with TEOS precursor at long reaction times [16].

In the case of the composites prepared in the presence of TESPT the decrease in the crosslinking density is probably not the result of DCP reacting with the silanol groups, because the FTIR analysis of these composites does not show the presence of silanol groups, indicating that most of the Si–OH reacted to form siloxane groups. Another possible explanation is that there was enough free volume between the chains to accommodate the toluene molecules during the swelling test, which led to an increase in the swelling ratios. A similar observation and explanation were given for HSG composites prepared from TEOS in the presence of TESPT at long reaction times [17].

The TGA curves of all the investigated samples are shown in Figure 6, while Table 2 shows a summary of the TGA results. The TGA curves show two mass loss steps for all the composites. This is different from the TGA results for the same composites prepared according to the HSG route [16]. These samples did not show the first mass loss step observed here. In order to figure out the reasons for this difference, we did a TGA-FTIR analysis on the samples prepared according to the HSG and NHSG routes. The FTIR spectra obtained at 250°C are presented in Figure 7. The interesting observation in Figure 7a is the peaks appearing at 2956 and 1144 cm^{-1} that indicate the CH_2 groups and the C–Cl bond in ethylene chloride which formed in Step 1 presented in Figure 4. There is also a strong peak at 1756 cm^{-1}, which indicates that acid chlorides may have formed part of the volatiles released at this temperature. It seems as if the ethylene chloride is less volatile than the ethanol formed during the HSG sol-gel reaction with TEOS as precursor [16]. The ethanol probably evaporated during the course of the sol-gel reaction, while the ethylene chloride formed during the NHSG sol-gel reaction with silicon tetrachloride remained trapped in the polymer and only evaporated at much higher temperatures during the TGA analyses of the samples. The larger mass loss observed for the TESPT containing samples prepared according to the NHSG route is clearly due to the evaporation of ethylene chloride and other acid chlorides, as discussed above, together with unreacted TESPT (the additional peaks in Figure 7b correspond well with the typical peaks of TESPT, as described earlier). We can therefore confidently state that TESPT did not

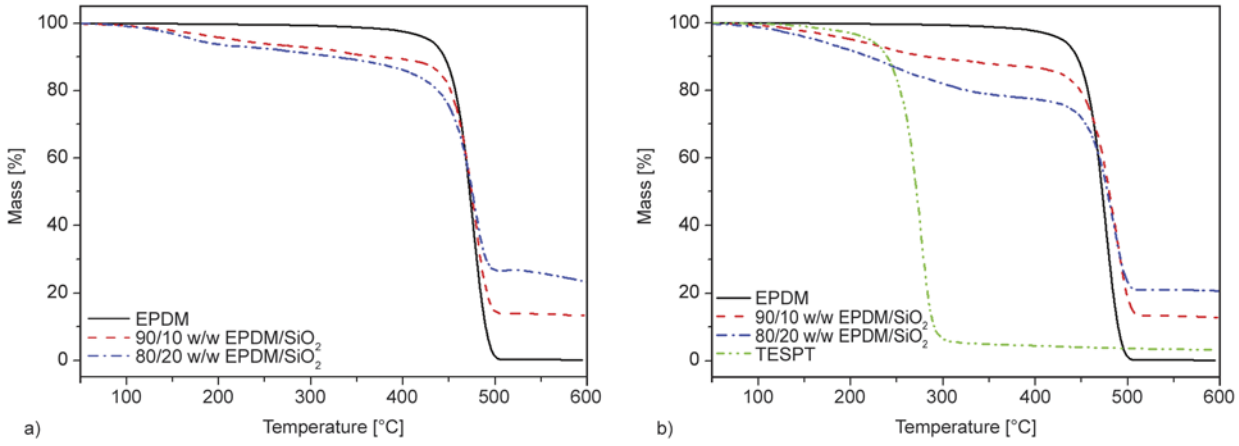

Figure 6. TGA curves for a) EPDM and silica filled EPDM composites and b) EPDM and silica filled EPDM composites in the presence of TESPT

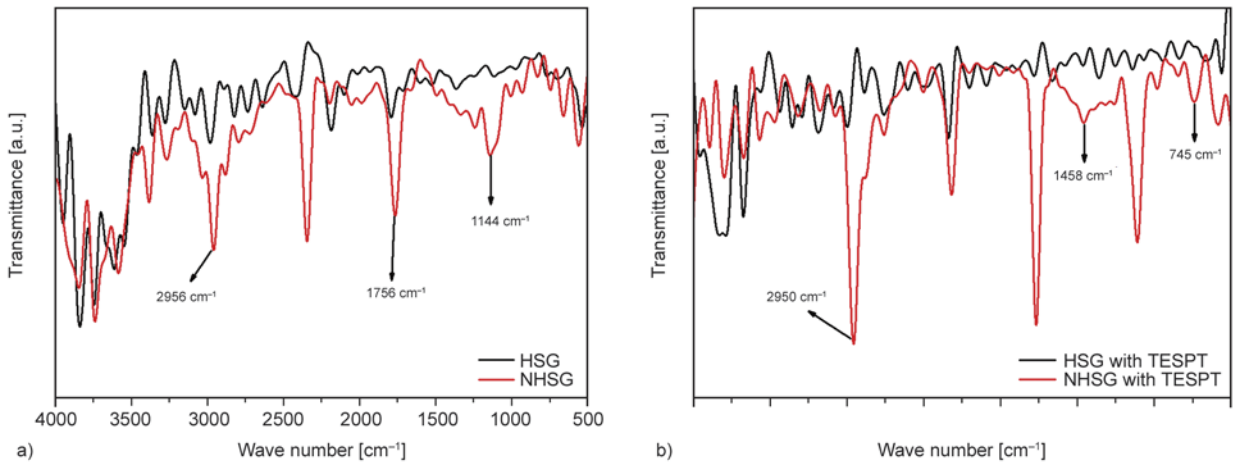

Figure 7. FTIR spectra of 80/20 w/w EPDM/SiO_2 during the thermal degradation in a TGA at a heating rate of 10°C·min^{-1} taken at 250°C for NHSG and HSG (a) without TESPT and (b) with TESPT

take part in the sol-gel reaction according to the NHSG route with $SiCl_4$ as precursor. It probably went to the interface between the polymer matrix and the silica nanoparticles, and in the process improved the interaction between EPDM and the silica nanoparticles, but not to the same extent as in the HSG process as will be shown later. At higher temperatures the TESPT then evaporated with the ethylene chloride and other acid chlorides.

The onset of thermal degradation looks very similar for all the investigated samples, and the temperatures at maximum degradation rate (T_{max}) are also very similar within experimental error. However, the actual rate of degradation is lower for the silica-containing samples (slopes of second degradation step less steep, Figure 6). The decrease in the rate of degradation is more pronounced for the composites prepared in the presence of TESPT (Figure 6b). The most probable explanation is that the well dispersed silica particles found for samples prepared in the presence of TESPT, reduced the polymer chain mobility and retarded the diffusion of volatile products from the sample.

Table 2 shows that the char content at 600°C increases with increasing silica content for the composites prepared in the absence and presence of TESPT. The values are slightly higher than what is theoretically expected, and an FTIR analysis of the char (Figure 8) shows the presence of carbon (C–O bending at 1615 cm^{-1}). This could explain the higher than expected char content. The other observed peaks are the Si–O–Si stretching and Si–O–C bending at 1055 and 802 cm^{-1} respectively. The composites prepared in the absence and presence of TESPT show char spectra with similar peaks.

The Young's modulus as function of volume fraction of neat EPDM and its silica filled composites are shown in Figure 9 together with its predicted Nielsen theoretical model fitting [11–13, 24, 25]. The values for Young's modulus, stress and elonga-

Table 2. Summary of TGA results of EPDM and EPDM/SiO_2 composites

Samples	$M_{300°C}$ [%]	T_{max} [°C]	Char content [%]	% SiO_2
EPDM	99.4±0.04	475±4.9	0	0
Unmodified composites				
90/10 w/w EPDM/SiO_2	92.4±0.5	480±1.4	12.9±0.6	12.9±0.6
80/20 w/w EPDM/SiO_2	91.2±0.3	476±2.1	22.6±0.5	22.6±0.8
TESPT modified composites				
TESPT	6.5±0.0	277±1.4	3.3±0.0	–
90/10 w/w EPDM/SiO_2	89.3±0.1	481±4.9	13.7±1.1	12.8±0.6
80/20 w/w EPDM/SiO_2	81.8±0.5	482±7.8	22.0±1.6	21.9±1.6

$M_{300°C}$, T_{max} and % SiO_2 are the mass loss at 300°C, the temperature at maximum degradation rate, and the silica content after normalization taking into account the char content of TESPT

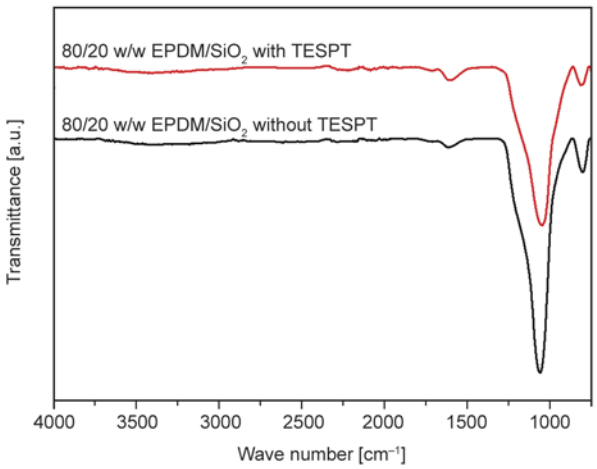

Figure 8. FTIR spectra of the char taken at 600°C of two of the investigated composites

tion at break are summarized in Table 3. For composite materials consisting of spherical particles in the matrix, the Nielsen equation has the form given in Equations (8) and (9):

$$E = E_1\left[\frac{1 + AB\varphi_2}{1 - B\psi\varphi_2}\right] \tag{8}$$

$$B = \frac{\frac{E_2}{E_1} - 1}{\frac{E_2}{E_1} + A} \tag{9}$$

where E, E_2 and E_1 are the modulus values of the composite, filler and matrix respectively, and φ_2 is the volume fraction of the filler. The theoretical modulus used for the silica particles was $E_2 = 70$ GPa [26]. The factor ψ takes into account the values of φ_m of the dispersed phase and it is given by Equation (10):

$$\psi = 1 + \left[\left(\frac{1 - \varphi_m}{\varphi_m^2}\right)\varphi_2\right] \tag{10}$$

where φ_m is the maximum packing fraction. The constant B takes into account the relative moduli of the filler and matrix phases, and its value is 1.0 for very large E_2/E_1 ratios (the values for E_2 and E_1 are 70 GPa and 2.0 MPa, respectively, and therefore we could confidently use a value of 1.0). The constant A is related to the Einstein coefficient given by Equation (11) and is determined by the morphology of the system. For strong aggregates, the value of A can become quite large while φ_m of the dispersed phase will decrease.

$$A = k_E - 1 \tag{11}$$

Figure 9 represents the Young's modulus of all the investigated samples, together with Nielsen's model fittings. The values of the A and φ_m used to predict the relationship between the experimental and theoretical moduli were 2.0 and 0.35 respectively for the composites prepared in the absence of TESPT. For the composites prepared in the presence of TESPT, the values of A and φ_m were 3.5 and 0.2. The *in situ* generation of silica particles by a non-hydrolytic sol-gel route obviously reduced the silica particle size and improve its dispersion in EPDM compared to our previous work using the hydrolytic sol-gel route [16, 17]. The non-hydrolytic route seems to overcome the typical problems related to

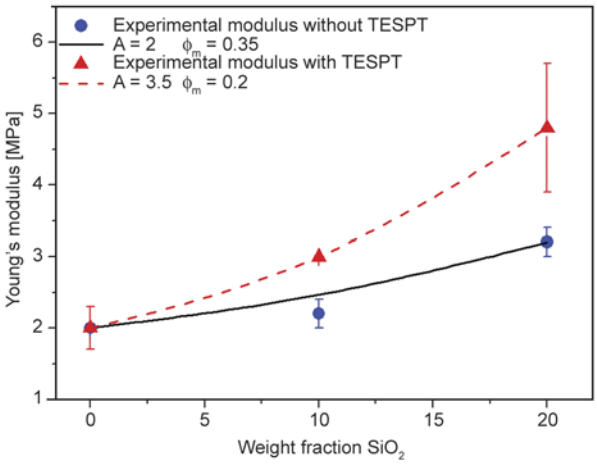

Figure 9. Young's modulus as a function of weight fraction of SiO_2 in EPDM/SiO_2 composites (▲) with TESPT and (●) without TESPT: experimental modulus and Nielsen's model fittings

hydrolytic route, in which the low miscibility of the sol-gel aqueous system limits the dispersion and distribution of the filler in the matrix. The low value of φ_m indicates the presence of agglomerated silica particles, but the aggregates are small enough for the value of A to be fairly small. The composites prepared in the presence of TESPT shows a better Nielsen's model fit and higher Young's modulus values than the composites prepared in absence of TESPT. This is in line with the smaller particles and better dispersion observed in the TEM images in Figure 2. Smaller particles and better dispersion will improve the matrix-filler interaction and increase the rubber reinforcement, giving rise to higher tensile modulus values.

The stress and elongation at break values observably increase with increasing silica content for all the EPDM/SiO_2 composites compared to those of the neat EPDM (Table 3). This indicates good reinforcement and is the result of improved adhesion between the filler and the matrix giving rise to effective stress transfer. For 10 wt% of filler the stress and elongation at break values increased, but for 20 wt% filler these values decreased, but they are still higher than that of pure EPDM. The reason for this observation is the agglomeration of the silica particles in the 20 wt% filled composite. The composites prepared in the presence of TESPT have significantly higher stress at break, but lower elongation at break, values than the comparable composites prepared in the absence of TESPT. The most probable explanation for the lower elongation at break for the samples prepared in the presence of TESPT is

Table 3. Summary of tensile results of EPDM and EPDM/SiO_2 composites

Samples	E [MPa]	σ_b [MPa]	ε_b [%]
EPDM	2.0±0.3	1.6±0.3	589±43
Unmodified composites			
90/10 w/w EPDM/SiO_2	2.2±0.2	4.9±2.1	2863±101
80/20 W/W EPDM/SiO_2	3.2±0.2	3.4±0.3	1865±35
TESPT modified composites			
90/10 w/w EPDM/SiO_2	3.0±0.0	10.0±1.6	1570±14
80/20 W/W EPDM/SiO_2	4.8±0.9	4.4±2.1	963±10

E, σ_b and ε_b, are the modulus, stress at break and elongation at break

Table 4. Percentage change in stress and elongation at break with change in reaction route and with addition of TESPT

Changes in the reaction route (80/20 w/w EPDM/SiO_2)	σ_b [MPa]	ε_b [%]
HSG → NHSG in the absence of TESPT	2.9 → 3.4	956 → 1865
HSG → NHSG in the presence of TESPT	3.7 → 4.4	1060 → 963
Presence of TESPT for HSG	3.7	1060
Presence of TESPT for NHSG	4.4	963

that TESPT probably settled on the interface between the silica particles and EPDM and did not form part of the network. Table 4 shows the differences between the stress and elongation at break values of the samples prepared according to the HSG and NHSG routes, and in the absence and presence of TESPT. The change in the reaction route from HSG to NSHG shows increased σ_b and ε_b values as a result of smaller particles and better particle-matrix interactions. However, when TESPT was present, the same change in reaction route only improved the stress at break, but reduced the elongation at break. The reason for this is the fact that during the HSG route the TESPT takes part in the sol-gel reaction and becomes part of the crosslinked network, while during the NHSG route it does not take part in the sol-gel reaction and only sits on the EPDM-silica interface.

Values obtained from dynamic mechanical analysis (DMA) are summarized in Table 5. The filler effectiveness (Factor C) in the rubber matrix can be evaluated from the values of the storage modulus obtained in the glassy and rubbery regions by using Equation (12) [27]:

$$\text{Factor C} = \frac{\left(\frac{E'_g}{E'_r}\right)\text{composites}}{\left(\frac{E'_g}{E'_r}\right)\text{matrix}} \tag{12}$$

where, E'_g and E'_r are the storage moduli determined in the glassy and rubbery regions, respectively. The state of filler dispersion in the rubber matrix was determined by calculation of the damping reduction (DR) from the damping values obtained from the normalized $\tan\delta$ peaks ($(\tan\delta)_{EPDM}$ and $(\tan\delta)_{composite}$) and is given by Equation (13) [30]:

$$DR = \frac{(\tan\delta)_{EPDM} - (\tan\delta)_{composite}}{(\tan\delta)_{EPDM}} \cdot 100 \tag{13}$$

The DMA results of EPDM and its nanocomposites are shown in Figures 9 and 10. The glass transition temperature, the $\tan\delta$ value at the glass transition peak maximum, the storage modulus at –80 and 20°C, Factor C and the damping reduction values are summarized in Table 5. The storage modulus values in the glassy region increase with increasing silica content (see E'_T = –80°C values in Table 5). There

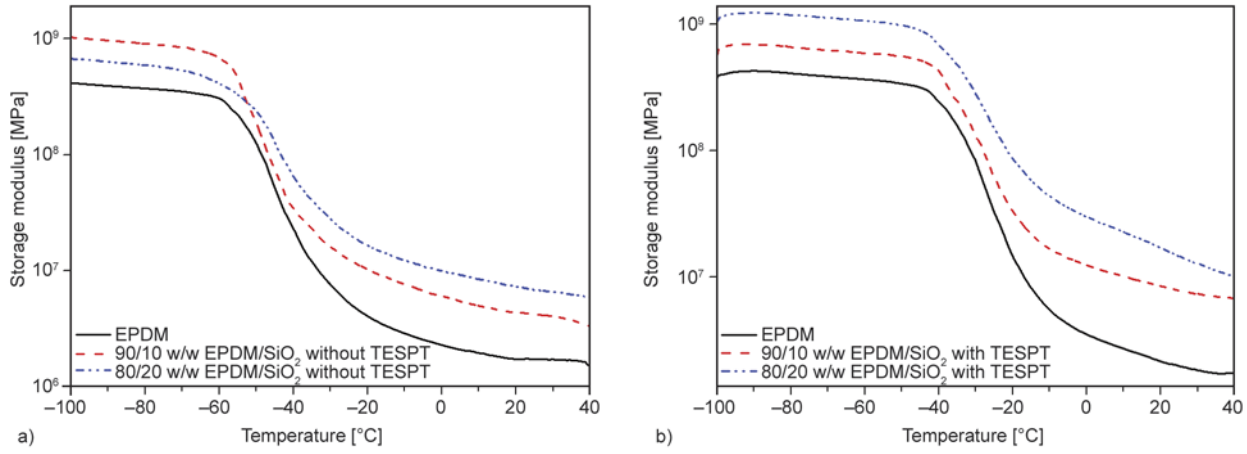

Figure 10. DMA storage modulus curves of EPDM and composites (a) without TESPT and (b) with TESPT

is also a significant increase in the storage modulus with increasing silica content in the rubbery region (see E'_T = 20°C values in Table 5 and shown in Figure 10). These modulus values depend on (i) the degree of crosslinking of the rubber, (ii) the content of the rigid dispersed phase, and (iii) the sizes of the filler particles. All these factors will contribute to an increase in the modulus. As can be seen from Table 1, the degree of crosslinking decreased with increasing silica content. However, the presence of the rigid dispersed silica particles and their interaction with EPDM reduced the chain mobility and increased the stiffness of the rubber to such an extent that the effect of the reduced crosslinking was not observable. The increase in agglomeration at higher silica content may also have contributed to the increase in modulus. Furthermore, the modulus values of the composites prepared in the presence of TESPT are significantly higher than those of the comparable composites prepared in the absence of TESPT and this is also observed in Figure 10. This is in line with the already discussed Young's modulus values. The $(\tan\delta)_{max}$ values in (Figure 11 and Table 5) clearly decrease with increasing silica content for the composites prepared in the absence and presence of TESPT, and they are lower for the samples prepared in the presence of TESPT. This is attributed to good adhesion between the filler and the matrix, which resulted in a restriction in the rubber chain mobility in the composites. The damping reduction (DR^{Norm}) values, which increased with both increasing silica content and with TESPT treatment, confirm the stronger interaction of EPDM with smaller and well dispersed silica particles which led to a reduction in the polymer chain mobility. However, the glass transition temperature (T_g) decreased for the 10 wt% silica-containing samples (Table 5), but again increased for the 20 wt% silica-containing samples. Reduced crosslinking should decrease the value of T_g, while the presence of the silica particles and their interaction with EPDM should reduce the mobility of the rubber chains and increase the value of T_g. In the case of the 10 wt% silica containing samples the reduced crosslinking seems to have a dominant effect, while the effect of chain immobilization by the silica particles is more dominant in the case of the 20 wt% silica containing samples.

Table 5. Summary of DMA results of EPDM and EPDM/SiO_2 composites with and without TESPT

Samples (w/w)	$E'_{-80°C}$ [MPa]	$E'_{20°C}$ [MPa]	$(\tan\delta)_{max}$	T_g [°C]	DR^{Norm} [%]	Factor C
EPDM	4.1	1.7	0.5188	–41.0	–	1.00
Unmodified composites						
90/10 EPDM/SiO_2	9.1	4.2	0.5197	–46.7	–0.17	1.21
80/20 EPDM/SiO_2	5.9	6.8	0.4405	–42.1	15.10	0.38
TESPT modified composites						
90/10 EPDM/SiO_2	6.6	6.9	0.4378	–44.3	15.60	0.45
80/20 EPDM/SiO_2	11.8	9.9	0.3958	–42.5	23.70	0.57

$E'_{-80°C}$, $E'_{20°C}$, $(\tan\delta)_{max}$, T_g, Factor C and DR are the modulus values at –80 and 20°C, maximum tan δ (normalised to the amount of rubber in the nanocomposites), glass transition temperature, filler effectiveness and the damping reduction (calculated from $(\tan\delta)_{max}$)

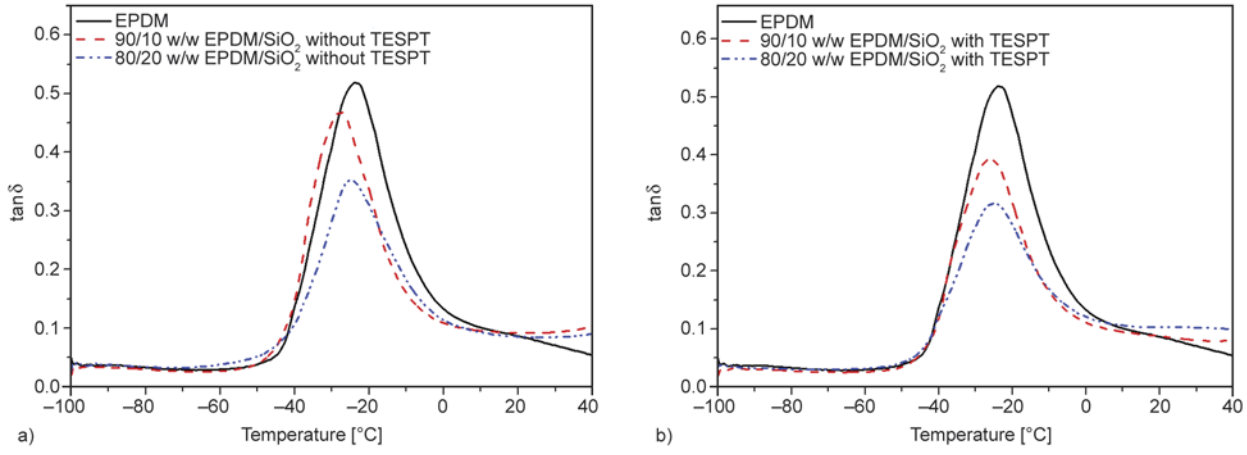

Figure 11. DMA damping factor curves of EPDM and composites (a) without TESPT and (b) with TESPT

Table 6. Storage modulus at 40°C of EPDM/SiO_2 nanocomposites prepared according to the HSG and NHSG routes in the absence and presence of TESPT

$E'_{T = 40°C}$ [MPa]	
Hydrolytic sol-gel (HSG) route without TESPT	
90/10 w/w EPDM/SiO_2	80/20 w/w EPDM/SiO_2
6.7	12.3
Hydrolytic sol-gel (HSG) route with TESPT	
90/10 w/w EPDM/SiO_2	80/20 w/w EPDM/SiO_2
8.2	8.8
Non-hydrolytic sol-gel (NHSG) route without TESPT	
90/10 w/w EPDM/SiO_2	80/20 w/w EPDM/SiO_2
4.2	6.8
Non-hydrolytic sol-gel (NHSG) route with TESPT	
90/10 w/w EPDM/SiO_2	80/20 w/w EPDM/SiO_2
6.7	9.9

$E'_{40°C}$, storage modulus value at 40°C

Table 6 shows the storage modulus values in the rubbery region at 40°C for the EPDM/SiO_2 composites prepared according to the HSG and NHSG routes in the absence and presence of TESPT. Generally, comparable composites prepared according to the HSG route show higher storage modulus values than the composites prepared according to the NHSG route. The reason for this is probably that the TESPT formed part of the network structure for the samples prepared according to the HSG route, while it sat on the EPDM-silica interface for the samples prepared according to the NHSG route, to some extent acting as a plasticizer.

The filler effectiveness (Factor C) can be used to indicate the composite reinforcing capacity. By definition an unfilled rubber matrix has a Factor C equal to 1, and a Factor C lower than 1 indicates a mechanical stiffening effect as well as a thermal stability contribution of the used filler [27]. The values in Table 5 show that the silica particles improved the stiffness of EPDM. However, the 90/10 w/w EPDM/SiO_2 composite shows values that are not in line with the rest of the values. This is the result of the high storage modulus values obtained at temperatures below the glass transition temperature. This result was found to be reproducible, and therefore it is not possible to offer an explanation at this point in time.

4. Conclusions

Non-hydrolytic sol-gel synthesis of EPDM-silica composites prepared in the absence and presence of a coupling agent was investigated. The TEM results showed that in the absence of TESPT the silica particles were homogeneously and fairly well dispersed, but with clear evidence of particle agglomeration and much larger agglomerates were visible at high silica content (20 wt%). The introduction of TESPT reduced the particle-particle interaction, and gave rise to much reduced agglomeration and observably better dispersion. The presence of silica particles inhibited the crosslinking density of the vulcanized EPDM matrix for all the composites prepared in the absence and presence of TESPT. The reduced crosslinking density of the composites prepared in the absence of TESPT was caused by reduced amounts of DCP available to initiate crosslinking, because the DCP was partially utilised in the grafting of silanol groups onto the rubber chains. In the case of the composites prepared in the presence of TESPT, the decline was due to the coupling agent that probably settled on the interface between the silica particles and EPDM and did not form part of the network. This caused enough free volume between the chains to accommodate the toluene molecules during swelling, and resulted in an increase in the swelling ratio.

The thermal stability of the EPDM/SiO_2 composites showed two mass loss steps for all the composites. The mass loss in the range 100–400°C was caused by the evaporation of ethylene chloride and other acid chlorides present in the composites, as well as the evaporation of TESPT that settled on the interface between the silica particles and EPDM for composites prepared in the presence of TESPT.

The Nielsen fitting of the Young's modulus indicated smaller and better dispersed filler particles for the NSHG route, and this further improved when the preparation was done in the presence of TESPT. Improved stress at break was observed as a result of improved EPDM-silica interactions that led to better stress transfer. However, the elongation at break was lower for the samples prepared in the presence of TESPT, probably because TESPT settled on the interface between the silica particles and EPDM and did not form part of the network. The DMA results supported the observations and conclusions from the other techniques.

In summary, the NHSG route generally gave rise to smaller and better dispersed filler particles than the HSG route, and this was reflected in the investigated thermal and mechanical properties of the composites. However, the presence of TESPT during the sol-gel preparation had a much smaller influ-

ence in the NHSG route. This is probably because TESPT did not take part in the sol-gel reaction and only settled on the interface between EPDM and the silica particles, as was established from a thermal degradation analysis of the samples.

Acknowledgements

The National Research Foundation in South Africa and the Italian Ministry of Foreign Affairs (Italy-South Africa bilateral collaboration project) are acknowledged for financial support of the project.

References

[1] Morselli D., Bondioli F., Fiorini M., Messori M.: Poly (methyl methacrylate)–TiO_2 nanocomposites obtained by non-hydrolytic sol–gel synthesis: The innovative *tert*-butyl alcohol route. Journal of Materials Science, **47**, 7003–7012 (2012).
DOI: 10.1007/s10853-012-6651-4

[2] Morselli D., Messori M., Bondioli F.: Poly(methyl methacrylate)–TiO_2 nanocomposite obtained by non-hydrolytic sol–gel synthesis. Journal of Materials Science, **46**, 6609–6617 (2011).
DOI: 10.1007/s10853-011-5610-9

[3] Morselli D., Bondioli F., Sangermano M., Messori M.: Photo-cured epoxy networks reinforced with TiO_2 *in-situ* generated by means of non-hydrolytic sol–gel process. Polymer, **53**, 283–290 (2012).
DOI: 10.1016/j.polymer.2011.12.006

[4] Mutin P. H., Vioux A.: Nonhydrolytic processing of oxide-based materials: Simple routes to control homogeneity, morphology, and nanostructure. Chemistry of Materials, **21**, 582–596 (2009).
DOI: 10.1021/cm802348c

[5] Debecker D. P., Mutin P. H.: Non-hydrolytic sol–gel routes to heterogeneous catalysts. Chemical Society Reviews, **41**, 3624–3650 (2012).
DOI: 10.1039/C2CS15330K

[6] Lafond V., Mutin P. H., Vioux A.: Non-hydrolytic sol–gel routes based on alkyl halide elimination: Toward better mixed oxide catalysts and new supports: Application to the preparation of a SiO_2–TiO_2 epoxidation catalyst. Journal of Molecular Catalysis A: Chemical, **182–183**, 81–88 (2002).
DOI: 10.1016/S1381-1169(01)00487-3

[7] Niederberger M.: Nonaqueous sol–gel routes to metal oxide nanoparticles. Accounts of Chemical Research, **40**, 793–800 (2007).
DOI: 10.1021/ar600035e

[8] Lind C., Gates S. D., Pedoussaut N. M., Baiz T. I.: Novel materials through non-hydrolytic sol-gel processing: Negative thermal expansion oxides and beyond. Materials, **3**, 2567–2587 (2010).
DOI: 10.3390/ma3042567

[9] Arnal P., Corriu R. J. P., Leclercq D., Mutin P. H., Vioux A.: A solution chemistry study of nonhydrolytic sol–gel routes to titania. Chemistry of Materials, **9**, 694–698 (1997).
DOI: 10.1021/cm960337t

[10] Hay J. N., Raval H. M.: Synthesis of organic–inorganic hybrids via the non-hydrolytic sol–gel process. Chemistry of Materials, **13**, 3396–3403 (2001).
DOI: 10.1021/cm011024n

[11] Wu Y-P., Jia Q-X., Yu D-S., Zhang L-Q.: Modeling Young's modulus of rubber–clay nanocomposites using composite theories. Polymer Testing, **23**, 903–909 (2004).
DOI: 10.1016/j.polymertesting.2004.05.004

[12] Jayasree T. K., Predeep P.: Effect of fillers on mechanical properties of dynamically crosslinked styrene butadiene rubber/high density polyethylene blends. Journal of Elastomers and Plastics, **40**, 127–146 (2008).
DOI: 10.1177/0095244307083865

[13] Ahmed S., Jones F. R.: A review of particulate reinforcement theories for polymer composites. Journal of Materials Science, **25**, 4933–4942 (1990).
DOI: 10.1007/BF00580110

[14] Nielsen L. E.: Morphology and the elastic modulus of block polymers and polyblends. Rheologica Acta, **13**, 86–92 (1974).
DOI: 10.1007/BF01526889

[15] Nielsen L. E., Landel R. F.: Mechanical properties of polymers and composites. Marcel Dekker, New York (1994).

[16] Mokhothu T. H., Luyt A. S., Morselli D., Bondioli F., Messori M.: Influence of *in situ*-generated silica nanoparticles on EPDM morphology, thermal, thermomechanical, and mechanical properties. Polymer Composites, in press (2014).
DOI: 10.1002/pc.23002

[17] Mokhothu T. H., Luyt A. S., Messori M.: Reinforcement of EPDM rubber with *in situ* generated silica particles in the presence of a coupling agent *via* a sol–gel route. Polymer Testing, **33**, 97–106 (2014).
DOI: 10.1016/j.polymertesting.2013.11.009

[18] Messori M., Bignotti F., De Santis R., Taurino R.: Modification of isoprene rubber by *in situ* silica generation. Polymer International, **58**, 880–887 (2009).
DOI: 10.1002/pi.2606

[19] Ikeda Y., Kemeda Y.: Preparation of 'green' composites by the sol-gel process: *In situ* silica filled natural rubber. Journal of Sol-Gel Science and Technology, **31**, 137–142 (2004).
DOI: 10.1023/B:JSST.0000047975.48812.1b

[20] Prasertsri S., Tattanasom N.: Mechanical and damping properties of silica/natural rubber composites prepared from latex system. Polymer Testing, **30**, 515–526 (2011).
DOI: 10.1016/j.polymertesting.2011.04.001

[21] Wang H., Zhong W., Xu P., Du Q.: Polyimide/silica/titania nanohybrids via a novel non-hydrolytic sol–gel route. Composites Part A: Applied Science and Manufacturing, **36**, 909–914 (2005).
DOI: 10.1016/j.compositesa.2004.12.008

[22] Zhu D., Van Ooij W. J.: Structural characterization of bis-[triethoxysilylpropyl]tetrasulfide and bis-[trimethoxysilylpropyl]amine silanes by Fourier-transform infrared spectroscopy and electrochemical impedance spectroscopy. Journal of Adhesion Science and Technology, **16**, 1235–1260 (2002).
DOI: 10.1163/156856102320256873

[23] Motaung T. E., Luyt A. S., Thomas S.: Morphology and properties of NR/EPDM rubber blends filled with small amounts of titania nanoparticles. Polymer Composites, **32**, 1289–1296 (2011).
DOI: 10.1002/pc.21150

[24] Barra G. M. O., Crespo J. S., Bertolino J. R., Soldi V., Pires A. T. N.: Maleic anhydride grafting on EPDM: Qualitative and quantitative determination. Journal of the Brazilian Chemical Society, **10**, 31–34 (1999).
DOI: 10.1590/S0103-50531999000100006

[25] Hussain A. I., Tawfic M. L., Khalil A. A., Awad T. E.: High performance emulsified EPDM grafted with vinyl acetate as compatibilizer for EPDM with polar rubber. Nature and Science, **8**, 348–357 (2010).

[26] Hsieh T. H., Kinloch A. J., Masania K., Lee J. S., Taylor A. C., Sprenger S.: The toughness of epoxy polymers and fibre composites modified with rubber microparticles and silica nanoparticles. Journal of Materials Science, **45**, 1193–1210 (2010).
DOI: 10.1007/s10853-009-4064-9

[27] Gregorova A., Machovsky M., Wimmer R.: Viscoelastic properties of mineral-filled poly(lactic acid) composites. International Journal of Polymer Science, **2012**, 252981/1–252981/6 (2012).
DOI: 10.1155/2012/252981

eXPRESS Polymer Letters Vol.8, No.11 (2014) 823–840
Available online at www.expresspolymlett.com
DOI: 10.3144/expresspolymlett.2014.84

Monitoring the production of FRP composites: A review of *in-line* sensing methods

S. Konstantopoulos[1*], *E. Fauster*[2], *R. Schledjewski*[1,2]

[1]Christian Doppler Laboratory for Highly Efficient Composites Processing, Otto Glöckel-Straße 2/I, 8700 Leoben, Austria
[2]Chair of Processing of Composites, Department of Polymer Engineering and Science Montanuniversität, Otto Glöckel-Straße 2/III, 8700 Leoben, Austria

Received 28 April 2014; accepted in revised form 8 June 2014

Abstract. Composites manufacturing is characterized by many degrees of freedom. Different materials, geometries and thermo-dynamical conditions contribute to a behavior that is difficult to predict. Monitoring the running process (*in-line* monitoring) eliminates the need for prediction; real time data provided by appropriate sensing systems can be used in the direction of process optimization, quality upgrade or material characterization. The aim of the review at hand is to record and discuss the latest progress in the field of *in-line* composites monitoring with a focus on Fiber Reinforced Polymeric-based (FRP) composite structures. Summaries of each sensor's principles of operation, appropriate association with polymer/composite properties detection, brief descriptions of representative studies, a critical overview of implementation aspects and discussion on the upcoming trends, contribute in constructing a complete picture.

Keywords: *material testing, cure monitoring, flow-front detection*

1. Introduction

Any composite part is generally characterized by a certain production cost, quality and in-production material behavior. Research areas around each of these topics have been developed in the past years. Naturally, the industry has a high interest in minimizing production costs. In composites manufacturing cost is related to the curing cycle time, adaptivity to batch-to-batch variations, reproducibility, etc. In principle such aspects fall under the field of process optimization. The quality of the final part is highly dependent on the filling and curing processes; filling defects (porosity, dry spots etc.) or cure-induced defects (degradation, under-curing etc.) are considered as a threat to the structural health of the component. Quality upgrade is the area that works in the direction of eliminating defects. Finally, the mechanisms that dominate filling and curing differ depending on the process inputs (materials, geometry and thermo-dynamical conditions). The field that is focused in investigating the material mechanisms with respect to process inputs and theory, is material characterization.

These research areas are distinct yet overlapping; hardly does a study focus in only one of them. Since *in-line* monitoring serves all three of these territories, it acts as a tool to inter-connect them. The work that has been done in the past in the direction of evaluating the various *in-line* monitoring techniques is rather limited. In 1991 Huntson [1] made one of the first approaches in evaluating technologies developed in the 80's to monitor composites manufacturing. In 2003 Mulligan [2] and Summerscales [3] contributed by reviewing mainly advancements of the 90's on *in-line* monitoring systems for both composites and adhesives. A review of Fon-

*Corresponding author, e-mail: spiridon.konstantopoulos@unileoben.ac.at

Table 1. Detectability chart of sensors monitoring composites manufacturing

		Flow front	Curing degree	Void content	Delaminations
Electromagnetic properties	Dielectric analysis (DEA)	✓	✓	✓	✓
	Direct Current (DC) analysis	✓	✓		
	Electrical time domain reflectometry (ETDR)	✓	✓		
Mechanical properties	Optical fiber interferometers (OFI)	✓	✓		
	Ultrasonic transducers	✓	✓	✓	✓
Optical properties	Optical fiber refractometers (OFR)	✓	✓		
	Spectrometers	✓	✓		
Thermo-dynamical properties	Thermometers	✓	✓		✓*
	Pressure transducers	✓			

*Only by Infrared (IR) thermography

seca *et al.* [4] in 2009 focuses on sensors appropriate for neat polymer monitoring in polymerization reactors, not composites manufacturing; yet their work offers valuable input due to the overlapping sensing technologies. Significant input to all chapters of this project were the handbooks of Webster [5] and Fraden [6] that offered concentrated knowledge on measuring and sensing, while the encyclopedic coverage of polymers by Chanda and Roy [7] provided the essential link between sensing and polymer technology.

Technology leaps, commercialization of sensors and production standardization, gave a boost to industrial *in-line* monitoring implementations. Meanwhile, novel approaches in composites monitoring add continuously to the conquered knowledge. This work aims to serve the need of recording and assessing the advances of the new millennia. A starting point is Table 1 that contains the main sensing methods and their corresponding detection capabilities, categorized by the material property groups. It serves as a roadmap for section 2 that includes summaries of sensing technologies and representative applications in composites manufacturing. More practical aspects of each sensor are discussed in section 3.2 and summarized in Table 2.

2. Sensing systems

2.1. Sensors detecting electromagnetic properties

2.1.1. Dielectric analysis (DEA)

An AC excited circuit generates an electrical field between parallel plates (homogeneous field, Figure 1a) or interdigitated electrodes (fringing electric field or FEF, Figure 1b). The field causes electronic, atomic, dipole polarization and ion migration phenomena to the material within, the last two being

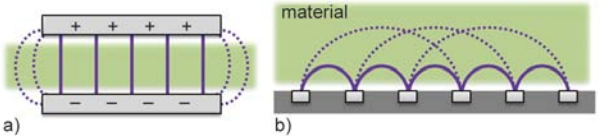

Figure 1. (a) Parallel plate and (b) interdigitated electrodes that create homogeneous and fringing electric fields respectively

the only measurable by DEA. Reorientation of the dipolar molecules (dipole polarization) and migration of ions with the external field frequency (ω), result in a resistive (energy loss) and capacitive (energy storage) behavior [8]. The complex dielectric permittivity (ε^*) of a dielectric material is a measure of its resistive and capacitive signature; it is expressed by Equation (1) where the real part of dielectric permittivity (ε') is related to the stored energy within the medium and the imaginary or dielectric loss (ε'') is related to the energy dissipated within the medium. Both the real and imaginary parts can have a dipolar and an ionic component.

The ionic component of the dielectric loss (ε'') dominates the total dielectric loss in certain frequencies. Furthermore, it is dependent on the ion resistivity or ion viscosity (ρ) (Equation (2)) which is typically the monitoring quantity in polymeric materials due to its strong correlation with the polymeric matrix viscosity (η) (Equation (3)) (as viscosity increases, volume loss in the micro-space indicates an increase in disturbance of ionic movement). Based on these dependencies, a sensing system able to monitor the dielectric permittivity can not only give valuable information on the degree of conversion, viscosity and flow front, but also introduce to the user the possibility of frequency selection for characterization on the frequency domain (dielectric spectroscopy).

$$\varepsilon^*(\omega) = \varepsilon'(\omega) - j\varepsilon''(\omega) \quad (1)$$

$$\varepsilon''_i = \frac{1}{\rho\omega\varepsilon_0} \quad (2)$$

$$\rho = \frac{6\pi r\eta}{Ze^2N} \quad (3)$$

Lee and Kim [9] investigated the dielectric loss behavior of composites produced in an Autoclave. FEF sensors with a constant frequency, recorded the $\varepsilon''(T)$ profile. Comparison with DSC (differential scanning calorimetry) showed that the temperature range of the loss curve did not coincide with the temperature range of the curing reaction. The two ranges however, did overlap which enabled the authors to derive geometrically a correlation between the loss, the temperature and the curing degree.

Hegg *et al*. [10] used parallel plate and FEF sensors to monitor filling within a Resin Transfer Moulding (RTM) tool with a transparent top tool. Although parallel plate sensors showed a linear increase in capacitance as the flow progressed, fringing effects at the sensor edges created a small difference (maximum 5 mm) between visual and dielectric data; repeating with FEF sensors eliminated the discrepancy.

Yenilmez and Sozer [11] developed an RTM mould with integrated rectangular electrodes in the cavity walls. The electrodes on the top tool were perpendicular to the ones on the bottom tool resulting this way to fifty measuring points at the cross-linking areas. Single frequency AC excitement resulted in relative permittivity measurements which served finally as the monitoring quantity for both flow (instantaneous increase upon resin arrival) and cure (gradual drop throughout conversion) during manufacturing of polyester/glass and epoxy/glass composites with various fiber volume and catalyst contents.

Kim *et al*. [12] embedded an FEF sensor between carbon/epoxy prepregs used in composite plate manufacturing by compression moulding. The sensor was excited by a single frequency and the obtained dielectric loss measurements followed closely viscosity changes. Critical process points such as the start and end of cure were determined by the ε'' time derivative maximum and minimum values respectively.

Kobayashi *et al*. [13] developed a flexible area sensor with multiple FEF elements. The system was patched on CFRP composites under fabrication aiming to monitor superficial curing gradients and operated in a variety of exciting frequencies. A novel correlation of dielectric measurements with the material state was proposed and used; it is based on the relation between viscosity and the frequency dependence of permittivity. The approach was confirmed by agreement with DSC measurements.

2.1.2. Direct current (DC) analysis

A DC electrical circuit specifically designed for resistance measurements is initially open. The Material Under Test (MUT) acts as an electrically conductive medium between the open points. As it closes the circuit, a voltage output proportional to the ion viscosity (ρ) is generated. The mathematical correlation between ρ and the output voltage is not strictly defined as it depends on the electrical circuit design; options vary from a simple voltage divider to a complex circuit with amplification or other enhancements. However, the association between ion viscosity and matrix viscosity discussed for DEA (Equation (3)) applies to DC analysis as well because ion migration remains the dominant mechanism in DC excited polymers [14].

Despite the DC and AC circuits overlapping mathematical descriptions, a significant difference remains; DC sensing offers only time domain analysis in contrast to DEA that can expand in the frequency domain and produce richer measurements. In practice, this disadvantage is counterbalanced by the straightforward and low cost DC based systems. Implementation of DC analysis in composites is typically achieved either by in or out-of-plane electrodes that can measure the resin or composite electrical resistance (Figure 2).

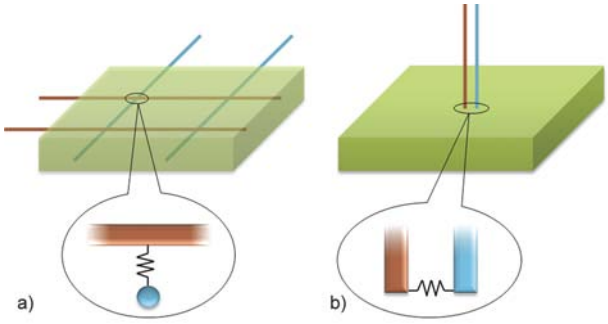

Figure 2. Measurements of the electrical resistance between the exciting (brown) and sensing (blue) electrodes arranged in (a) the in-plane electrode configuration known as the SMARTweave™ and (b) out-of-plane configuration

Lawrence *et al*. [15] optimized filling in a complex RTM tool via a multiple gate injection system. Filling simulations were used to predict the dry spot locations around which auxiliary gates were opened and point DC sensors were mounted; they provided real time resin arrival information which was input in a decision making algorithm. A fully automated injection machine with pneumatic grips that open/closed vents and gates realized the taken decision. Comparison between parts produced by controlled and non-controlled processes, showed that the multiple injection prevented the formation of dry spots. Luthy and Ermanni [16] developed a variation of the SMARTweave™ method where the sensing and exciting fibrous in-plane electrodes within the preforms are parallel. As the matrix filled the space between them, an electrical signal proportional to the flow front was generated and a model based flow front position was deduced. Difficulties to maintain a constant distance between the fibrous electrodes lead the authors to develop a plate with multiple printed electrodes which however demanded sampling that deteriorated the time domain resolution. Relevant experimentation showed small deviations from the visual detection.

Danisman *et al*. [17] focused on the development of flow detecting DC sensors and appropriate circuitry for signal conditioning. The prototype with concentric electrodes that operated as a Boolean point sensor was proven to be the most practical for mould integration. To validate, multiple sensors of this type were mounted in an RTM mould and monitored filling experiments. The obtained flow front was verified visually through the transparent top tool.

Garschke *et al*. [18] investigated the impregnation and cure cycle for Resin Film infusion (RFI) processes. Heating scenarios with different dwell times and heating rates were monitored by a point DC sensor inserted in the vacuum bag. The resistance measurements were correlated to viscosity by a novel model which showed that short dwelling and high rates result in significant cycle reduction but not without increased void formation. However, degassing at elevated temperatures was able to reduce void formation to acceptable levels.

Hsiao [19] derived the thermomechanical behavior of a curing epoxy resin using a single carbon fiber embedded in it. Electrical resistance and the thermal history revealed the T_g corresponding to the abrupt change in the coefficient of thermal expansion, the T_g by the storage modulus (E') onset, and the upper temperature limit for linear E'–T relationship. Comparison with the same quantities obtained by dynamic mechanical analysis (DMA) and thermomechanical analysis (TMA) showed good agreement.

2.1.3. Electric time domain reflectometry (ETDR)

A high frequency electromagnetic voltage pulse E_i that is driven through a pair of conductors (transmission line), creates electrostatic and magnetic fields around them (Figure 3). The dynamical behavior of material within the field expressed as a discontinuity, causes a reflection waveform (E_d) that requires finite time to travel back through the lines [20]. The ratio of the incident to the reflection pulse or the electric reflection coefficient (R_e) is a function of the electrical impedance at the discontinuity location Z_d (Equation (4)). The latter is dependent on both the geometry of the transmission line and the state of the material they are placed in [21].

In composites monitoring, the flow front acts as a discontinuity along the transmission lines that given constant real dielectric permittivity and magnetic permeability (ε' and μ') during filling, can be located spatially by measuring the time of flight of the reflected wave (Equation (5)). On the other hand, curing can be detected by changes in the reflection amplitude imposed by the contributions of ε' and μ' in the electrical impedance of the measured discontinuity (Equation (6)). Equations (5) and (6) apply under the assumption that the resistance of the transmission lines and the conductance of the material within the field are negligible (lossless transmission).

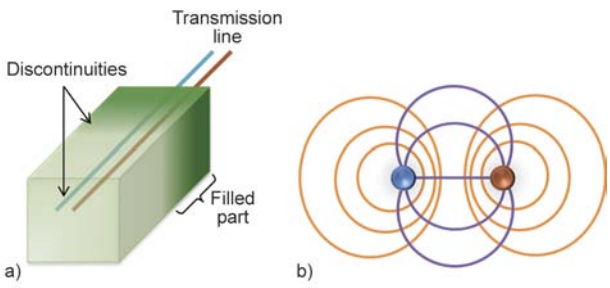

Figure 3. (a) The flow front along the transmission line acts as a reflective interface for the electromagnetic pulse. (b) The electric (purple) and magnetic (orange) field lines around the transmission line electrodes.

$$R_e = \frac{E_d}{E_i} = \frac{Z_d - Z_0}{Z_d + Z_0} \quad (4)$$

$$x = ut = \frac{1}{\sqrt{\varepsilon' \mu'}} t \quad (5)$$

$$Z = K\sqrt{\frac{\mu'}{\varepsilon'}} \quad (6)$$

Pandey *et al*. [22] integrated two parallel electrodes on a VaRTM tool as an ETDR transmission line that was used to monitor both filling and curing progression of glass/resin samples. Electrostatic simulations were used to determine the optimal distance between the electrodes with respect to maximizing sensitivity. Flow front detection during filling experiments agreed with visual data while degree of cure measurements of fast and slow curing resin systems were validated by DSC.

Dominauscas *et al*. [23] developed parallel plate and parallel wire ETDR sensors for flow detection in LCM (liquid composite molding) processes. The parallel wires exhibited higher practicality (flexibility, small size) and performance (higher reflection signal levels due to the wire insulation). Experiments with the wires embedded in the textile in parallel to the flow front showed good agreement with visual data. Multi-flow front detection with a single fiber was demonstrated by placing it perpendicularly to multiple flow fronts.

Dominauscas *et al*. [24] in a subsequent study developed a transmission line that was partially unshielded in multiple points, allowing for multiple point flow detection. The impedance discontinuity upon resin arrival at each unshielded region creates a reflection that is superimposed in the output signal. The impedance and thus the dielectric distribution is then calculated by inverting a non-uniform transmission line model. Measurements from filling experiments in a mould where a 3.8 m line with 150 sensing elements was inserted (zigzag arrangement), generally agreed with model-predicted values.

Urabe *et al*. [25] used carbon fibers to construct an ETDR transmission line that was used to monitor filling and curing of composites. The incident signal was driven through a carbon fiber strand and grounded through a carbon fiber cloth. Although the resin flow front, existence of air, progress and variation of cure were detected successfully, comparison with a metallic line showed that a carbon fiber line produces more obscure results due to the carbon higher electrical resistance.

2.2. Sensors detecting mechanical properties

2.2.1. Optical fiber interferometer (OFI)

Out of four types of optical fiber interferometers (Fabry-Pérot, Mach-Zehnder, Michelson, Sagnac), Fabry-Pérot are the most attractive for composite applications where multiple point sensing using a single fiber is of the essence. Reflective micro-surfaces along the core of a Fabry-Pérot interferometer cause partial reflection of the light that is travelling through. All reflections contribute to an interference signal characterized by a peak wavelength [26]. Thermal deformation or external strains influence significantly the spacing between the reflective surfaces and their refractive index (Figure 4). As a result environmental strain and temperature cause a shift to the peak wavelength of the reflected signal. The small diameter (typically 125 μm) and immunity to extreme conditions made the OFIs appropriate to insert in composite structures where thermal, cure induced or in-service strains can be measured.

Perhaps the most cited application of OFIs in composites is a special intrinsic Fabry-Pérot interferometer, the Fiber Bragg Grating (FBG) sensor. The reflective micro-surfaces in this case are manufactured by periodical refractive index modulations or *gratings* on one or more areas along the core of the optical fiber [27]. The reflection peak wavelength or Bragg wavelength (λ_B) is dependent on the grating distance (Λ) (Equation (7)). Modifications of Λ induced either by changes of the axial strain Δs or temperature ΔT result in a shift of the Bragg peak ($\Delta\lambda_B$) (Equation (8)):

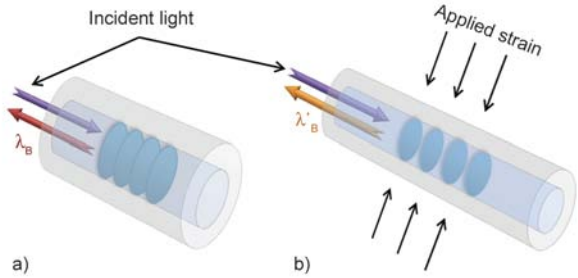

Figure 4. The increase of the grating spacing caused by the applied strain on an FBG sensor (b), results in different Bragg wavelength as compared to strain-free conditions (a)

$$\lambda_B = 2n_0\Lambda \quad (7)$$

$$\Delta\lambda_B = \lambda_B(1 - p_e)\Delta_s + \lambda_B(\alpha_e + \xi)\Delta T \quad (8)$$

Kuang *et al*. [28] used an FBG sensor to monitor the manufacturing of a novel sandwitch structure (Skin: 300 μm aluminium alloy – 300 μm fiberglass/ polypropelene, Core: 10 mm aluminium foam). The part was manufactured by compression moulding during which the embedded sensor recorded the induced strains and detected key process points. Comparison with theoretically expected strains and key points derived by DSC, showed good agreement.
Jung and Kang [29] embedded distributed FBGs in braided glass-kevlar/epoxy composites manufactured by RTM. The obtained stress signal was stabilized only after solidification immobilized the sensors. Wavelength peak split was observed which lead to using the full width at half maximum (FWHM) instead. After the stress profile was decoupled from thermal strains, it was compared with post-manufacturing mechanical tests that correlated well with FBG strains.
Khoun *et al*. [30] detected the strain profile of carbon epoxy composites during an RTM process by use of FBG sensors. The part-tool separation was detected by a difference in the thermal expansion coefficient of different FBGs in the part. The obtained stress values were used for stress simulations development. A model that assumed frictional contact at the part-tool interface agreed best with experimental values.
Archer *et al*. [31] investigated the usage of extrinsic Fabry-Pérot OFI sensors for cure induced stress monitoring. The sensors were inserted in woven carbon/epoxy composites manufactured with VaRTM and were compared with off-line rheological measurements that recreated the same conditions. A 4 and 10 min difference at the detected gelation and vitrification points respectively was observed.
Tsai *et al*. [32] examined the potential of cure monitoring by embedded FBGs in carbon/epoxy composites. Vacuum infusion experiments showed that Bragg wavelength shifts and intensity attenuation of the output signal, revealed the conversion progression. During the heating stage the glass transition temperature was detected via a change in the slope of the peak intensity versus wavelength. In the cooling stage peak splitting due to non-uniaxial stresses, was used for residual stresses calculation.

2.2.2. Ultrasonic transducers

An ultrasonic wave is a mechanical vibration in the region of 20 kHz–100 MHz, that propagates through small displacements of particles around their equilibrium positions (Figure 5c). The relative orientation of the vibration to the wave propagation defines the ultrasonic wave type (Longitudinal, Shear, Rayleigh or Lamb wave). In longitudinal and shear waves the particle vibrations are parallel and perpendicular to the wave propagation respectively. Rayleigh waves have an elliptical orbit with a symmetrical mode whereas Lamb waves have a component perpendicular to the surface. The longitudinal and shear velocities of waves propagating within isotropic material, (c_l) and (c_s), are given by Equations (9) and (10) respectively [33]. The dependency of the velocities on the density and elastic (Young's) modulus shows that within a curing matrix or composite the 'time of flight' will change as conversion progresses which allows cure monitoring.
The sound wave is also characterized by a loss of energy or *attenuation* within the media due to friction. Attenuation in composites is considered to be proportional to the impregnation quality on account of the fact that porosity and voids contribute significantly to friction-generating non-elastic responses. A measure of the attenuation is the attenuation coefficient (a), defined as the inverse ratio of change in amplitude to the initial amplitude of the transmitted wave (Equation (11)) [34]. Known configurations of ultrasonic systems are the transmission (Figure 5a) or reflection modes (Figure 5b). The latter detects wave reflections caused by discontimuities (e.g. material-mould interface) and is considered to produce signals of lower quality. This drawback is counterbalanced by the one sided access which is often of importance in composites manufacturing.

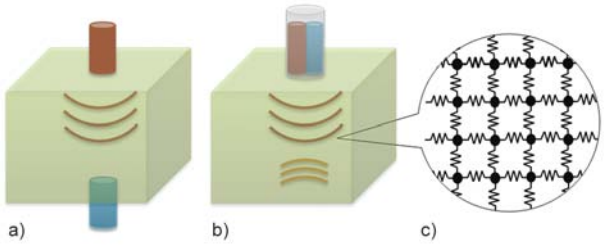

Figure 5. Ultrasonic transmitter (brown) and receiver (blue) arranged in a) transmission and b) reflection mode. The wave propagation can be modeled as the matrix oscillator (c).

$$c_l = \sqrt{\frac{E(1-\upsilon)}{d(1+\upsilon)(1-2\upsilon)}} \quad (9)$$

$$c_s = \sqrt{\frac{G}{d}} = \sqrt{\frac{E}{2d(1+\upsilon)}} \quad (10)$$

$$a = -\frac{1}{\pi\left(\frac{\Delta A}{A}\right)} \quad (11)$$

Fomitchov *et al*. [35] developed an optical fiber based ultrasonic system to monitor RTM. A beam produced by the optical fibers reached a graphite layer placed on the top of the preform. Due to rapid thermal expansion it transmitted a pulse through the composite that was detected by an embedded Sagnac OFI. Although the obtained velocity profile revealed the gelation time it did not reveal the end of cure; the velocity continued to increase post curing due to the velocity-temperature dependency.

Schmachtenberg *et al*. [36] integrated a pitch-catch ultrasonic system in an RTM mould which was used to monitor manufacturing with different reinforcements. Since the sound velocity is affected by the cross-linking process the curing stage was monitored. The amplitude is related to molecular attenuation and consequently to the impregnation quality while both signals could detect the flow front as the wave cannot propagate in dry fiber. Experiments with different pressures/flow rates that were compared with post-curing mechanical tests revealed significant enhancement of mechanical properties with the increase of amplitude maxima.

Visvanathan and Balasubramaniam [37] investigated the potential of flow front detection using ultrasonic waves propagating through a material embedded copper wire. At the wire-flow front interface the wave gets reflected/scattered through mode conversions. The time of flight of the reflected signal is used for spatial location of the flow front (the method can be considered as the equivalent of time-domain reflectometry in mechanical waves). Experimentation revealed that the reflection signal strength is proportional to viscosity, and that the wire is not without length limitations; it must be short enough to keep attenuation at acceptable levels but at the same time long enough to avoid merging with the incident signal.

Pavlopoulou *et al*. [38] utilized Lamb waves to monitor conversion of glass/epoxy composites. Uncured, semi-cured and cured samples were obtained for testing that involved 2 PZTs in pitch-catch mode. A multi-level signal conditioning procedure was followed: After Ensemble Empirical Mode Decomposition, the optimal Intrinsic Mode Function was used as input to a Hilbert Transform. The resulting weighted frequency versus time function served as the monitoring quantity; it was characterized by a monotonic increase during curing.

Liebers *et al*. [39] developed a novel ultrasonic sensor for cure monitoring for composite structures that is based on bare piezoceramic elements instead of the typical ultrasonic transducers. It was found that the liability of unstable coupling of the MUT with the transducer was no longer an issue with piezoceramic elements fixed on the mould with an adhesive layer, due to the reduction of the number of reflective interfaces. Experimenting with different piezoceramics with double or single sided access on open mould processes showed higher signal amplitudes and stability.

2.3. Sensors detecting optical properties

2.3.1. Optical fiber refractometer (OFR)

As discussed in section 2.2.1, the light travelling through an optical fiber will reflect partially when an interface is reached. Instead of e.g. gratings that the FBG sensor uses, OFRs utilize the optical fiber-MUT interface to generate the measured signal which is why direct contact of the optical fiber core with the material is essential.

In case the cladding at a certain point along the fiber is removed (evanescent OFR, Figure 6a), the signal received at the output end has reduced intensity compared to the incident signal [40]; the loss is dependent on the optical reflection coefficient (R_o). Another approach is to establish contact of the cross sectional surface of one of the ends with the MUT. The other end serves both as an input and output

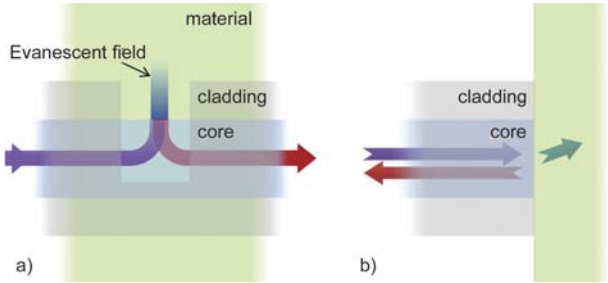

Figure 6. The evanescent (a) and Fresnel (b) optical fiber refractometers. The incident light (purple) is being reflected (red) from axial and cross section interfaces respectively.

end, the output being a reflection signal from the material-opti- cal fiber interface. The reflection signal in this case abides to Fresnel's law [41] (Fresnel OFR, Figure 6b) according to which (R_o) is a function of the refractive indexes of the interfacial materials (Equation (12)). In both cases, cure monitoring is based on the Lorentz-Lorenz law (Equation (13)) which relates the refractive index of a material to its density. As a result, an optical fiber with a bare section inserted in a composite can detect the nature (flow front) or state (curing degree).

$$R_o = \left(\frac{n_1 - n_2}{n_1 + n_2}\right)^2 \tag{12}$$

$$\frac{n^2 - 1}{n^2 + 1} = \frac{R_M}{M} d \tag{13}$$

Wang *et al*. [42] employed a Fresnel OFR to monitor the production of carbon/epoxy composites by Liquid Resin Infusion. An instant drop of the output signal indicated resin arrival while the curing stage was characterized by a gradual drop followed by a gradual increase. The signal did not cease to increase after the end of cure to shrink-induced density increase.

Lekakou *et al*. [43] used evanescent OFRs to monitor glass/epoxy composites manufacturing by Resin Infusion under Flexible Tool (RIFT). Upon resin arrival on a short bare region, a sudden intensity drop of the reflected signal was observed and confirmed optically. Experimenting with a long bare region in the flow direction showed an exponential intensity drop as the epoxy covered the core. However, at the point where the loss reaches resolution levels, the accuracy drops. During curing the reflected intensity dropped gradually and stabilized at the end of cure which coincided with the rheological end of cure determination.

Li *et al*. [44] investigated the potential of cure monitoring of Compression Moulding and Autoclave production using evanescent OFRs. In all cases the output signal followed closely the numerically expected viscosity behavior; a drop (start of cure), a rise (mid-cure) and stabilization (end of cure). Quantification of the drops and rises was not easy due to a sensitivity fluctuation of the sensor that was caused by microbends dependent on the different orientation of the sensing fiber with respect to the reinforcement fibers.

Gupta and Sundaram [45] developed a hybrid FBG – evanescent OFR sensor and used it to monitor flow in glass/epoxy specimens manufactured by Vacuum Enhanced Resin Infusion Technology (VERITy). The etched region of the optical fiber was the sensing element and the grated region was out of the part serving as a built-in transducer of the reflected signal to an interference signal. A multi-point flow detection system comprised of consecutive bare and grated regions along a single fiber was developed and experimentally validated; resin arrival was successfully detected on all bare regions.

Buggy *et al*. [46] employed two Fresnel OFRs operating in different wavelengths to monitor the curing of an epoxy resin. The measured refractive index increased rapidly after an initial decrease, indicating correlation with viscosity. Small deviations were observed between the Fresnel OFR and grating based refractometer measurements mainly due to the coupled strain/temperature effect on the latter.

2.3.2. Spectrometers

Generally, a monochromatic or polychromatic light that is directed to a media, causes electron excitement to higher electronic, vibrational or virtual states (Figure 7a). Polychromatic light in the Infrared region excites stable vibrational modes denoted by a frequency loss of the output spectra (Infrared spectroscopy). Monochromatic light typically in the ultraviolet region causes an unstable excitement to a higher electronic and possibly vibrational state. Relaxation back to the original electronic and vibrational state is realized by emitting heat and a photon of characteristic frequency (fluorescence spec-

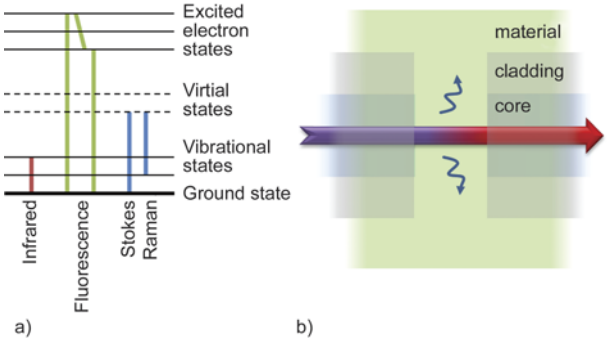

Figure 7. a) Excitation and emission scenarios typical for polymeric materials. b) Optical fiber spectrometer arranged in transmission mode, a configuration appropriate only for absorption (Infrared) and not emission (Fluorescence, Raman) spectra investigations.

troscopy). Monochromatic light that belongs to the infrared region excites to virtual states, only this time relaxation to higher vibrational modes of the ground state are characterized by photon emission that has a lower energy than the incident light (Raman spectroscopy) [47]. In all three cases, the output emission or absorption spectra characterizes the nature or state of the MUT.

Spectroscopic techniques are unique in that they do not rely on model based correlations with the material state; they detect directly the spectroscopic signature of chemical species. When applied to composites, flow can be detected by the different spectral signature of impregnated versus dry fiber while cure is monitored by detecting wavelength fluctuations or vibrations due to the cross linking process. However, spectroscopic systems are by nature mostly appropriate for laboratory testing. Towards *in-line* spectroscopy material embedded optical fiber spectrometers (OFS) are mostly employed; they are implemented either by evanescent (Figure 6a) or transmission mode optical fibers (Figure 7b) with the difference that instead of examining the output signal intensity (OFRs), OFSs examine the signal spectra. Other approaches for *in-line* spectroscopy involve remote optical fiber probes or self-sensing composites.

Wang *et al*. [48] investigated the potential of using the reinforcing glass fibers of composites as chemical sensors for cure monitoring (self-sensing composites). Experiments involving detection of the evanescent wave infrared spectra of silane-treated glass fibers embedded in epoxy resin, showed good correlation with conventional FTIR spectra for curing temperatures up to 45°C. However the silica treatment was found to affect the curing kinetics; higher curing rates but lower conversion of epoxy functional groups was observed with the increase of silane concentration.

Mahendran *et al*. [49] developed transmission mode OFS which were embedded in thermoset resins and used for cure monitoring. Simple fixtures kept the transmitting and receiving end of the optical fiber in position and infrared spectra was acquired periodically throughout conversion at various temperatures. Data from experiments at various temperatures had excellent agreement with conventional transmission spectroscopy.

Dunkers *et al*. [50] used fluorescence OFS sensors and modified glass fibers to detect filling and curing of composites in a mould with transparent lid. Long period gratings (LPGs) written at the bare regions, prevented specific wavelengths from propagating. Upon resin arrival on the bare regions, the denied wavelengths found an alternative route of propagation thus providing flow front detection. An embedded glass fiber with a fluorescently labeled silane-coupling agent (FLSCA) layer grafted on its surface, emitted a fluorescence peak that shifted as curing progressed. Experimentation showed that flow front detection deteriorated with fiber volume content increase and that there was a dependency of the fluorescence shift on the polarity of the co-silane and the layer thickness.

Wood *et al*. [51] used near-infrared OFS to monitor composite curing. The poor quality spectrum obtained by a single mode silica fiber, lead the authors to use lead doped and higher refractive index optical fibers aiming to increase the transmitted energy. Although the modified optical fiber clearly indicated a certain wavelength vibration during neat resin curing, it produced noisy results for composites. Further increase of the refractive index of the optical fiber prevented energy escape from the bare region due to complete internal reflection.

Anne *et al*. [52] employed an IR OFS with a modified core to monitor epoxy resin curing. A vibrating wavelength associated with C–O chemical bounds was clearly detected. Significant differences were observed in the curing stage allocation in the time domain between the evolution of the integrated transmission spectra and Principal Component Analysis (PCA). The latter was characterized by the authors as more reliable and reproducible. Finally, the observed absorbency correlated well with model-based predictions.

Cruz and Osswald [53] developed a high precision heating chamber with a silica window that allows remote spectroscopy. Optical fiber probes obtained repeatedly the Raman spectrum of unsaturated polyester (UP) and epoxy resin during isothermal and non-isothermal curing. A clear vibrating peak associated with C=C bonds was observed for the UP while the typical vibrating peak expected for epoxy resin suffered from overlapping; an alternative peak associated with the CH_2 stress interaction with oxygen was used instead. Although experimentation showed higher curing rates with higher pressures, post curing mechanical tests revealed that the best

mechanical properties were achieved in non-extreme pressures.

2.4. Sensors detecting thermodynamic properties

2.4.1. Thermometers

Typical instrumentation for temperature measurements in composite monitoring includes thermocouples and infrared thermometers (either point measurements or infrared thermography) while a growing experimental approach is the use of material embedded optical fiber interferometers (OFIs) with thermal decoupling. Thermocouples exploit the thermoelectric effect; they consist of two metal alloys in contact which produce a voltage proportional to the contact temperature. Infrared thermometers utilize a photosensitive cell to detect from a distance the thermal radiation emitted by a body and transduce it into an electrical signal [54]. OFIs with thermal decoupling infer the temperature by distinguishing the wavelength shift (see section 2.2.1) that is caused from thermal strains alone, in contrast to typical OFIs whose measurement contains both kinematic and thermal strain contributions.

Every operation has a different ideal; indicatively, thermocouples are commonly used due to their standardized production and performance, OFIs when a measurement of rich content (temperature, strain, pressure etc.) is aimed while infrared thermography is ideal for non-intrusive surface temperature gradients detection (e.g. open-mould or large scale processes) or in-depth imperfections (delaminations, dry spots, etc.) detection.

Temperature is of the most influential factors in composites because the polymer cross linking is a thermally activated process. A measure of the thermal effect on polymerization is often expressed by the Williams, Landel, and Ferry (WLF) dependency of viscosity on temperature (Equation (14)). Heat induced variations of viscosity define the conversion rhythm and can play a role in filling quality. However, the heating system defines the heat that reaches the material only to a certain degree; poor heating regulation, the heat capacity/thermal conductivity of the composite and the exothermic heat produced by thermoset matrices are contributing factors that need to be accounted for. Temperature monitoring aims to include all these factors in optimizing the part heating.

$$\log\left(\frac{\eta}{\eta_{T_g}}\right) = \frac{-17.44(T - T_g)}{51.6 + (T - T_g)} \tag{14}$$

Hsiao *et al*. [55] used distributed thermocouples in the interior of a polyester/glass fiber composite to monitor curing during a VaRTM process. The measurements were used to validate a model-based fitting technique consisting of a genetic algorithm optimizer and a one-dimensional cure simulator which aimed to adjust the curing kinetics on actual LCM conditions.

Tuncol *et al*. [56] used thermocouples to monitor the flow front propagation of an RTM process. Given a mould-resin temperature difference, the flow was detected reasonably fast when the mould was made of acrylic but delay was observed when an aluminium mould was used, attributed to the higher thermal diffusivity of metal. The authors advise against the usage of thermocouples for flow front detection in metallic moulds, while in non-metallic they must be used with caution.

Marin *et al*. [57] wrote a long period grating (LPG) and a Bragg grating (FBG) on the same fiber zone. The superimposed gratings result in a good discrimination of thermal and kinematic strains. To verify the accuracy in temperature detection, the sensor was used in a liquid resin infusion process for a glass/epoxy specimen. The temperature recorded during curing deviated negligibly from parallel thermocouple measurements.

Yoon *et al*. [58] wrote FBGs in two optical fibers with different dopants in the core and spliced them so that the FBGs were adjacent. The resulting sensing element discriminates efficiently thermal from kinematic strains. This ability was tested by embedding the sensor in a Kevlar/Epoxy composite with shape memory alloy (SMA) micro-wires. Very good agreement with comparative thermocouple measurements during curing was observed. Post curing activation of the SMA caused contractions which were measured by the sensor and were found to agree well with theoretically expected values.

Cuevas *et al*. [59] utilized thermal imaging to detect artificial defects as deep as six layers from the surface of both cured and uncured composite specimens. Better results were obtained with halogen lamb excitation and frequencies below 100 Hz, while signal conditioning improved detection further.

Wang *et al*. [42] distributed micro-thermocouples in the interior of carbon preforms in order to monitor

through thickness and in-plane flow movement of epoxy resin during the LRI process. An increase in temperature upon the pre-heated resin arrival in every point allowed the thermocouples to characterize the filling behavior for experiments with different heating systems. The experimental data were in agreement with simulations concerning the flow movement. However, significant deviation between the actual and predicted filling time indicated actual temperature variations that were not considered in the simulation.

2.4.2. Pressure transducers

Typically pressure sensors exploit the piezoresistive effect; a change in the electrical resistance of the sensing element upon pressure application. Alternatively, piezoelectric sensors exploit the ability of crystals to produce a flow of electric charge when elastically deformed. In either case, the sensing element is installed in a shell where the pressure under measurement and a reference pressure can be isolated. Depending on the reference pressure (vacuum, ambient or arbitary) the sensor results in different types of pressure measurements (absolute, gage or differential respectively) [5].

The significance of pressure in composites manufacturing lies on that it has a major influence on filling, a crucial stage where flow propagation discrepancies bound to affect the overall part quality can occur. Moreover due to thermodynamics it affects the curing reaction inversely to temperature. For these reasons studies focused mostly on filling behavior and filling simulations rely on pressure sensors in their experimental configurations.

Di Fratta *et al*. [60] proposed the detection of the flow front during an LCM process by use of pressure sensing combined with numerical modelling of the pressure distribution. The model can estimate the flow front in real-time with only a few pressures as input. Validation experiments of various filling scenarios in a mould with a transparent top tool and 3 pressure sensors showed good agreement with visual data.

Govignon *et al*. [61] developed a monitoring system for Resin Infusion capable of capturing dynamically the fiber volume fraction via a stereophotogrammetry unit. Complementary distributed pressure sensors correlated the pressure gradient along the preform with thickness changes and provided additional data for comparison with simulations.

Xin *et al*. [62] developed a high accuracy pressure measurement system for zero-bleeding Autoclave processes. Appropriate experimentation in Autoclave revealed a uniform pressure distribution along through-thickness and in plane directions. The pressure profile was proven to conform to the piston-spring model and to be independent of the vacuum condition while it is strongly influenced by the prepreg fiber volume fraction and compaction properties.

Simacek *et al*. [63] investigated the post filling residual flows in LCM processes with compliant tool. A previously proposed model was compared with experiments where pressure and thickness at various locations during the post filling stage are examined. There was good qualitative correlation between the model and the experimental data. Quantitative discrepancies have been observed in the prediction of the final part thickness, related to poor control, insufficient material characterization and the natural variability of the process.

Kobayashi *et al*. [64] modeled pressure fluctuations during compression moulding to predict the resin impregnation with micro-braided yarns. For validation, a mould including a pressure sensor was developed and tested in the fabrication of FRP composites. The measured pressure history was used for the analytical prediction which was confirmed by practice.

3. Discussion

3.1. Emerging trends and technologies

Undoubtedly, each and every publication takes steps towards uncharted territory, while progress in commercialization/standardization of sensing systems can be observed. Having said these general remarks, the authors comment on the overall progress and new directions of *in-line* monitoring in composite production (as compared to a decade ago), as follows:

– Structural health monitoring and smart composites* [65] motivated large volume of work on material embedded optical fibers. As a result, optical fibers have found their way in measuring *in-line* almost all kinds of material properties (electrical properties is the only exception due to the fact

*Composites that respond to environmental impacts towards preserving their safety without substantially changing their original functionality.

that optical fibers are electrically inert): Ultrasonic wave propagation, refractive index, stress, temperature, energy absorption today have all been monitored in multiple research studies with optical fiber technology.

– Material invasive sensors (optical fibers, electrodes etc.) can be a threat to structural health. Besides the typical non-invasive approach of contact sensors (DEA, Ultrasonics etc.), a clear tendency towards self-sensing composites* [66] is emerging. The most common self-sensing approach is the usage of the reinforcing carbon fiber as electrodes for electrical property sensing. Similar usage of glass fibers in optical property sensing is another possibility. Although significant work has already been done in damage detection with self-sensing [67–69], it is the belief of the authors that the first steps in *in-line* monitoring via self-sensing composites are being made at the moment by studies such as [19, 48, 50, 70].
– Electrical time-domain reflectometry (ETDR), a method based on measuring the time of flight of electrical signals, was implemented in composites for the first time. The method shows potential in *in-line* monitoring [22–24], damage detection [71–73] and self-sensing [73, 25]. Moreover, it is the only method able to detect both electric and magnetic properties. Although conventional composites are not magnetic, magnetic microwire inserts that magnetize the composite, make magnetic measurements meaningful. Research interest is attracted to polymeric composites with embedded microwires [74–77] because they are considered as a tool to develop multifunctional composites** [78, 79].

3.2. Implementation assessment of sensing systems

The problem of selecting the appropriate sensing technique for a given application is a multi-disciplinary one. Luckily technology leaps have eliminated factors that needed consideration in the past; indeed all commercially available sensors addressing composites manufacturing share a minimum of specifications related to their endurance in harsh environments, sensitivity, accuracy and digital connectivity with variations rather insignificant towards composite manufacturing needs. Nevertheless attributes related to the measurement content and sensor positioning still remain and will be discussed in this section.

Perhaps the most significant attribute of a sensor is the information it produces. For the objectives discussed in the introduction, at least two transitions have to be made from what is actually measured; the first transition is from the measured quantity to a material property (e.g. a thermocouple is actually measuring a voltage difference which is used to infer the material temperature). The second transition is from the material property to another material property or a process property (e.g. the temperature of the material can be used to infer the stage of the curing process). The initially measured quantity (e.g. voltage in case of thermocouples) defines the sensitivity and accuracy of the inferred properties; it is therefore significant to investigate ways to improve the initial measurement qualitatively. However such a topic falls under the area of sensor development and will not be examined in the current study. On the other hand, material properties (electromagnetic, mechanical, optical, thermodynamic) and process properties (flow front, degree of cure, defects) will be briefly referred to, in order to know what to expect ultimately from each sensing technique (Table 2/rows 1–5).

As discussed in section 3.1, the needs for through-life and non-invasive monitoring of composite structures, have directed attention around the areas of smart and self-sensing composites respectively. Indicatively, optical fibers are of the most promising sensing method that can contribute to smart composites. But not the only; resistance measurements of the carbon reinforcement (both in or post production) is another example. The same method can of course be categorized as self-sensing since the reinforcement is part of the material. Alternatively, light propagation within common glass fibers can be used to derive intensity modulation or even spectra, both of which have been proven to monitor cure. The attributes ‘smart’ and ‘self-sensing’ (Table 2/rows 6 and 7) inform the reader of the potential of each sensor towards these two directions.

The position of the sensor with respect to the MUT (Table 2/row 8) is of great importance for two reasons: It defines the invasiveness and the reusability;

*Composites that exploit some of the involved materials as sensing elements.

**Composites with multiple functions that are enabled by the constitutive materials.

Table 2. Typical implementation attributes of contemporary *in-line* FRP monitoring techniques

	DEA	**Out-of-plane DC**	**In-plane DC**	**ETDR**	**OFI**	**Ultrasonic transducer**
Material property	Complex dielectric permittivity	Electrical resistance		Real permittivity, magnetic permeability	Strain, temperature	Micro-mechanical impedance
Flow Front	✓	✓	✓	✓	✓	✓
Curing degree	✓	✓	✓	✓	✓	✓
Void content	✓					✓
Delaminations	✓					✓
Smart			✓		✓	
Self-Sensing			✓	✓		
Position relative to the MUT	Contact/ Embedded	Contact/ Embedded	Embedded	Contact/ Embedded	Embedded	Contact
Spatial allocation	3-D point/ 3-D areal	point	point/lineal/areal	3-D lineal/ 3-D areal	point	3-D point
Post manufacturing usage	–	–	SHM	SHM	SHM	NDE
Industrial Applicability	✓	✓				✓
Practical limitations	Require electrical isolation from carbon fibers		Only for glass fiber reinforcements, laborious installation		Fragility, laborious installation	Requires high fixation pressure

	OFR	**Spectrometer**	**Thermo-couple**	**IR thermo- graphy**	**Pressure transducer**
Material property	Refractive index	Absorption/ emission spectra	Temperature	Superficial temperature	Pressure
Flow Front	✓	✓	✓		✓
Curing degree	✓	✓	✓	✓	
Void content					
Delaminations				✓	
Smart					✓
Self-Sensing		✓			
Position relative to the MUT	Embedded	Embedded	Contact/ Embedded	Remote	Contact
Spatial allocation	point/lineal	point	point	areal	point
Post manufacturing usage	–	–	–	NDE	–
Industrial Applicability			✓	✓	✓
Practical limitations	Fragility, laborious installation	A through beam window required (remote spectrometers), fragility (OFS), laborious installation	–	Requires open or transparent moulding, high parasitic content	–

if the sensor is material embedded it can have a negative structural effect on the composite and it is considered disposable as in most cases extracting it from the part is impossible. Solutions that only require contact are only invasive to the reactor (e.g. mould) and not to the material, thus exhibit higher reusability. Remote methods are of course non-invasive to either material or reactor and since they do not suffer from contact friction effects or cleaning-induced damages, are even more reusable. It must be noted, however, that remote methods usually require optical contact with the MUT therefore their usage is limited to open or transparent mould processes.

The spatial allocation of the measurement (Table 2/ row 9) is to give a feeling to the reader of the geometry of the space that is actually being measured with each system. When this is a localized planar space (e.g. in case of one sided access systems it is the plane defined by the exciting and sensing elements), the measurement is characterized as point measurement. When the space is expanded (not localized) on the same plane in a line or area, the measurement can be distinguished correspondingly to lineal meas-

urement or areal measurement. Measurements that include information from out-of-plane space (e.g. DEA) will be referred to as 3-dimentional (3-D). Some methods offer various possibilities in that regard. For instance, when the electrodes of an in-plane DC system are placed perpendicularly to each other (SMARTweaveTM), point measurements are taken from the cross-linking locations. When the electrodes are parallel with a small or large distance between them, lineal or areal measurements are produced respectively.

Post-manufacturing and *in-line* testing are overlapping territories. The potential of post manufacturing usage of an *in-line* sensing technique (Table 2/row 10) is mainly addressing the areas of Non-Destructive Evaluation (NDE) [80] and Structural Health Monitoring (SHM) [81]. Such potential is intriguing in that a single system would cover a larger portion of the life-span of a composite part. Perhaps the most controversial example in that context are the OFIs that can monitor the strains applied on a part both in-production and in-service. The drawback in this case is the lack of reliable assessment of the effect of the embedded optical fibers on the structural health of the part. It must be noted that this drawback does not apply to all methods with post-manufacturing potential (e.g. Ultrasonics are not material embedded which is why non-destructive ultrasonic testing is an industrially standardized process).

Typically, all sensing methods can be used in a laboratory but mostly the ones that are not material intrusive are attracted to industry. Indeed, the existing protocol of standardized industrial processes excludes anything that compromises the structural integrity of a part (e.g. a material embedded sensor) while a second argument against them is the intensive labor and high costs involved in embedding. As a result, material embedded solutions find only laboratory applications; the current trend in industrial moulds are sensors that require only superficial contact with the material. The extreme mould conditions have triggered the development of a new generation of sensor probes appropriate for mounting in moulds; their shells protect from the common mould temperatures and pressures. The probes are connected to remote measuring units that contain the less tolerant components of the measuring system (e.g. electronics and circuitry). Commercial probes of the kind can be found for thermocouples, pressure transducers, DEA, DC, Ultrasonic or even Spectroscopy. IR thermography can also be used industrially but is limited to visible operations. The potential of industrial usage is given by (Table 2/row 11).

Each sensing approach has limitations of different nature, depending on the principle of operation. Focusing more on practical operational restrictions, one can comment for example that sensors monitoring electrical properties (DEA, DC etc.) either cannot be used with carbon (conductive) fibers, or that they need additional isolation from them. Optical fiber-based methods (OFI, OFR, OFS) need laborious installation within the composite specimen while they are highly fragile which means that the probability of sensor destruction is higher than usual and needs to be taken into account for both cost and efficiency reasons. Another example is the high fixation pressure required by ultrasonic transducers in order to achieve acoustic coupling. Given that during conversion the pressure of the probe on the material varies (e.g. due to material shrinkage), a screw fixation is not enough; alternative means of fixation pressure (e.g. spring) must be used. The major known practical limitations of each method are briefly referred to in (Table 2/row 12).

4. Conclusions

The latest advances on *in-line* monitoring of FRP composites were summarized in the current review. The theoretical grounds of optical fiber, electrical or sound wave-based technologies were discussed, with respect to their interpretation to electromagnetic, mechanical, optical or thermodynamic material properties. Selected publications of the last fourteen years in composites *in-line* sensing depict the interest in smart, self-sensing and multifunctional composite structures. An evaluation with respect to practical implementation aspects summarizes the overall abilities and drawbacks of each system within an actual setup.

Nomenclature

ε^* Complex dielectric permittivity
ε' Real dielectric permittivity
ε'' Dielectric loss
ε_i'' Ionic component of the dielectric loss
ε_0 Air replacement permittivity
Λ Grating spacing
λ_B Bragg wavelength
μ Magnetic permeability

η Fluid viscosity
ρ Ion resistivity or ion viscosity
ξ Thermo-optic coefficient
ω Angular frequency
A Wave amplitude
a Attenuation coefficient
a_e Thermal expansion coefficient
c_l Longitudinal wave velocity
c_s Shear wave velocity
d Density
Z_d Discontinuity electrical impedance
E Young's modulus
E_i Electromagnetic voltage pulse
E_d Electromagnetic reflection waveform
e Electron charge
G Shear modulus
K Geometric constant of the transmission line
M Molar mass
N Concentration of ionic species
n Refractive index
n_0 Core refractive index
p_e Photo-elastic constant
R_M Molar refractivity
R_e Electric reflection coefficient
R_o Optical reflection coefficient
r Average radius of ionic species
s Axial strain
T Temperature
T_g Glass transition temperature
υ Poisson's ratio
υ Poisson's ratio
Z Average number of electric charges of ionic species

Acknowledgements

The authors kindly acknowledge the financial support provided by the Bundesministerium für Wirtschaft, Familie und Jugend.

References

[1] Huntson D.: Assessment of the state-of-the-art for process monitoring sensors for polymer composites. U.S. Department of Commerce, National Institute of Standards and Technology, Materials Science and Engineering Laboratory, Washington (1991).

[2] Mulligan D. R.: Cure monitoring for composites and adhesives. Rapra, Shawbury (2003).

[3] Summerscales J.: In-process monitoring for control of closed-mold techniques for the manufacture of thermosetting matrix composites. in 'Advanced polymeric materials'. (eds.: Shonaike G. O., Advani S. G.) CRC Press, Boca Raton, 55–97 (2003).

[4] Fonseca G. E., Dubé M. A., Penlidis A.: A critical overview of sensors for monitoring polymerizations. Macromolecular Reaction Engineering, **3**, 327–373 (2009).
DOI: 10.1002/mren.200900024

[5] Webster J. G.: The measurement, instrumentation, and sensors handbook. CRC Press, Boca Raton (1999).

[6] Fraden J.: Handbook of modern sensors. AIP Press/Springer, New York (2004).

[7] Chanda M., Roy S. K.: Plastics technology handbook. CRC Press, Boca Raton (2007).

[8] Vassilikou-Dova A., Kalogeras I. M.: Dielectric analysis (DEA). in 'Thermal analysis of polymers, fundamentals and applications'. (eds.: Menczel J. D., Prime R. B.) Wiley, Hoboken, 497–613 (2009).
DOI: 10.1002/9780470423837.ch6

[9] Lee D. G., Kim H. G.: Non-isothermal *in situ* dielectric cure monitoring for thermosetting matrix composites. Journal of Composite Materials, **38**, 977–993 (2004).
DOI: 10.1177/0021998304040563

[10] Hegg M. C., Ogale A., Mescher A., Mamishev A., Minaie B.: Remote monitoring of resin transfer molding processes by distributed dielectric sensors. Journal of Composite Materials, **39**, 1519–1539 (2005).
DOI: 10.1177/0021998305051083

[11] Yenilmez B., Murat Sozer E.: A grid of dielectric sensors to monitor mold filling and resin cure in resin transfer molding. Composites Part A: Applied Science and Manufacturing, **40**, 476–489 (2009).
DOI: 10.1016/j.compositesa.2009.01.014

[12] Kim S. S., Murayama H., Kageyama K., Uzawa K., Kanai M.: Study on the curing process for carbon/epoxy composites to reduce thermal residual stress. Composites Part A: Applied Science and Manufacturing, **43**, 1197–1202 (2012).
DOI: 10.1016/j.compositesa.2012.02.023

[13] Kobayashi S., Matsuzaki R., Todoroki A.: Multipoint cure monitoring of CFRP laminates using a flexible matrix sensor. Composites Science and Technology, **69**, 378–384 (2009).
DOI: 10.1016/j.compscitech.2008.10.029

[14] Blythe A. R., Bloor D.: Electrical properties of polymers. Cambridge University Press, Cambridge, New York (2005).

[15] Lawrence J. M., Hsiao K-T., Don R. C., Simacek P., Estrada G., Sozer E., Stadtfeld H. C., Advani S. G.: An approach to couple mold design and on-line control to manufacture complex composite parts by resin transfer molding. Composites Part A: Applied Science and Manufacturing, **33**, 981–990 (2002).
DOI: 10.1016/S1359-835X(02)00043-X

[16] Luthy T., Ermanni P.: Flow monitoring in liquid composite molding based on linear direct current sensing technique. Polymer Composites, **24**, 249–262 (2003).
DOI: 10.1002/pc.10026

[17] Danisman M., Tuncol G., Kaynar A., Sozer E. M.: Monitoring of resin flow in the resin transfer molding (RTM) process using point-voltage sensors. Composites Science and Technology, **67**, 367–379 (2007).
DOI: 10.1016/j.compscitech.2006.09.011

[18] Garschke C., Weimer C., Parlevliet P. P., Fox B. L.: Out-of-autoclave cure cycle study of a resin film infusion process using *in situ* process monitoring. Composites Part A: Applied Science and Manufacturing, **43**, 935–944 (2012).
DOI: 10.1016/j.compositesa.2012.01.003

[19] Hsiao K-T.: Embedded single carbon fibre to sense the thermomechanical behavior of an epoxy during the cure process. Composites Part A: Applied Science and Manufacturing, **46**, 117–121 (2013).
DOI: 10.1016/j.compositesa.2012.11.007

[20] Robinson D. A., Jones S. B., Wraith J. M., Or D., Friedman S. P.: A review of advances in dielectric and electrical conductivity measurement in soils using time domain reflectometry. Vadose Zone Journal, **2**, 444–475 (2003).
DOI: 10.2136/vzj2003.4440

[21] Agilent Technologies: Time domain reflectometry theory. Application note (2014).

[22] Pandey G., Deffor H., Thostenson E. T., Heider D.: Smart tooling with integrated time domain reflectometry sensing line for non-invasive flow and cure monitoring during composites manufacturing. Composites Part A: Applied Science and Manufacturing, **47**, 102–108 (2013).
DOI: 10.1016/j.compositesa.2012.11.017

[23] Dominauskas A., Heider D., Gillespie J. W.: Electric time-domain reflectometry sensor for online flow sensing in liquid composite molding processing. Composites Part A: Applied Science and Manufacturing, **34**, 67–74 (2003).
DOI: 10.1016/S1359-835X(02)00232-4

[24] Dominauskas A., Heider D., Gillespie J. W.: Electric time-domain reflectometry distributed flow sensor. Composites Part A: Applied Science and Manufacturing, **38**, 138–146 (2007).
DOI: 10.1016/j.compositesa.2006.01.019

[25] Urabe K., Okabe T., Tsuda H.: Monitoring of resin flow and cure with an electromagnetic wave transmission line using carbon fiber as conductive elements. Composites Science and Technology, **62**, 791–797 (2002).
DOI: 10.1016/S0266-3538(02)00047-7

[26] Błażejewski W., Gąsior P., Kaleta J.: Application of optical fibre sensors to measuring the mechanical properties of composite materials and structures. in 'Advances in composite materials – Ecodesign and analysis'. (ed.: Attaf B.) InTech, Rijeka, 221–246 (2011).
DOI: 10.5772/13954

[27] Lee B. H., Kim Y. H., Park K. S., Eom J. B., Kim M. J., Rho B. S., Choi H. Y.: Interferometric fiber optic sensors. Sensors, **12**, 2467–2486 (2012).
DOI: 10.3390/s120302467

[28] Kuang K. S. C., Zhiang L., Cantwell W. J., Bennion I.: Process monitoring of aluminum-foam sandwich structures based on thermoplastic fibre–metal laminates using fibre Bragg gratings. Composites Science and Technology, **65**, 669–676 (2005).
DOI: 10.1016/j.compscitech.2004.09.005

[29] Jung K., Kang T. J.: Cure monitoring and internal strain measurement of 3-d hybrid braided composites using fiber bragg grating sensor. Journal of Composite Materials, **41**, 1499–1519 (2007).
DOI: 10.1177/0021998306068088

[30] Khoun L., de Oliveira R. D., Michaud V., Hubert P.: Investigation of process-induced strains development by fibre Bragg grating sensors in resin transfer moulded composites. Composites Part A: Applied Science and Manufacturing, **42**, 274–282 (2011).
DOI: 10.1016/j.compositesa.2010.11.013

[31] Archer E., Broderick J., McIlhagger A. T.: Internal strain measurement and cure monitoring of 3D angle interlock woven carbon fibre composites. Composites Part B: Engineering, **56**, 424–430 (2014).
DOI: 10.1016/j.compositesb.2013.08.067

[32] Tsai L., Cheng T-C., Lin C-L., Chiang C-C., Meyendorf N. G., Peters K. J., Ecke W.: Application of the embedded optical fiber Bragg grating sensors in curing monitoring of Gr/epoxy laminated composites. in 'Proceeding of the 16th International Symposium on: Smart Structures and Materials and Nondestructive Evaluation and Health Monitoring, San Diego, USA' Vol 7293, 7–8 (2009).
DOI: 10.1117/12.817520

[33] Nakamura K.: Ultrasonic transducers. Woodhead Publishing, Cambridge (2012).

[34] Lempriere B. M.: Ultrasound and elastic waves. Academic Press, Amsterdam (2002).

[35] Fomitchov P. A., Kim Y. K., Kromine A. K., Krishnaswamy S.: Laser ultrasonic array system for real-time cure monitoring of polymer-matrix composites. Journal of Composite Materials, **36**, 1889–1901 (2002).
DOI: 10.1177/0021998302036015245

[36] Schmachtenberg E., Schulte zur Heide J., Töpker J.: Application of ultrasonics for the process control of resin transfer moulding (RTM). Polymer Testing, **24**, 330–338 (2005).
DOI: 10.1016/j.polymertesting.2004.11.002

[37] Visvanathan K., Balasubramaniam K.: Ultrasonic torsional guided wave sensor for flow front monitoring inside molds. Review of Scientific Instruments, **78**, 015110/1–015110/8 (2007).
DOI: 10.1063/1.2432258

[38] Pavlopoulou S., Soutis C., Staszewski W. J.: Cure monitoring through time–frequency analysis of guided ultrasonic waves. Plastics, Rubber and Composites, **41**, 180–186 (2012).
DOI: 10.1179/1743289811Y.0000000052

[39] Liebers N., Raddatz F., Schadow F.: Effective and flexible ultrasound sensors for cure monitoring for industrial composite production. in 'Proceedings of Deutscher Luft- und Raumfahrtkongress (DGLR). Berlin, Germany', 281405/1–281405/6 (2012).
[40] Yu F., Yin S.: Fiber optic sensors. Marcel Dekker (2002).
[41] Sharma K. K.: Optics: Principles and applications. Academic Press, Amsterdam (2006).
[42] Wang P., Molimard J., Drapier S., Vautrin A., Minni J. C.: Monitoring the resin infusion manufacturing process under industrial environment using distributed sensors. Journal of Composite Materials, **46**, 691–706 (2012).
DOI: 10.1177/0021998311410479
[43] Lekakou C., Cook S., Deng Y., Ang T. W., Reed G. T.: Optical fibre sensor for monitoring flow and resin curing in composites manufacturing. Composites Part A: Applied Science and Manufacturing, **37**, 934–938 (2006).
DOI: 10.1016/j.compositesa.2005.03.003
[44] Li C., Cao M., Wang R., Wang Z., Qiao Y., Wan L., Tian Q., Liu H., Zhang D., Liang T., Tang C.: Fiber-optic composite cure sensor: monitoring the curing process of composite material based on intensity modulation. Composites Science and Technology, **63**, 1749–1758 (2003).
DOI: 10.1016/S0266-3538(03)00118-0
[45] Gupta N., Sundaram R.: Fiber optic sensors for monitoring flow in vacuum enhanced resin infusion technology (VERITy) process. Composites Part A: Applied Science and Manufacturing, **40**, 1065–1070 (2009).
DOI: 10.1016/j.compositesa.2009.04.022
[46] Buggy S. J., Chehura E., James S. W., Tatam R. P.: Optical fibre grating refractometers for resin cure monitoring. Journal of Optics A: Pure and Applied Optics, **9**, S60–S65 (2007).
DOI: 10.1088/1464-4258/9/6/S09
[47] Fawcett A. H.: Polymer spectroscopy. Wiley, Chichester (1996).
[48] Wang L., Pandita S., Machavaram V. R., Malik S., Harris D., Fernando G. F.: Characterisation of the cross-linking process in an E-glass fibre/epoxy composite using evanescent wave spectroscopy. Composites Science and Technology, **69**, 2069–2074 (2009).
DOI: 10.1016/j.compscitech.2008.11.001
[49] Mahendran R. S., Wang L., Machavaram V. R., Pandita S. D., Chen R., Kukureka S. N., Fernando G. F.: Fiber-optic sensor design for chemical process and environmental monitoring. Optics and Lasers in Engineering, **47**, 1069–1076 (2009).
DOI: 10.1016/j.optlaseng.2009.05.013
[50] Dunkers J. P., Lenhart J. L., Kueh S. R., van Zanten J. H., Advani S. G., Parnas R. S.: Fiber optic flow and cure sensing for liquid composite molding. Optics and Lasers in Engineering, **35**, 91–104 (2001).
DOI: 10.1016/S0143-8166(00)00110-X
[51] Wood K. H., Brown T. L., Wu M. C., Gause C. B.: Fiber optic sensors for cure/health monitoring of composite materials. NASA Langley Research Center, Hampton (2004).
[52] Anne M. L., Le Gal La Salle E., Bureau B., Tristant J., Brochot F., Boussard-Plédel C., Ma H. L., Zhang X. H., Adam J. L.: Polymerisation of an industrial resin monitored by infrared fiber evanescent wave spectroscopy. Sensors and Actuators B: Chemical, **137**, 687–691 (2009).
DOI: 10.1016/j.snb.2009.01.069
[53] Cruz J. C., Osswald T. A.: Monitoring epoxy and unsaturated polyester reactions under pressure – Reaction rates and mechanical properties. Polymer Engineering and Science, **49**, 2099–2108 (2009).
DOI: 10.1002/pen.21448
[54] Childs P. R. N: Practical temperature measurement. Butterworth-Heinemann, Oxford (2001).
[55] Hsiao K-T., Little R., Restrepo O., Minaie B.: A study of direct cure kinetics characterization during liquid composite molding. Composites Part A: Applied Science and Manufacturing, **37**, 925–933 (2006).
DOI: 10.1016/j.compositesa.2005.01.019
[56] Tuncol G., Danisman M., Kaynar A., Sozer E. M.: Constraints on monitoring resin flow in the resin transfer molding (RTM) process by using thermocouple sensors. Composites Part A: Applied Science and Manufacturing, **38**, 1363–1386 (2007).
DOI: 10.1016/j.compositesa.2006.10.009
[57] Marin E., Robert L., Triollet S., Ouerdane Y.: Liquid resin infusion process monitoring with superimposed fibre Bragg grating sensor. Polymer Testing, **31**, 1045–1052 (2012).
DOI: 10.1016/j.polymertesting.2012.07.018
[58] Yoon H-J., Costantini D. M., Limberger H. G., Salathé R. P., Kim C-G., Michaud V.: *In situ* strain and temperature monitoring of adaptive composite materials. Journal of Intelligent Material Systems and Structures, **17**, 1059–1067 (2006).
DOI: 10.1177/1045389X06064889
[59] Cuevas E., Garcia C., Hernandez S., Venegas P., Gomez T., Canada M.: Non destructive testing for non-cured composites: Air coupled ultrasounds and thermography. in 'Proceedings of the 5th International Symposium on NDT in Aerospace, Singapore' p.13 (2013).
[60] Di Fratta C., Klunker F., Ermanni P.: A methodology for flow-front estimation in LCM processes based on pressure sensors. Composites Part A: Applied Science and Manufacturing, **47**, 1–11 (2013).
DOI: 10.1016/j.compositesa.2012.11.008
[61] Govignon Q., Bickerton S., Kelly P. A.: Experimental investigation into the post-filling stage of the resin infusion process. Journal of Composite Materials, **47**, 1479–1492 (2013).
DOI: 10.1177/0021998312448500

[62] Xin C., Gu Y., Li M., Li Y., Zhang Z.: Online monitoring and analysis of resin pressure inside composite laminate during zero-bleeding autoclave process. Polymer Composites, **32**, 314–323 (2011). DOI: 10.1002/pc.21048

[63] Simacek P., Eksik Ö., Heider D., Gillespie J. W., Advani S.: Experimental validation of post-filling flow in vacuum assisted resin transfer molding processes. Composites Part A: Applied Science and Manufacturing, **43**, 370–380 (2012). DOI: 10.1016/j.compositesa.2011.10.002

[64] Kobayashi S., Tanaka A., Morimoto T.: Analytical prediction of resin impregnation behavior during processing of unidirectional fiber reinforced thermoplastic composites considering pressure fluctuation. Advanced Composite Materials, **21**, 425–432 (2012). DOI: 10.1080/09243046.2012.740773

[65] Elhajjar R.: Smart composites – Mechanics and design. CRC Press, Boca Raton (2013).

[66] Zwaag S.: Self-healing materials: An alternative approach to 20 centuries of materials science. Springer Science+Business Media B.V., Dordrecht (2008).

[67] Angelidis N., Wei C. Y., Irving P. E.: The electrical resistance response of continuous carbon fibre composite laminates to mechanical strain. Composites Part A: Applied Science and Manufacturing, **35**, 1135–1147 (2004). DOI: 10.1016/j.compositesa.2004.03.020

[68] Shen L., Li J., Liaw B. M., Delale F., Chung J. H.: Modeling and analysis of the electrical resistance measurement of carbon fiber polymer–matrix composites. Composites Science and Technology, **67**, 2513–2520 (2007). DOI: 10.1016/j.compscitech.2006.12.020

[69] Todoroki A., Omagari K., Shimamura Y., Kobayashi H.: Matrix crack detection of CFRP using electrical resistance change with integrated surface probes. Composites Science and Technology, **66**, 1539–1545 (2006). DOI: 10.1016/j.compscitech.2005.11.029

[70] Bakhshi M., Horoschenkoff A.: Use of carbon fiber sensors to determine the resin flow. in 'Proceedings of the 19th ICCM Conference. Montreal, Canada', 7606–7613 (2013).

[71] Obaid A. A., Yarlagadda S., Yoon M. K., Hager N. E., Domszy R. C.: A time-domain reflectometry method for automated measurement of crack propagation in composites during mode I DCB testing. Journal of Composite Materials, **40**, 2047–2066 (2006). DOI: 10.1177/0021998306061309

[72] Pandey G., Wolters M., Thostenson E. T., Heider D.: Localized functionally modified glass fibers with carbon nanotube networks for crack sensing in composites using time domain reflectometry. Carbon, **50**, 3816–3825 (2012). DOI: 10.1016/j.carbon.2012.04.008

[73] Todoroki A., Kurokawa H., Mizutani Y., Matsuzaki R., Yasuoka T.: Self-sensing time domain reflectometry method for damage monitoring of a CFRP plate using a narrow-strip transmission line. Composites Part B: Engineering, **58**, 59–65 (2014). DOI: 10.1016/j.compositesb.2013.10.047

[74] Qin F. X., Peng H. X.: Macro-composites containing ferromagnetic microwires for structural health monitoring. Nano Communication Networks, **1**, 126–130 (2010). DOI: 10.1016/j.nancom.2010.08.001

[75] Phan M. H., Peng H. X., Yu S. C., Wisnom M. R.: Large enhancement of GMI effect in polymer composites containing *co*-based ferromagnetic microwires. Journal of Magnetism and Magnetic Materials, **316**, 253–256 (2007). DOI: 10.1016/j.jmmm.2007.02.112

[76] Qin F. X., Brosseau C., Peng H. X., Wang H., Sun J.: *In situ* microwave characterization of microwire composites with external magnetic field. Applied Physics Letters, **100**, 192903/1–192903/4 (2012). DOI: 10.1063/1.4712126

[77] Rau M., Iftemie A., Baltag O., Costandache D.: The study of the electromagnetic shielding properties of a textile material with amorphous microwire. Advances in Electrical and Computer Engineering, **11**, 17–22 (2011). DOI: 10.4316/AECE.2011.01003

[78] Qin F., Peng H-X.: Ferromagnetic microwires enabled multifunctional composite materials. Progress in Materials Science, **58**, 183–259 (2013). DOI: 10.1016/j.pmatsci.2012.06.001

[79] Leng J., Du S.: Shape-memory polymers and multifunctional composites. CRC Press, Boca Raton (2010).

[80] Karbhari V. M.: Non-destructive evaluation (NDE) of polymer matrix composites. Woodhead, Cambridge (2013).

[81] Cai J., Qiu L., Yuan S., Shi L., Liu P., Liang D., Shi L.: Structural health monitoring for composite materials. in 'Composites and their applications' (ed.: Hu N.) Intech, Rijeka (2012). DOI: 10.5772/48215

eXPRESS Polymer Letters Vol.8, No.11 (2014) 841–849
Available online at www.expresspolymlett.com
DOI: 10.3144/expresspolymlett.2014.85

Preparation of carboxymethyl cellulose based microgels for cell encapsulation

Y. Ke[1], *G. S. Liu*[2], *J. H. Wang*[3], *W. Xue*[1], *C. Du*[4], *G. Wu*[4*]

[1]Department of Biomedical Engineering, College of Life Science and Technology, Jinan University, 510632 Guangzhou, China
[2]Department of Pediatrics, Institute of Fetal-Preterm Labor Medicine, The First Affiliated Hospital, Jinan University, 510632 Guangzhou, China
[3]National Engineering Research Center for Tissue Reconstruction and Restoration, 510006 Guangzhou, China
[4]Biomaterial Research Institute, School of Materials Science and Engineering, South China University of Technology, 510641 Guangzhou, China

Received 8 April 2014; accepted in revised form 13 June 2014

Abstract. Biocompatible and biodegradable carboxymethyl cellulose (CMC) has been modified with 4-hydroxybenzylamine (CMC-Ph) in order to prepare CMC-based microgels through the horseradish peroxidise/hydrogen peroxide enzymatic reaction. CMC-Ph was identified as a blend, and the amount of the grafted 4-hydroxybenzylamine per 100 units of CMC was between 17 and 23 according to the molecular weight of CMC. Through a special designed co-flowing microfluidic device, CMC-Ph microgels were prepared with the radius from 100 to 500 μm *via* adjusting the flow rates of the disperse phase and the continuous phase, respectively. The chondrocytic cell line ATDC5 was encapsulated in the CMC-Ph microgels. The cell-laden microgels were cultured for up to 40 days, illustrating the biocompatibility of CMC-Ph and the microfluidic approach through the enzymatic crosslinking reaction primarily. CMC-Ph showed a great promise to encapsulate the cells for further fabrication of the injectable scaffolds.

Keywords: *biocompatible polymers, polymer synthesis, polymer gels, carboxymethyl cellulose, microfluidic*

1. Introduction

Osteoarthritis, characterized by progressively degeneration or loss of articular cartilage, is the most common form of arthritis. Tissue engineering has shown great promise as a strategy to develop biological substitutes to restore, replace or regenerate the defective tissue [1]. Scaffolds made of polymeric biomaterials offer support for cell attachment, proliferation and differentiation [2, 3]. Encapsulation of living cells within a semi-permeable membrane is a simple one-step procedure with characteristics of homogenous cell distribution and excellent cell viability [4, 5]. Its unique self-assembled capability makes it suitable for injectable scaffolds for *in situ* tissue regeneration. Recent advances in microfluid designs have brought the field of microfluidics to the forefront of the preparation of micro- or nano-gels for cell encapsulation [6–8].

Many naturally derived biomaterials have been used for encapsulation, such as sodium alginate [9] and agarose [10]. However, these biomaterials have limited ability to support cell attachment, growth and differentiation, resulting in low cell viability and growth [11]. Carboxymethyl cellulose (CMC) is a water-soluble, biodegradable and biocompatible derivative of cellulose. Its hydrophilic carboxylic or hydroxyl groups serve as active sites for preparing CMC gels. Physical-crosslinking CMC gels *via*

*Corresponding author, e-mail: imwugang@scut.edu.cn

supermolecular [12] and ionic [13] interaction are simple to be produced, but usually questioned by their reversibility.

Chemical-crosslinking provides CMC gels a more stable three-dimensional network. For example, divinyl sulfone [14], epichlorohydrin [15], aldehydes [16, 17], fumaric acid [18] and citric acid [19] have been used as crosslinkers to form CMC and CMC composite gels. Monomers with double bond, such as *N*-isopropyl acrylamide [20] and partially neutralized acrylic acid/rectorite [21], have been initiated by ammonium persulfate and coupled onto CMC backbones *via* methylene bisacrylamide (crosslinker). These chemical crosslinkers are limited for the applications in biomedical or pharmaceutical areas because of their toxicity or the stimulatory reaction to the encapsulated bioactive molecules or live cells. A bio-based carbodiimide crosslinker has been used to prepare chitosan/CMC microgels [22], indicating a very low efficiency of crosslinking reaction. Another synthetic route is to form CMC gels *via* functional groups of both components without any crosslinker, for example, hydrazide-functionalized CMC/aldehyde-functionalized dextran, suggested by Kesselman *et al*. [23]. They have introduced the two reactive streams into a continuous oil solution simultaneously through two separate inlets of a microfluidics device. However, the premixing of the reactive streams before the formation of droplets often resulted in the blockage of small opening of the microfluidics.

Enzymatic reaction has been extensively studied owing to its low toxicity, mild reaction, stereochemistry, and high reaction velocity, high enantio-, regio- and chemo-selectivity [24]. Horseradish peroxidise/hydrogen peroxide (HRP/H_2O_2) is a common enzymatic system, where peroxidases (oxidoreductases) catalyzes the oxidation of donors using H_2O_2, resulting in polyphenols linked at the aromatic ring by C–C and C–O coupling of phenols [25]. DeVolder *et al.* [26] have prepared hydrogels of alginate grafted with pyrrole groups through a HRP-activated crosslinking reaction for drug release system. We designed a special microfluidic device to prepare monodisperse CMC-based microdroplets [27]. In this work, we synthesized 4-hydroxybenzylamine modified CMC (CMC-Ph) with different molecular weight and prepared CMC-Ph microgels through an enzymatic reaction. The properties of CMC-Ph that influenced the formation of microgels were studied. Moreover, cells were encapsulated in CMC-Ph microgels to study the biocompatibility of CMC-Ph and the microfluidic approach through the enzymatic crosslinking reaction.

2. Experimental

2.1. Materials

1-Ethyl-3-(3-dimethylaminopropyl)carbodiimide hydrochloride (EDC), *N*-hydroxysulfosuccinimide (NHS), HRP (250 units/mg), lecithin, 4-hydroxybenzylamine, 1-hydroxybenzotriazole hydrate (HOBT) and 2-(4-morpholino)ethanesulfonic acid (MES) were obtained from Qiyun Biotech (China). Aqueous H_2O_2 (30%, w/w) and liquid paraffin were purchased from Dalu Chemical Reagent (China). All reagents were of analytical grade and used as received.

CMC with M_w of 1.0×10^5 (CMC_{10}), 2.0×10^5 (CMC_{20}) and 3.0×10^5 (CMC_{30}) were purchased from Jingchun Chemical Reagent (China). CMC-Ph was synthesized according to our previous study [27]: Briefly, CMC and 4-hydroxybenzylamine were dissolved in MES buffer (50 mM, pH 6.0) at 1.0 and 0.6%, respectively. NHS, HOBt and EDC were added at a weight ratio of 1:0.26:0.68:0.70 (CMC:NHS:HOBt:EDC). The solution was magnetic stirred for 24 hours and dialyzed against deionized water using an ultrafiltration membrane (molecular weight cut-off = 3500 Da) at 25°C for 4 days. The resultant polymer solution was enriched by a rotary evaporator (100 rpm) at 50°C and lyophilized.

2.2. Preparation of CMC-Ph microgels

A co-flowing microfluidic device with an inner diameter of 260 μm and an outer diameter of 510 μm was used for preparing CMC-Ph microparticles. The continuous liquid paraffin phase was prepared as follows: In brief, 250 mL of liquid paraffin containing 1.25 mL H_2O_2 was magnetically stirred for 12 hours at 25°C and centrifuged at 2000 rpm for 10 minutes. Lecithin was dissolved at 3.0% (w/v) into the upper liquid paraffin containing H_2O_2. CMC-Ph aqueous solution containing HRP as the dispersed phase was injected into the microfluidic device using a micro-syringe pump (Baoding Longer TS-1B/W0109-1B, China), and the continuous phase was injected into an inlet in a perpendicular direction. The particles flew along the channel and finally collected.

2.3. Preparation of cell-laden CMC-Ph microgels

The lyophilized CMC-Ph was sterilized by exposure to epoxyethane vapor. CMC-Ph (~0.2 g) was dissolved in 4 mL of Dulbecco's modified Eagle medium (DMEM, Hyclone, USA). HRP was then dissolved at 1 mg/mL in DMEM, and the solution was kept at 37°C. The chondrocytic cell line ATDC5 (Sigma, USA) of sixth passage was trypsinized at a density of 1×10^7 cells/mL. 1 mL of cell suspension was added into the CMC-Ph solution containing HRP, which injected as the dispersed phase at a rate of 50 μL/min. The continuous liquid paraffin phase was injected at a rate of 10 mL/min. The resulted microgels were collected and centrifuged at 2000 rpm for 5 min. Phosphate buffer saline (PBS, pH = 7.4, Gibco, USA) was added to the tube, followed by centrifuging at 2000 rpm for 5 min twice. The collected cell-laden CMC-Ph microgels were removed into 6-well cell culture dishes (Corning, USA). Cells enclosed in microgels were incubated in DMEM supplemented with 10% (v/v) fetal bovine serum (FBS, Gibco, USA) in a humidified atmosphere at 37°C under 5% CO_2. The medium was exchanged for fresh medium every 2 days, and a new cell culture dish was replaced every 4 days till cell-culturing for 40 days. The morphology of the cell-laden CMC-Ph microgels was evaluated under an inverted light microscope (Nikon ECLIPSE TS100, Japan).

2.4. Characterization

A Bruker (Germany) Vertex 70 Fourier transform infrared spectrometry (FTIR) was used to obtain infrared analyses of 4-hydroxybenzylamine, CMC and CMC-Ph using KBr pellet method. The spectra comprised 64 scans at a resolution of 1 cm^{-1} in 4000~400 cm^{-1} spectral range.

^1H nuclear magnetic resonance (NMR, Drx-400 Bruker, Germany) spectra were achieved at 400 MHz using deuterated water (D_2O) as solvent in the presence of tetramethylsilane as an internal standard.

Graft density of phenols in CMC-Ph was calculated by measuring the absorbance at 275 nm of CMC-Ph solutions using a Thermo (USA) Evolution 300 UV-VIS spectrometer. The absorbance being measured was compared with a 4-hydroxybenzylamine standard curve. The graft density of phenols then calculated from the ratio of phenols to 100 repeat units of CMC. The data was the mean of five samples.

Molecular weight and polydispersity index (PDI) of CMC and CMC-Ph were determined by a Water (USA) 515–410 gel permeation chromatography (GPC). Weight-average (M_w) and number-average (M_n) molecular weight were expressed with respect to polyethyleneglycol standards.

Rheological behavior of CMC-Ph solutions with different concentrations was measured using a TA (USA) ARES/RFS rotational viscometer at 16 and 30°C, respectively. The solutions were prepared by mass using a XS105DU balance (Mettler Toledo, Switzerland) with a precision of 10^{-5} g. The employed shear rate varied from 0.01 to 250 s^{-1}, and viscosity and stress were identified.

Stereomicroscope images of the microdroplets in the liquid paraffin were obtained with a SMZ-DM200 stereomicroscope (Optec, China) with a digital CCD camera to estimate the size in number-average diameters and coefficients of variation (CV, defined as the ratio of standard deviation to the mean) by analyzing images of 100 particles in liquid paraffin phase.

3. Results and discussion

3.1. CMC-Ph

3.1.1. FTIR spectrum

In Figure 1a, the absorption bands at 1450, 1501, 1561 and 1611 cm^{-1} were ascribed to the benzene skeleton vibration. The peaks at 842, 1261 and 1386 cm^{-1} were attributed to the C–H out-of-plane bending vibration of benzene ring, C–O stretching vibration and O–H in-plane bending vibration of phenol, respectively. The absorption peak at 1642 cm^{-1} was associated to N–H scissoring vibration of free amine. The broad association peak at 3423 cm^{-1} would be the stretching vibration of C–H, O–H and N–H, in which a hydrogen bond formed between a hydrogen atom and O–H group or N–H group. In FTIR spectrum of CMC-Ph (Figure 1b, curve (2)), the absorption bands at 1045, 1323 and 1415 cm^{-1} were attributed to the –C=O stretching vibration, in-plane bending vibration of O–H and C–H scissoring vibration of methylene of CMC, respectively (Figure 1b, curve (1)). The characteristic absorption bands of 4-hydroxybenzylamine were traced, including the C–H out-of-plane bending vibration of benzene ring (827 cm^{-1}), C–O strong stretching vibration of phenol (1257 cm^{-1}), benzene skeleton vibration (1504 and 1456 cm^{-1}) and N–H scissoring vibration of free amine (1644 cm^{-1}). The

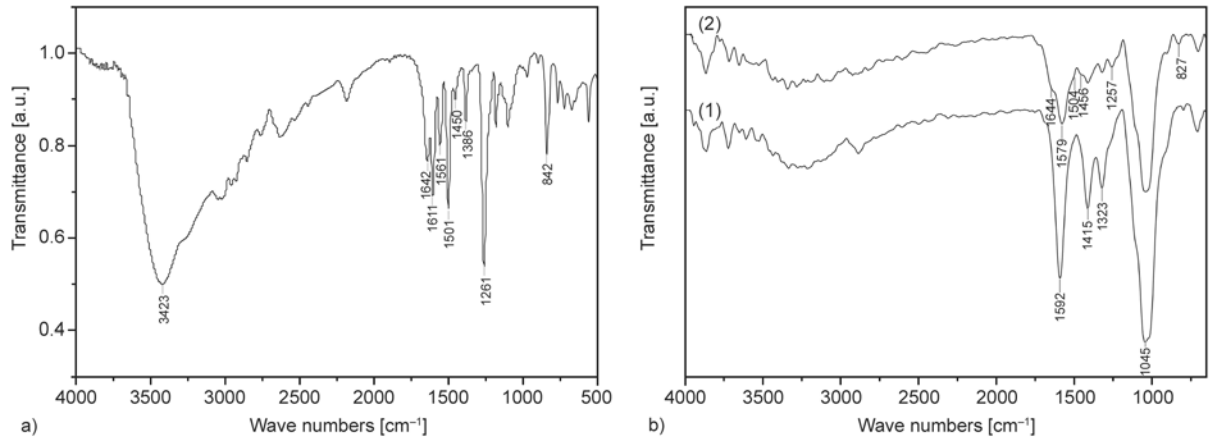

Figure 1. FTIR spectra of 4-hydroxybenzylamine (a), CMC (b-(1)) and CMC-Ph (b-(2))

band with a peak at 1579 cm^{-1} was the IR absorption of the –O– stretching vibration of CMC (1592 cm^{-1}, Figure 1b, curve (1)) and the benzene skeleton vibration (1561 and 1611 cm^{-1}).

3.1.2. ^{1}H NMR spectra

Figure 2 illustrates ^{1}H NMR spectra along with schematics of their chemical structures, on which proton assignments are indicated. 4-Hydroxybenzylamine (Figure 2a) showed chemical shifts (δ) at 6.60 and 7.06 ppm of aromatic protons (a) and (b), respectively, and at 3.81 ppm of aliphatic protons (c). The spectra of CMC (Figure 2b) and CMC-Ph (Figure 2c) showed δ of anomeric protons at 4.15 and 4.42 ppm, and sugar ring protons between 3.11 and 3.99 ppm for both macromolecules [28]. The signals at 7.21 and 6.84 ppm of CMC-Ph spectrum were attributed to the aromatic protons of 4-hydroxybenzylamine being grafted with CMC (CMC-*g*-Ph, 1a and 1b). The strong inductive effect being caused by the neighboring carbonyl groups decreased the electron density of the benzene ring, so that δ of aromatic protons decreased compared with those of 4-hydroxybenzylamine (Figure 2a, (a) and (b)). The signals at 1.79~2.02 ppm (2a), 0.96~1.19 ppm (2b) and 2.75 ppm (2c) were ascribed to the byproduct being formed between CMC and EDC (CMC-EDC). EDC and phenolic groups of 4-hydroxybenzylamine reacted to form CMC-*g*-Ph-EDC, resulting in a change in proton shift of the aromatic protons at 7.51 and 7.35 ppm (3a and 3b) [29].

3.1.3. Graft density of phenols

The CMC-Ph aqueous solution showed a specific absorbance with a peak at 275 nm of 4-hydroxybenzylamine. We also tested the dialysis solution at four days, the UV absorption was not detected, so that the UV absorption of the CMC-Ph solution would be ascribed to the grafted 4-hydroxybenzylamine. Based on the standard curve, the amount of the grafted 4-hydroxybenzylamine per 100 units of CMC (grafting density) was calculated (Table 1). It fell in the range of 17~23, and increased as M_w of CMC increased. Usually, the flexibility of polymer increased with the increasing molecular weight, so that CMC with higher M_w or M_n was favorable to collide effectively with small molecules *via* changing conformation, leading to a higher reaction probability of CMC with 4-hydroxybenzylamine.

3.1.4. Molecular weight

The molecular weight and the polydispersity (PI) of the molecular weight were also shown in Table 1. M_w, M_n and PI of CMC-Ph were higher than those of CMC. The difference of molecular weight between CMC and CMC-Ph increased as the molecular weight of CMC increased, perhaps owing to a slight cross-linking between hydroxyl groups of 4-hydroxybenzylamine and carboxyl groups of CMC under EDC/NHS reactive system.

Table 1. Grafting density and molecular weight of CMC-Ph

	Grafting density	M_n ($\times10^{-4}$)	M_w ($\times10^{-4}$)	Polydispersity
CMC_{10}	0	4.47	9.86	2.2
CMC_{20}	0	6.20	24.53	4.0
CMC_{30}	0	10.20	31.52	3.1
CMC_{10}-Ph	17.4	4.44	17.43	3.9
CMC_{20}-Ph	17.8	9.42	48.08	5.1
CMC_{30}-Ph	22.5	17.36	87.50	5.0

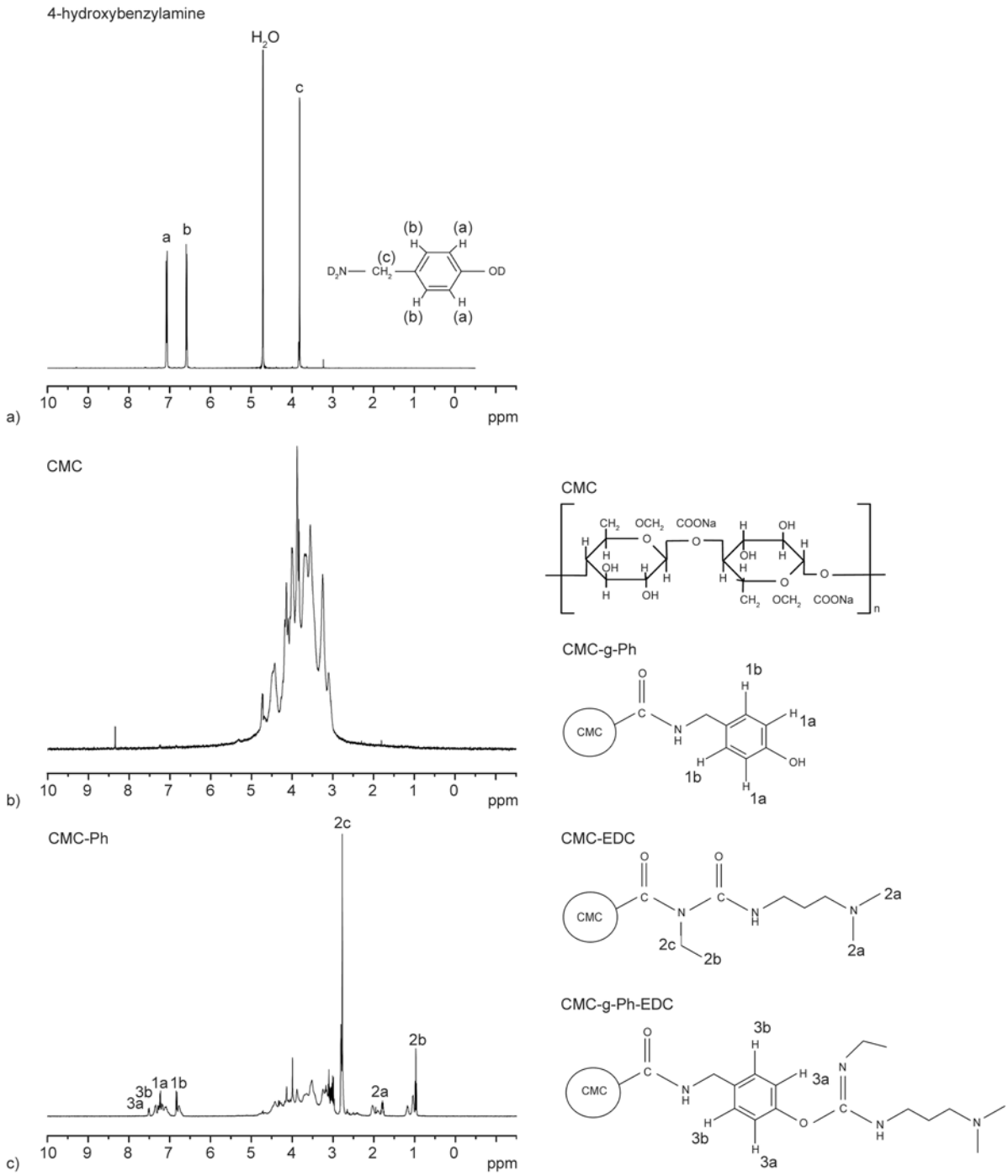

Figure 2. ^{1}H NMR spectra of 4-hydroxybenzylamine (a), CMC (b) and CMC-Ph (c) with protons assigned

3.1.5. Viscosity

Rheological behavior of the CMC-Ph solution with the different molecular weight has been determined by analyzing the influence of shear rate on viscosity. Flow curve was a straight line passing through the origin, and the stress increased lineally with the shear rate at 30°C, respectively (Figure 3 (a_2), (b_2), (c_2). An increase in the molecular weight produced an increase in the viscosity (Figure 3). For example, the viscosity was 5.4, 14.8 and 25.5 mPa·s, respectively for CMC_{10}-Ph, CMC_{20}-Ph and CMC_{30}-Ph at 30°C. As the molecular weight of CMC-Ph increased, the intermolecular volume decreased and thus the molecular interaction of CMC-Ph increased. The CMC-Ph with high molecular weight possessed low ability to rearrange and move past each other, so

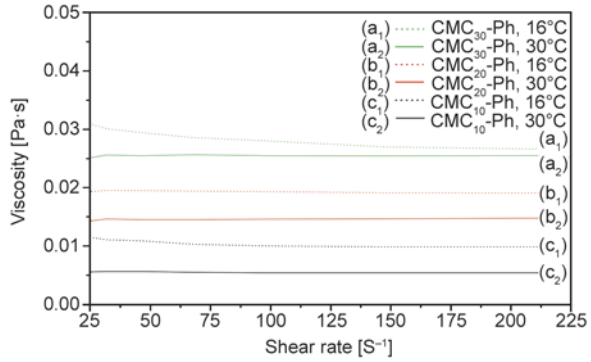

Figure 3. Viscosity of 1.0% CMC-Ph solution being measured at 16°C: (a_1) CMC_{30}-Ph; (b_1) CMC_{20}-Ph; (c_1) CMC_{10}-Ph, and at 30°C: (a_2) CMC_{30}-Ph; (b_2) CMC_{20}-Ph; (c_2) CMC_{10}-Ph

that the internal resistance to flow increased. Therefore, the viscosity increased with the increasing molecular weight of CMC-Ph.

At 16°C, the viscosity of CMC_{30}-Ph decreased significantly with the increasing shear rate. When the shear rate was 215 s^{-1}, the viscosity was 9.9, 19.1 and 26.6 mPa·s, respectively for CMC_{10}-Ph, CMC_{20}-Ph and CMC_{30}-Ph. In general, an increase in temperature allows quicker molecules motion and thus less energy is needed to flow CMC-Ph solution, resulting in a decrease in the viscosity. When the shear rate was 215 s^{-1}, the difference between viscosity measuring at 16 and 30°C was 4.45, 4.31 and 1.08 mPa·s for CMC_{10}-Ph, CMC_{20}-Ph and CMC_{30}-Ph, respectively. The less difference of CMC_{30}-Ph was perhaps owing to the decreasing viscosity as the shear rate increased. As the shear rate was 215 s^{-1}, the viscosity ratio of CMC_{30}-Ph to CMC_{10}-Ph at 16°C was 2.7, which reached 4.7 when temperature went up to 30°C.

3.2. CMC-Ph microgels

Prior to the microfluidic preparation of CMC-Ph microgels, we examined the gelation of the disperse fluid as the presence of H_2O_2. The CMC-Ph gels were formed after a contact time of 1 min. In the microfluidic device, the viscous disperse fluid was extruded into the immiscible continuous liquid flowing in the same direction. The disperse fluid flowed and snapped off at the orifice. H_2O_2 in the continuous liquid surrounded the CMC-Ph droplets containing HRP. Thereafter, diffusion of H_2O_2 from the continuous fluid to the disperse phase triggered the gelation reaction to bind the phenols groups.

Because H_2O_2 was separated from HRP, the enzymatic reaction cannot occur before the droplets formation, thus avoiding the blockage of the inner opening. The concentration of H_2O_2 in the continuous phase (0.82 mmol/L) would not bring severe harmful effect on the encapsulated contents, but it was enough for gelation of the microdroplets. The CMC-Ph microgels were intact while immersed in DMEM for 40 days. This diffusion-controlled crosslinking was very important for improving the integrity and encapsulation efficiency of microparticles.

We prepared the CMC-Ph microdroplets with different molecular weight while using the 1% CMC-Ph containing HRP (1 mg/mL). As the flow rate of the disperse phase (Q_d) was fixed at 10 μL/min, the effect of the flow rate of the continuous phase (Q_c) on the radius of microdroplets was shown in Figure 4a. The increased flow rate of the continuous phase produced a stronger shear force, thus resulted in a decreasing radius of the CMC-Ph microdroplets.

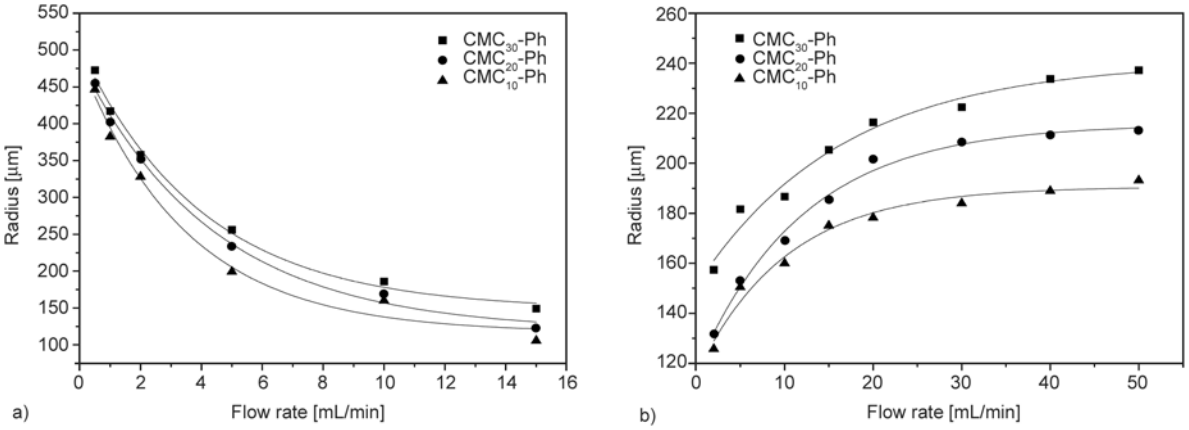

Figure 4. Dependence of flow rates on the size of the microdroplets obtained by using 1.0% CMC_{10}-Ph (triangle), CMC_{20}-Ph (circle) and CMC_{30}-Ph (square): (a) effect of Q_c on the radius of microdroplets at a constant Q_d (10 μL/min); (b) effect of Q_d on the radius of microdroplets at a fixed Q_c (10 mL/min)

When using a fixed Q_c (10 mL/min), the radius of the CMC-Ph microdroplets increased with an increasing flow rate of the disperse fluid (Figure 4b). In general, the CMC-Ph solution with higher molecular weight produced larger microdroplets due to higher viscosity.

3.3. Cell-laden CMC-Ph microgels

The injectable microsphere scaffolds should support cells adhesion, migration, and proliferation, and more important, maintain the differentiated phenotype of the cells within the scaffold. The cell-laden microgels would facilitate gas exchange, nutrient diffusion, and waste metabolism. ATDC5 is a prechondrogenic stem cell line, and reproduces the differentiation stages of chondrocytes during endochondral bone formation [30]. The ATDC5-laden microgels being cultured up to 40 days were shown in Figure 5. The microgels presented round morphology that was very important for mechanical stability under the compressive forces in the body. The living cells (light dots) were distributed separately in the microgels (Figure 5a). Some of the cell-laden microgels broke with the damaged border. The microgel did not maintain the round morphology any more (Figure 5b). Some of the cells released from the broken microgels and can stick to the cell culture dishes at 40 days of culturing (Figure 5c), showing high viability.

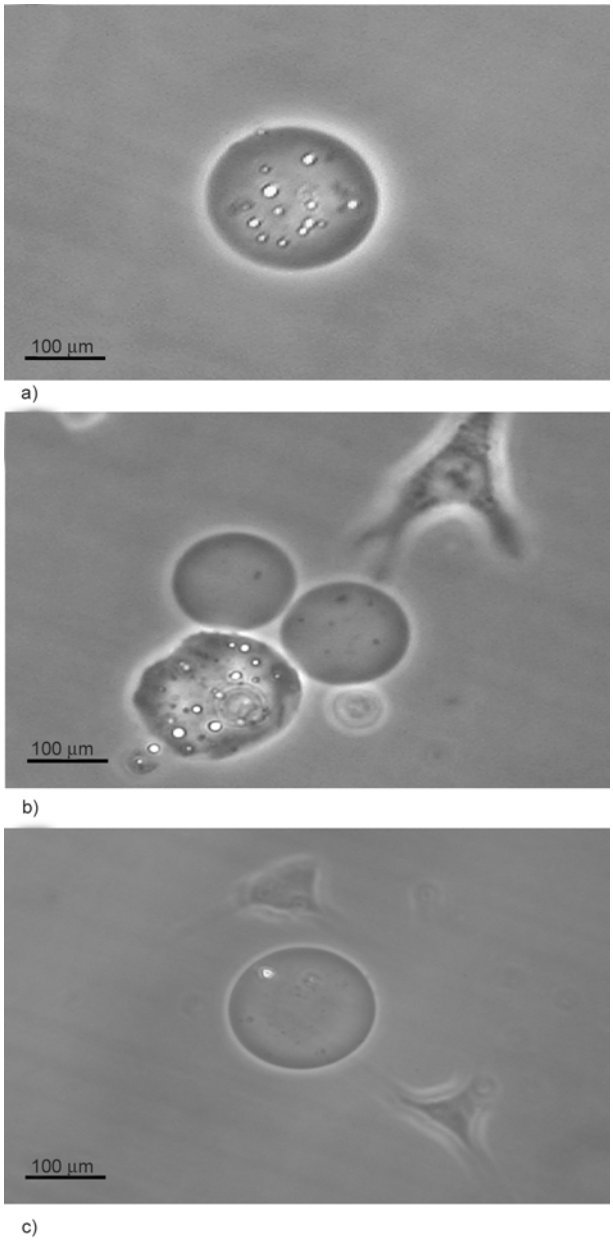

Figure 5. Photographs of the cell-laden microgels up to 40 days of culturing: (a) living cells distributed separately at 40 days; (b) broken cell-laden microgels at 5 days; (c) cells from the broken microgels sticking to the dishes at 40 days

4. Conclusions

4-Hydroxybenzylamine modified CMC with different molecular weight was synthesized through EDC/NHS coupling agents. Uniform CMC-Ph microparticles were obtained in the co-flowing microfluidic devices. The radius was tuned in the range of (100~500) μm by changing the flow rates of the disperse phase and the continuous phase, respectively. The cells encapsulated in CMC-Ph microgels were still living at 40 days of culturing. The microfluidic approach to the preparation of the cell-laden microgels will provide a potential method of fabricating scaffolds for tissue engineering, especially in the defect with an irregular-shape and/or a minimally invasive approach. The CMC-Ph microgels with the different molecular weight along with the different encapsulating content may also been used to prepare the injectable microsphere scaffolds, having a gradient mechanical property, a gradient encapsulating content, and a gradient releasing property.

Acknowledgements

This study was financially supported by the Basic Research Project of China (2012CB619105), the National Natural Science Foundation of China (51072056, 51173053), Guangdong Natural Science Foundation (9451063201003024), Guangdong Provincial Program for Excellent Talents in Universities, and Key Laboratory of Biomaterials of Guangdong Higher Education Institutes of Jinan University.

References

[1] Langer R., Vacanti J. P.: Tissue engineering. Science, **260**, 920–926 (1993).
DOI: 10.1126/science.8493529

[2] Hutmacher D. W.: Scaffolds in tissue engineering bone and cartilage. Biomaterials, **21**, 2529–2543 (2000).
DOI: 10.1016/S0142-9612(00)00121-6

[3] Ke Y., Wu G., Wang Y. J.: PHBV/PAM scaffolds with local oriented structure through UV polymerization for tissue engineering. BioMed Research International, **2014**, 157987/1–157987/9 (2014).
DOI: 10.1155/2014/157987

[4] Lanza R. P., Hayes J. L., Chick W. L.: Encapsulated cell technology. Nature Biotechnology, **14**, 1107–1111 (1996).
DOI: 10.1038/nbt0996-1107

[5] Orive G., Hernández R. M., Gascón A. R., Calafiore R., Chang T. M. S., De Vos P., Hortelano G., Hunkeler D., Lacík I., Shapiro A. M. J., Pedraz J. L.: Cell encapsulation: Promise and progress. Nature Medicine, **9**, 104–107 (2003).
DOI: 10.1038/nm0103-104

[6] Dendukuri D., Doyle P. S.: The synthesis and assembly of polymeric microparticles using microfluidics. Advanced Materials, **21**, 4071–4086 (2009).
DOI: 10.1002/adma.200803386

[7] Lazarus L. L., Riche C. T., Marin B. C., Gupta M., Malmstadt N., Brutchey R. L.: Two-phase microfluidic droplet flows of ionic liquids for the synthesis of gold and silver nanoparticles. ACS Applied Materials and Interfaces, **4**, 3077–3083 (2012).
DOI: 10.1021/am3004413

[8] Ke Y.: Microfluidic-assisted fabrication of nanoparticles for nanomedicine application. Recent Patents on Nanomedicine, **1**, 109–122 (2011).
DOI: 10.2174/1877912311101020109

[9] Sakai S., Kawakami K.: Both ionically and enzymatically crosslinkable alginate–tyramine conjugate as materials for cell encapsulation. Journal of Biomedical Materials Research Part A, **85**, 345–351 (2008).
DOI: 10.1002/jbm.a.31299

[10] Batorsky A., Liao J., Lund A. W., Plopper G. E., Stegemann J. P.: Encapsulation of adult human mesenchymal stem cells within collagen-agarose microenvironments. Biotechnology and Bioengineering, **92**, 492–500 (2005).
DOI: 10.1002/bit.20614

[11] Zimmermann H., Hillgärtner M., Manz B., Feilen P., Brunnenmeier F., Leinfelder U., Weber M., Cramer H., Schneider S., Hendrich C., Volke F., Zimmermann U.: Fabrication of homogeneously cross-linked, functional alginate microcapsules validated by NMR-, CLSM- and AFM-imaging. Biomaterials, **24**, 2083–2096 (2003).
DOI: 10.1016/S0142-9612(02)00639-7

[12] Liu H., Huang S., Li X., Zhang L., Tan Y., Wei C., Lv J.: Facile fabrication of novel polyhedral oligomeric silsesquioxane/carboxymethyl cellulose hybrid hydrogel based on supermolecular interactions. Materials Letters, **90**, 142–144 (2013).
DOI: 10.1016/j.matlet.2012.09.030

[13] Zhang H., Tumarkin E., Peerani R., Nie Z. H., Sullan R. M. A., Walker G. C., Kumacheva E.: Microfluidic production of biopolymer microcapsules with controlled morphology. Journal of the American Chemical Society, **128**, 12205–12210 (2006).
DOI: 10.1021/ja0635682

[14] Butun S., Ince F. G., Erdugan H., Sahiner N.: One-step fabrication of biocompatible carboxymethyl cellulose polymeric particles for drug delivery systems. Carbohydrate Polymers, **86**, 636–643 (2011).
DOI: 10.1016/j.carbpol.2011.05.001

[15] Chang C., He M., Zhou J., Zhang L.: Swelling behaviors of pH- and salt-responsive cellulose-based hydrogels. Macromolecules, **44**, 1642–1648 (2012).
DOI: 10.1021/ma102801f

[16] Rao K. M., Mallikarjuna B., Rao K. S. V. K., Prabhakar M. N., Rao K. C., Subha M. C. S.: Preparation and characterization of pH sensitive poly(vinyl alcohol)/sodium carboxymethyl cellulose IPN microspheres for in vitro release studies of an anti-cancer drug. Polymer Bulletin, **68**, 1905–1919 (2012).
DOI: 10.1007/s00289-011-0675-9

[17] Patenaude M., Hoare T.: Injectable, mixed natural-synthetic polymer hydrogels with modular properties. Biomacromolecules, **13**, 369–378 (2012).
DOI: 10.1021/bm2013982

[18] Akar E., Altınışık A., Seki Y.: Preparation of pH- and ionic-strength responsive biodegradable fumaric acid crosslinked carboxymethyl cellulose. Carbohydrate Polymers, **90**, 1634–1641 (2012).
DOI: 10.1016/j.carbpol.2012.07.043

[19] Gorgieva S., Kokol V.: Synthesis and application of new temperature-responsive hydrogels based on carboxymethyl and hydroxyethyl cellulose derivatives for the functional finishing of cotton knitwear. Carbohydrate Polymers, **85**, 664–673 (2011).
DOI: 10.1016/j.carbpol.2011.03.037

[20] Ekici S.: Intelligent poly(*N*-isopropylacrylamide)-carboxymethyl cellulose full interpenetrating polymeric networks for protein adsorption studies. Journal of Materials Science, **46**, 2843–2850 (2011).
DOI: 10.1007/s10853-010-5158-0

[21] Wang W. B., Wang A. Q.: Preparation, swelling, and stimuli-responsive characteristics of superabsorbent nanocomposites based on carboxymethyl cellulose and rectorite. Polymers for Advanced Technologies, **22**, 1602–1611 (2011).
DOI: 10.1002/pat.1647

[22] Dhar N., Akhlaghi S. P., Tam K. C.: Biodegradable and biocompatible polyampholyte microgels derived from chitosan, carboxymethyl cellulose and modified methyl cellulose. Carbohydrate Polymers, **87**, 101–109 (2012). DOI: 10.1016/j.carbpol.2011.07.022

[23] Kesselman L. R. B., Shinwary S., Selvaganapathy P. R., Hoare T.: Synthesis of monodisperse, covalently cross-linked, degradable 'smart' microgels using microfluidics. Small, **8**, 1092–1098 (2012). DOI: 10.1002/smll.201102113

[24] Kobayashi S., Uyama H., Kalra B.: Enzymatic polymerization. Chemical Reviews, **101**, 3793–3813 (2001). DOI: 10.1021/cr9901211

[25] Kurisawa M., Chung J. E., Yang Y. Y., Gao S. J., Uyama H.: Injectable biodegradable hydrogels composed of hyaluronic acid–tyramine conjugates for drug delivery and tissue engineering. Chemical Communications, **34**, 4312–4314 (2005). DOI: 10.1039/B506989K

[26] DeVolder R., Antoniadou E., Kong H. J.: Enzymatically cross-linked injectable alginate-g-pyrrole hydrogels for neovascularization. Journal of Controlled Release, **172**, 30–37 (2013). DOI: 10.1016/j.jconrel.2013.07.010

[27] Ke Y., Liu G. S., Guo T., Zhang Y., Li C., Xue W., Wu G., Wang J., Du C.: Size controlling of monodisperse carboxymethyl cellulose microparticles *via* a microfluidic process. Journal of Applied Polymer Science, **131**, 40663 (2014). DOI: 10.1002/app.40663

[28] Darr A., Calabro A.: Synthesis and characterization of tyramine-based hyaluronan hydrogels. Journal of Materials Science: Materials in Medicine, **20**, 33–44 (2009). DOI: 10.1007/s10856-008-3540-0

[29] Castillo J. J., Torres M. H., Molina D. R., Castillo-León J., Svendsen W. E., Escobar P., Martínez F.: Monitoring the functionalization of single-walled carbon nanotubes with chitosan and folic acid by two-dimensional diffusion-ordered NMR. Carbon, **50**, 2691–2697 (2012). DOI: 10.1016/j.carbon.2012.02.010

[30] Atkinson B. L., Fantle K. S., Benedict J. J., Huffer W. E., Gutierrez-Hartmann A.: Combination of osteoinductive bone proteins differentiates mesenchymal C3H/10T1/2 cells specifically to the cartilage lineage. Journal of Cellular Biochemistry, **65**, 325–339 (1997). DOI: 10.1002/(SICI)1097-4644(19970601)65:3<325::AID-JCB3>3.0.CO;2-U

eXPRESS Polymer Letters Vol.8, No.11 (2014) 850–861
Available online at www.expresspolymlett.com
DOI: 10.3144/expresspolymlett.2014.86

Synthesis of molecularly imprinted polypyrrole/titanium dioxide nanocomposites and its selective photocatalytic degradation of rhodamine B under visible light irradiation

M. Q. He, L. L. Bao, K. Y. Sun, D. X. Zhao, W. B. Li, J. X. Xia, H. M. Li*

School of Chemistry and Chemical Engineering, Jiangsu University, Zhenjiang, 212013 Jiangsu, China

Received 15 April 2014; accepted in revised form 13 June 2014

Abstract. Highly selective molecularly imprinted nanocomposites MIP_{RhB}-PPy/TiO_2 were successfully prepared by surface molecular imprinting technique with rhodamine B (RhB) as template molecule. The prepared MIP_{RhB}-PPy/TiO_2 coated with a thin imprinted layer could respond to visible light. The static and dynamic binding experiments revealed that MIP_{RhB}-PPy/TiO_2 possessed strong affinity, high adsorption capacity and fast adsorption rate for RhB. The selectivity experiments indicated that MIP_{RhB}-PPy/TiO_2 had excellent recognition selectivity for RhB. Selective photocatalytic degradation experiments indicated that the apparent rate constant (k) for the photodegradation of RhB over MIP_{RhB}-PPy/TiO_2 is 0.0158 min^{-1}, being 3.6 times of that over non-imprinted nanocomposites NIP-PPy/TiO_2 (0.0044 min^{-1}). Compared with the NIP-PPy/TiO_2, MIP_{RhB}-PPy/TiO_2 showed higher photocatalytic selectivity toward RhB under visible light, which was attributed the introduction of the imprinted cavities on the surface of MIP_{RhB}-PPy/TiO_2. Moreover, MIP_{RhB}-PPy/TiO_2 exhibited high reusability and stability. The results indicate that molecularly imprinted nanocomposites MIP_{RhB}-PPy/TiO_2 have a promising perspective in industrial wastewater treatment.

Keywords: *nanocomposites, photodegradation, selectivity, molecular imprinting, rhodamine B*

1. Introduction

Titanium dioxide (TiO_2) photocatalyst as a semiconductor material has been well studied for photocatalytic degradation of pollutants due to its inexpensive, non-toxic, good stability, excellent photoelectric properties and reusable performances [1–3]. However, it has a wide band gap (3.0–3.2 eV), and usually cannot be effectively activated by the solar light for degradation of pollution [4]. Much work have been tried to improve the photocatalytic efficiency of TiO_2 under visible light irradiation by transforming its optical response from the UV to the visible range, such as by metal doping [5, 6], nonmetal doping [7, 8], surface dye sensitization [9] and forming composites with other semiconductors [10, 11]. Recently, conductive polymers have emerged as stable photosensitizers to modify TiO_2 nanoparticles owning to their remarkable physical attributes and electrical properties [12]. Among various conductive polymers, polypyrrole (PPy) is one of the most promising conductive polymers due to its high absorption coefficients in the visible part of the spectrum, superior conductivity, electrochemical reversibility, high thermal stability and non-toxicity nature [13–17]. Some publications have been reported that PPy/TiO_2 nanocomposites showed higher adsorption capacity and better photocatalytic activity under visible light irradiation than that of neat TiO_2 nanoparticles [18–21].

Although the photocatalytic degradation activity of the modified photocatalyst is improved, the selective degradation of targeted pollutants is very poor

*Corresponding author, e-mail: hemq@ujs.edu.cn

as the reactivity of the hydroxyl radical is difficult to control. When applied to environmental treatment, photocatalysis may not be efficient if it aims to remove all pollutants by itself [22]. Therefore, it is important to find a way to selectively remove the targeted pollutants. In recent years several approaches have been proposed to enhance the selectivity of photocatalyst such as pH adjustment to control of surface electric charge [23], specific molecules modified surface of TiO_2 [24], double-region-structured photocatalysts [25], and using the molecular imprinting technique (MIT) for selective removal the organic pollutant [26]. Among these methods, MIT combined with photocatalytic technology exhibit higher efficient to enhance the selectivity of photocatalyst for degradation of targeted organic pollutants.

MIT is a promising way for synthesizing three-dimensional cross-linked polymers to achieve specific molecular recognition properties [27]. The molecularly imprinted polymers (MIPs), for its chemical/mechanical stability, high selectivity, low cost, and preparation simplicity, has been applied in many fields such as specific separation [28], solid-phase extraction [29], reactive catalysis [30], and sensors [31]. Compared with conventional MIPs, the surface imprinting polymers (SMIPs) which control the imprinted cavities to be situated at the surface or in the proximity of materials process more accessible sites, faster mass transfer, and higher adsorption capacity for template molecules. Based on the surface molecular imprinting technique (SMIT), Shen *et al*. [26] prepared a series of MIP-coated TiO_2 photocatalysts, the photodegradation experiments confirmed that the photocatalysts have good selectivity toward the two nitrophenols in both single and binary systems. Luo *et al*. [32] prepared inorganic-framework molecularly imprinted TiO_2/WO_3, The photocatalytic activity of molecularly imprinted TiO_2/WO_3 toward the target molecules is more than two times that of non-imprinted TiO_2/WO_3, a result of selective adsorption of target molecules on molecularly imprinted TiO_2/WO_3. Huo *et al*. [33] prepared the imprinted photocatalyst of poly-o-phenylenediamine (POPD) modified the TiO_2/fly-ash cenospheres, compared with the non imprinted photocatalysts, it could effectively select degradation of the targeted POPD in environment. The above approach, however, has some drawbacks such as a layer of organic polymer may hinder light absorption and could be degraded during photocatalysis. Therefore, it is crucial to obtain steady imprinted polymer and control the thickness of the imprinted layer.

In our study, a highly selective molecularly imprinted nanocomposite MIP_{RhB}-PPy/TiO_2 was successfully prepared by adopting the SMIT with TiO_2 as the support material, rhodamine B (RhB) as template molecule, respectively. The as-prepared MIP_{RhB}-PPy/TiO_2 coated with a thin layer of MIP not only exhibits high adsorption capacity and selectivity for RhB, but also can improve molecular recognitive photocatalytic activity under visible light irradiation. The adsorption characteristics of MIP_{RhB}-PPy/TiO_2 were explored using static and dynamic binding experiments, the adsorption selectivity of MIP_{RhB}-PPy/TiO_2 was also investigated. In addition, the selective photocatalytic degradation activity of MIP_{RhB}-PPy/TiO_2 towards RhB was discussed in detail.

2. Experimental

2.1. Reagents

All chemical reagents were used as received without further purification. TiO_2 nanoparticles (P25) were obtained from Degussa (Germany). Iron (III) chloride hexahydrate ($FeCl_3 \cdot 6H2O$) was obtained from Shanghai Meryer Chemical Reagent Co. (China), Ltd. Polypyrrole (PPy) was purchased from Lark Technology Co., Ltd. (UK), Rhodamine B (RhB) was obtained from Shanghai Sinopharm Chemical Co., Ltd. (China) Rhodamine 6G (Rh6G) was purchased from Shanghai Maikun Chemical Co., Ltd. (China), Methylene Blue (MB) was provided by Beijing Chemical Reagent Co. (China) Hydrochloric acid and ammonia aqueous were purchased from Shanghai Zhongshi Chemistry Co., Ltd. (China).

2.2. Characterization

X-ray diffraction (XRD) measurements were performed on a Philips X′ pert MPD Pro X-ray diffractometer using Cu Kα radiation (λ = 1.5406 Å). Transmission electron microscope was recorded with a JEOL-IEM-200CX microscope. A UV-2450 Ultraviolet-visible Spectrophotometer (Shimadzu, Japan) was used to obtain the reflectance spectra of the photocatalysts over a range of 200–800 nm, using $BaSO_4$ as a reflectance reference. The specific surface area of MIP_{RhB}-PPy/TiO_2 and NIP-PPy/TiO_2

were determined by Brunauer-Emmett-Teller (BET) method.

The photocurrent experiments were measured in Na_2SO_4 aqueous (0.2 mol·L^{-1}) solution under the irradiation of 500 W Xenon lamp. A standard three-electrode configuration was used in the experiments. The indium-tin oxide (ITO) glass (1 cm×1 cm) coated with as-prepared samples (0.1 mg) was used as working electrodes, a Pt wire was used as the counter electrode, and a saturated Ag/AgCl electrode was used as the reference electrode. A CHI660B electrochemical workstation (Chen Hua Instruments, China) was photocurrent test systems.

2.3. Preparation of MIP_{RhB}-PPy/TiO_2 nanocomposites

The TiO_2 nanoparticles (2.0 g) were dispersed in hydrochloric acid (100 mL, pH = 2) in four-necked round bottomed flask and sonicated for 30 min. RhB (0.03 g, 0.06 mmol) and pyrrole (17.3 μL, 0.25 μmol) were dissolved in mixed solvent of methanol and water (1:1, v/v), and the mixture was stirred in dark for 30 min. Then the solution was injected into the previous four-necked round bottomed flask at 0°C with constant stirring. After that, hydrochloric acid (2 mL, pH = 2) containing $FeCl_3·6H_2O$ (0.45 g, 0.0017 mmol) was added dropwise to the above cooled mixture. The mixture was permitted to react at 0°C for 4 h with continuous stirring. The product particles were washed repeatedly with ammonia aqueous solution (pH = 8) to remove the targeted RhB and then washed with distilled water to remove remaining ammonia. Finally, molecularly imprinted polypyrrole titanium dioxide nanocomposites (MIP_{RhB}-PPy/TiO_2) were obtained by centrifugation and drying.

As a contrast, the non-imprinted nanocomposites (NIP-PPy/TiO_2) were prepared in the absence of the template and treated by using the same method.

2.4. Binding experiments in dark

2.4.1. Batch mode binding experiments

The adsorption kinetics behaviour of MIP_{RhB}-PPy/TiO_2 for RhB was firstly measured at room temperature. MIP_{RhB}-PPy/TiO_2 (10 mg) was added into RhB aqueous solutions (80 μmol/L) and then the mixture was agitated in a shaken bed. After an interval of time, the mixture was centrifuged, and the supernatant solution was collected, and diluted with water to a certain times. Finally, the concentration of RhB was determined by UV-vis spectrophotometer at the maximum absorption wavelength of RhB. The adsorption amount (Q) was calculated by Equation (1):

$$Q = \frac{(C_0 - C_t)V}{W} \tag{1}$$

where Q [μmol/g] is the adsorption amount of MIP_{RhB}-PPy/TiO_2 for RhB, W [g] is the weight of the MIP_{RhB}-PPy/TiO_2 nanocomposites, V [L] is the volume of solution, C_0 [μmol/L] is the initial concentration of RhB and C_t [μmol/L] is the concentration of RhB at the time of t.

For the determination of the static binding behavior of MIP_{RhB}-PPy/TiO_2 for RhB, numbers of RhB aqueous solutions with different concentrations were taken into centrifuge tubes. Then 10 mg of MIP_{RhB}-PPy/TiO_2 or NIP-PPy/TiO_2 was added into the above solutions, respectively. These mixtures were agitated on a shaken bed at room temperature and centrifuged after reaching binding equilibrium. The supernatant solution was collected and diluted with water to a certain times. Finally, the equilibrium concentrations of RhB in the supernatants were determined by UV-vis spectrophotometer. The adsorption amount (Q_e, μmol/g) was calculated by Equation (2):

$$Q_e = \frac{(C_0 - C_e)V}{W} \tag{2}$$

where W [g] is the weight of MIP_{RhB}-PPy/TiO_2 or NIP-PPy/TiO_2, V [L] is the volume of the solution, C_0 [μmol/L] and C_e [μmol/L] are the initial concentration and the equilibrium concentration of RhB, respectively.

The binding parameters of MIP_{RhB}-PPy/TiO_2 are mainly estimated by Scatchard analysis with the data of static adsorption experiment. Scatchard equation is described by Equation (3):

$$\frac{Q_e}{C_e} = \frac{(Q_{max} - Q_e)}{K_d} \tag{3}$$

where K_d [μmol/L] is the equilibrium dissociation constant, Q_{max} [μmol/g] is the apparent maximum adsorption amount, Q_e [μmol/g] is the equilibrium adsorption amount of MIP_{RhB}-PPy/TiO_2 for RhB, and C_e [μmol/L] is the equilibrium concentration of RhB.

2.4.2. Selectivity experiments

In order to examine the recognition selectivity of MIP_{RhB}-PPy/TiO_2 towards RhB, Rh6G and MB are selected as competitive substances. The size and structure of Rh6G are quite analogous to RhB. The chemical structure of MB and RhB has certain difference. The structures of RhB, Rh6G and MB were shown in Figure 1.

The equilibrium adsorption amount of MIP_{RhB}-PPy/TiO_2 and NIP-PPy/TiO_2 for RhB and the competition species were calculated as above. The distribution coefficients (K_D, L/g) for RhB, Rh6G and MB were calculated according to Equation (4):

$$K_D = \frac{Q_e}{C_e} \tag{4}$$

where Q_e [μmol/g] is the equilibrium adsorption amount, and C_e [μmol/L] is the equilibrium concentration.

The selectivity coefficients (α) of MIP_{RhB}-PPy/TiO_2 and NIP-PPy/TiO_2 for RhB relative to the competition species were obtained from Equation (5):

$$\alpha = \frac{K_{Di}}{K_{Dj}} \tag{5}$$

where i and j represent the template and competition species, respectively.

A relative selectivity coefficient (α') can be defined as Equation (6):

$$\alpha' = \frac{\alpha_{MIP}}{\alpha_{NIP}} \tag{6}$$

where α_{MIP} and α_{NIP} are selectivity coefficients of MIP_{RhB}-PPy/TiO_2 and NIP-PPy/TiO_2 for RhB relative to the competition species, respectively.

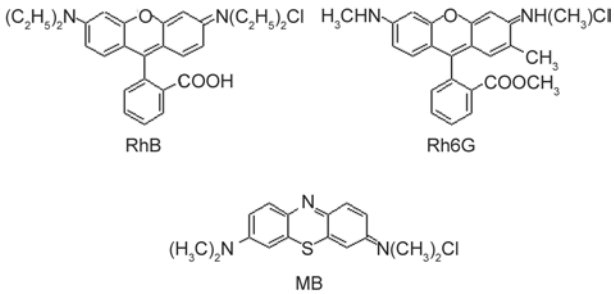

Figure 1. The structures of RhB, Rh6G and MB

2.5. Photocatalytic activity measurement

Photocatalytic activities of MIP_{RhB}-PPy/TiO_2 and NIP-PPy/TiO_2 nanocomposites were evaluated by photocatalytic degradation of RhB, Rh6G and MB aqueous solution under visible light irradiation, respectively. Experiments were carried out in a Pyrex photocatalytic reactor under 300 W Xe lamp with a 400 nm cutoff filter which was used as the visible light source. MIP_{RhB}-PPy/TiO_2 (0.1 g) or NIP-PPy/TiO_2 (0.1 g) nanocomposites were dispersed into RhB solution (100 mL, 10 mg·L^{-1}), respectively, then stirred in dark for 50 min to reach the adsorption-desorption equilibrium and the concentration of the RhB was determined as the initial concentration C_0. During irradiation, about 4.0 mL of the suspension continually was taken from the reaction cell every 20 min. The nanocomposites and the RhB solution were separated with acentrifuge. The RhB concentration was also analyzed through a UV-vis spectrophotometer. The degradation of Rh6G and MB aqueous solution were tested by using the same method.

3. Results and discussion

3.1. Preparing processes of MIP_{RhB}-PPy/TiO_2

The possible preparation protocol of MIP_{RhB}-PPy/TiO_2 nanocomposites is shown in Figure 2. It is of obvious importance that the functional monomers strongly interact with the template and form stable host-guest complexes prior to polymerization. From the structure of RhB shown in Figure 2, the epoxy group and a carboxyl group of RhB can interact with the secondary amines group of pyrrole via the hydrogen bonds to form a stable host-guest complex. The existence of such a complex leads to the formation of well-defined specific binding sites in imprinted layer of TiO_2. Subsequently, in situ polymerization occurs with the oxidizer of $FeCl_3 \cdot 6H_2O$, and PPy layer gradually grows on the surface of TiO_2 granules and extends to the interparticle space. Ultimately, the molecularly imprinted PPy/TiO_2 particles were washed by ammonia aqueous solution to remove RhB and leave imprinted cavities.

3.2. Charaterization of MIP_{RhB}-PPy/TiO_2

XRD patterns of the TiO_2 and MIP_{RhB}-PPy/TiO_2 photocatalysts are shown in Figure 3. In comparison with TiO_2, MIP_{RhB}-PPy/TiO_2 has no new diffraction peaks in the XRD pattern due to the amorphous imprinted layer. The average crystallite size of each sample is estimated by using the Scherrer formula, which is defined as Equation (7):

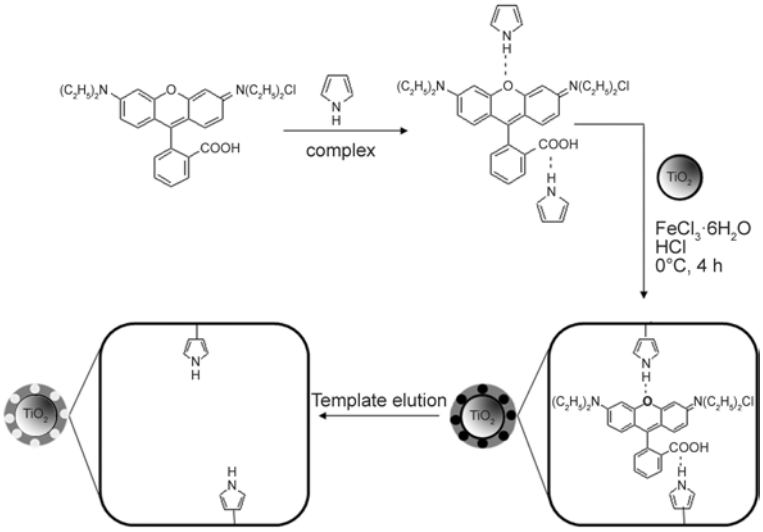

Figure 2. The preparation protocol of MIP_{RhB}-PPy/TiO_2

$$D_{\text{Scherrer}} = \frac{K\lambda}{\beta \cos\theta} \tag{7}$$

where K is the Scherrer constant ($K = 0.89$), λ is the wavelength of the X-ray radiation ($\lambda = 0.154056$ nm), β is the line width at half-maximum height of the most intense peak and θ is the diffraction angle.

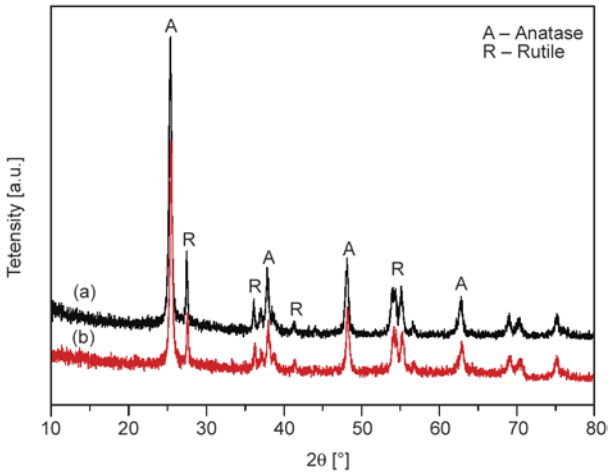

Figure 3. XRD patterns of: (a) TiO_2 and (b) MIP_{RhB}-PPy/TiO_2

The mean size of TiO_2 and MIP_{RhB}-PPy/TiO_2 photocatalysts can be estimated to be 19.70 and 21.05 nm, respectively. The result indicates that size of MIP_{RhB}-PPy/TiO_2 is a little bit larger than that of TiO_2. It can be attributed to the thin imprinted layer which coating on the surface of TiO_2.

The TEM images of TiO_2 and MIP_{RhB}-PPy/TiO_2 are given in Figure 4a and 4b, respectively. It can be confirmed that the morphology of MIP_{RhB}-PPy/TiO_2 does not differ much from that of TiO_2. The mean size of MIP_{RhB}-PPy/TiO_2 and TiO_2 are similar by comparing Figure 4a and 4b, which indicating that the imprinted layer is very thin. Figure 4a and 4b also reveals that TiO_2 are aggregated, and the MIP_{RhB}-PPy/TiO_2 alleviates the aggregation. The aggregation of TiO_2 could be attributed to high surface energy of the nanoparticles, and the repulsion force produced by the imprinted layer of the TiO_2 can

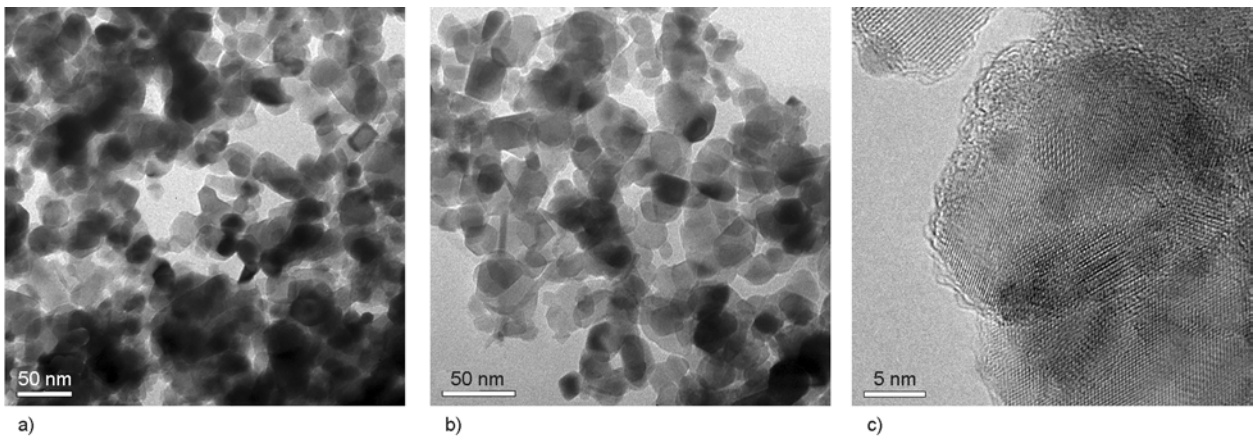

Figure 4. TEM images of: (a) TiO_2 and (b) (c) MIP_{RhB}-PPy/TiO_2

inhibit the aggregation of the MIP_{RhB}-PPy/TiO_2 nanocomposites. Figure 4c is the HR-TEM image of MIP_{RhB}-PPy/TiO_2. It shows the surface of MIP_{RhB}-PPy/TiO_2 nanocomposites is relatively rough, suggesting the formation of imprinting layer with a thickness of about 2 nm. The results are in good agreement with the XRD patterns.

The BET specific surface areas of MIP_{RhB}-PPy/TiO_2 and NIP-PPy/TiO_2 were measured as 60.1 and 55.3 m^2/g, respectively. The BET specific surface area of MIP_{RhB}-PPy/TiO_2 and NIP-PPy/TiO_2 is larger than that of TiO_2 (49.6 m^2/g). It indicated that the dispersion of MIP_{RhB}-PPy/TiO_2 is better than that of TiO_2. The BET specific surface area of MIP_{RhB}-PPy/TiO_2 is a little greater than that of NIP-PPy/TiO_2, it may be due to the initial molar ratio of PPy to TiO_2 which is 1:100. The amount of PPy is small, therefore, the imprinted cavities on the surface of MIP_{RhB}-PPy/TiO_2 play a tenuous role in improving the specific surface area.

3.3. Optical absorption properties

The optical properties of TiO_2, MIP_{RhB}-PPy/TiO_2 and NIP-PPy/TiO_2 were measured by UV-vis diffuse reflectance spectroscopy (DRS). Figure 5 shows the DRS of the TiO_2, MIP_{RhB}-PPy/TiO_2 and NIP-PPy/TiO_2. It can be seen that the absorption of MIP_{RhB}-PPy/TiO_2 and NIP-PPy/TiO_2 are much enhanced in the whole range of visible region compared with TiO_2. It is well known that the TiO_2 itself can not been excited by visible light. The possible explanation for this is that some synergic effect between PPy and TiO_2 which may induce efficiency of charge separation and PPy plays a role as photosensitizer in the nanocomposites. A classical Tauc method is employed to estimate the band gap enegy (E_g) of a semiconductor according to the Equation (8):

$$\alpha E_{photon} = K(E_{photon} - E_g)^{n/2} \quad (8)$$

where K is absorption constants for indirect transitions, α is the absorption coefficient, E_{photon} is the discrete photo-energy and E_g is the band gap energy. Among them, n depends on the characteristics of the transition in a semiconductor (direct transition $n = 1$ and indirect transition $n = 4$). For TiO_2, the value of n is 1.

The E_g of MIP_{RhB}-PPy/TiO_2 and NIP-PPy/TiO_2 are calculated to be 2.91, and 2.95 eV, respectively. They are less than that of TiO_2 (about 3.15 eV). The above results reveal that the absorption edges of MIP_{RhB}-PPy/TiO_2 lie in the visible region, so the nanocomposites can be excited to produce more electron-hole pairs under visible light irradiation, which could result in higher photocatalytic.

3.4. Photoelectrochemical properties

The transient photocurrent responses of TiO_2 and MIP_{RhB}-PPy/TiO_2 were recorded for several on-off cycles of visible light irradiation. As shown in Figure 6, the current responses on both the TiO_2 and MIP_{RhB}-PPy/TiO_2 in the dark are very low. When the irradiation was on, the electrons and holes were generated, therefore the current responses were drastically increased and the photocurrent came back to the original value as soon as the irradiation of light on the photoanode was stopped. In comparison with TiO_2, MIP_{RhB}-PPy/TiO_2 exhibited more intensive photocurrent responses, which indicated that MIP_{RhB}-PPy/TiO_2 can effectively reduce more the recombi-

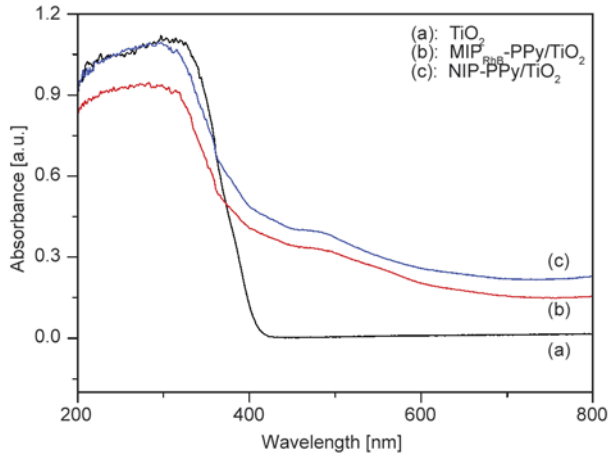

Figure 5. UV-vis diffuse reflectance spectra of TiO_2, MIP_{RhB}-PPy/TiO_2 and NIP-PPy/TiO_2

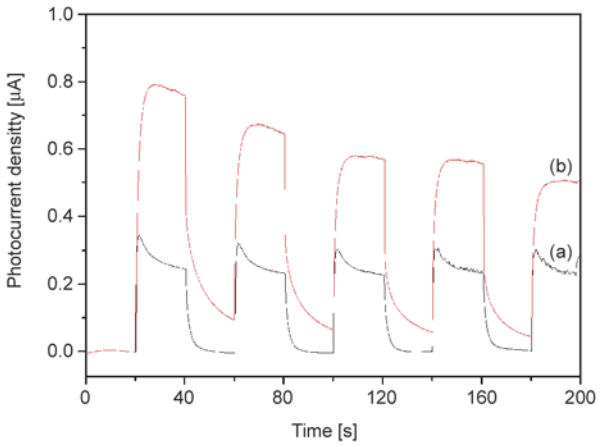

Figure 6. Transient photocurrent responses of: (a) TiO_2 and (b) MIP_{RhB}-PPy/TiO_2

nation of photogenerated electrons and holes, and produce longer living photogenerated carriers than that of TiO_2. Therefore, MIP_{RhB}-PPy/TiO_2 is expected to exhibit an improved photocatalytic activity for RhB degradation under visible light irradiation.

3.5. Adsorption properties of the nanocomposites

3.5.1. Adsorption kinetics

The adsorption kinetics curve of MIP_{RhB}-PPy/TiO_2 towards template RhB is provided in Figure 7. As seen in this figure, a fast initial adsorption of RhB by the MIP_{RhB}-PPy/TiO_2 was observed within the first 20 min, followed by a slow increase of the adsorption amount till the adsorption equilibrium. The equilibrium time is less than 50 min. It is reasonable to assume that the surface of MIP_{RhB}-PPy/TiO_2 has much imprinted cavities, the template RhB was easy to enter into the cavities and bind with the recognition sites. When the recognition sites were filled up, the rate of adsorption dropped significantly and adsorption process achieved equilibrium gradually.

In order to investigate the underlying mechanism of the adsorption process, the kinetic data obtained were analyzed using pseudo-first-order rate equation (Equation (9)) and pseudo-second-order rate equation (Equation (10)):

$$\log(Q_e - Q_t) = \log Q_e - \frac{k_1 t}{2.303} \tag{9}$$

$$\frac{1}{Q_t} = \frac{1}{k_2 Q_e^2} + \frac{t}{Q_e} \tag{10}$$

where Q_e [μmol/g] and Q_t [μmol/g] are the adsorption amount at equilibrium and time t [min], respectively, k_1 (min^{-1}) and k_2 (g/(μmol·min)) are pseudo-first-order and pseudo-second-order rate constants of adsorption, respectively.

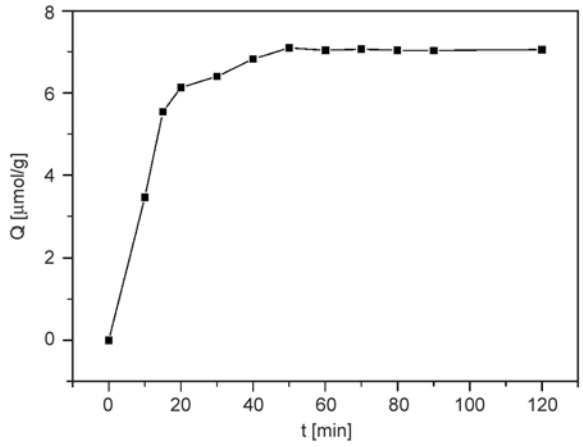

Figure 7. Adsorption kinetics curve of MIP_{RhB}-PPy/TiO_2 for RhB

Table 1. Adsorption kinetic constants for the pseudo-first-order rate equation and pseudo-second-order rate equation

Constants	Pseudo-first-order equation	Constants	Pseudo-second-order equation
$Q_{e,c}$ [μmol/g]	2.876	$Q_{e,c}$ [μmol/g]	7.537
Q_{exp} [μmol/g]	7.095	Q_{exp}]μmol/g]	7.095
k_1 [min^{-1}]	0.0456	k_2 [g/(μmol·min)]	0.0228
R^2	0.8107	R^2	0.9947

The adsorption kinetic constants for the pseudo-first-order rate equation and pseudo-second-order rate equation are listed in Table 1. As shown in Table 1, the correlation coefficient for the pseudo-second-order rate equation (R^2 = 0.9947) was higher than that of pseudo-first-order rate equation (R^2 = 0.8107). Moreover, the calculated equilibrium adsorption amount of MIP_{RhB}-PPy/TiO_2 is 7.537 μmol/g, which is consistent with the experimental data (7.095 μmol/g). Therefore, the adsorption behavior of MIP_{RhB}-PPy/TiO_2 for RhB belonged to the pseudo-second-order rate equation and the adsorption process was a chemical process.

3.5.2. Adsorption isotherms

The adsorption isotherms of MIP_{RhB}-PPy/TiO_2 and NIP-PPy/TiO_2 for RhB are illustrated in Figure 8a. As shown in this figure, the adsorption amount of the MIP_{RhB}-PPy/TiO_2 and NIP-PPy/TiO_2 increased gradually with the increase of concentration of RhB in the initial solution, and ultimately inclined to reach a stable value, the adsorption reached saturation. In addition, it also could be found that MIP_{RhB}-PPy/TiO_2 had much higher adsorption amount than that of NIP-PPy/TiO_2 at either low or high concentration. The above facts indicated that the non-selective physical adsorption occurred between NIP-PPy/TiO_2 and RhB. In contrast, the MIP_{RhB}-PPy/TiO_2 had generated specific recognition sites in imprinting cavities and exhibited higher adsorption capacity for RhB. Due to the adsorption capacity has much influence on the degradation behavior of organic pollutants, it is hoped that the MIP_{RhB}-PPy/TiO_2 show higher photocatalytic selectivity towards RhB than that of NIP-PPy/TiO_2.

In general, Scatchard analysis was used to evaluate the binding affinity and the theoretical binding site

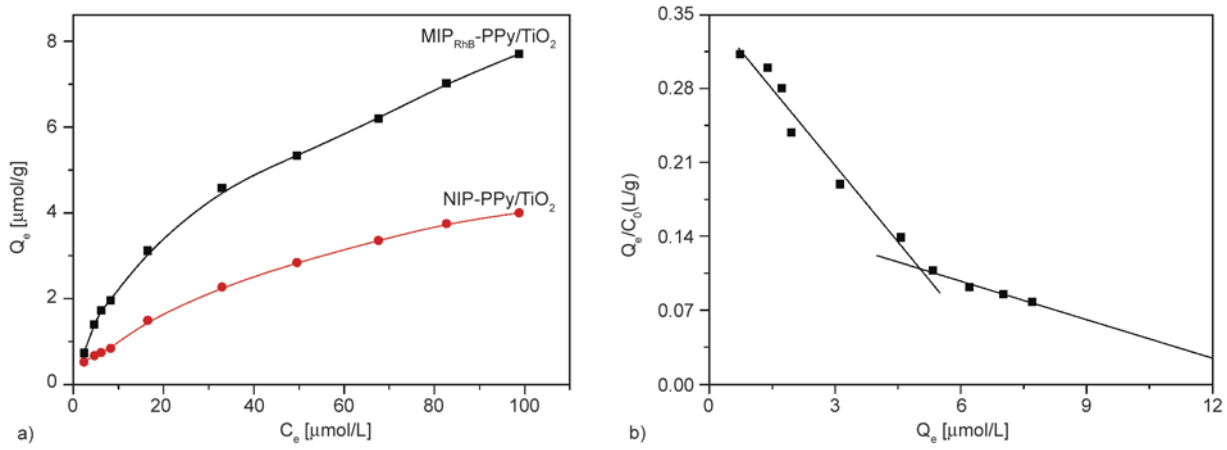

Figure 8. (a) Adsorption isotherms of MIP$_{RhB}$-PPy/TiO$_2$ and NIP-PPy/TiO$_2$ for RhB (b) Scatchard plot of the adsorption of MIP$_{RhB}$-PPy/TiO$_2$ for RhB

Table 2. The results of the Scatchard analysis

Binding site	Linear equation	K_d [μmol/L]	Q_{max} [μmol/g]	R^2
Higher affinity site	$Q_e/C_0 = -0.0482Q_e + 0.3517$	20.75	7.41	0.9490
Lower affinity site	$Q_e/C_0 = -0.0121Q_e + 0.1703$	82.64	14.07	0.9492

number for template of the molecularly imprinted material. Figure 8b shows the Scatchard plot of the adsorption of MIP$_{RhB}$-PPy/TiO$_2$ for RhB. As seen in this figure, there were two distinct linear sections in the plot. It suggests that there exist two types of binding sites in the imprinted layer in respect to the adsorption for RhB: one was of high selectivity or affinity with a high binding energy, and the other was of low affinity with a low binding energy. From the slopes and intercepts of the two straight lines, the K_d and Q_{max} values can be calculated, and the results are listed in Table 2.

3.5.3. Adsorption selectivity

Figure 9 shows the adsorption amount of MIP$_{RhB}$-PPy/TiO$_2$ and NIP-PPy/TiO$_2$ for RhB, Rh6G and MB, respectively. The distribution coefficient (K_D), selectivity coefficient of the sorbent (α) and the relative selectivity coefficient (α') values were summarized in Table 3. From Figure 9, the adsorption amount of MIP$_{RhB}$-PPy/TiO$_2$ for RhB is higher than that for Rh6G and MB. Compared with MB, the adsorption amount of MIP$_{RhB}$-PPy/TiO$_2$ for Rh6G is higher, whereas the adsorption amount of NIP-PPy/TiO$_2$ for the three substrates was almost the same. This indicated that the imprinted cavities have been created in MIP$_{RhB}$-PPy/TiO$_2$ owing to the addition of template RhB during polymerization, and the binding abilities of MIP$_{RhB}$-PPy/TiO$_2$ for RhB is far stronger than that for Rh6G and MB. From the data shown in Table 3, the selectivity coefficients of MIP$_{RhB}$-PPy/TiO$_2$ for RhB relative to Rh6G and MB are higher, 1.75 and 2.29, respectively. The selectiv-

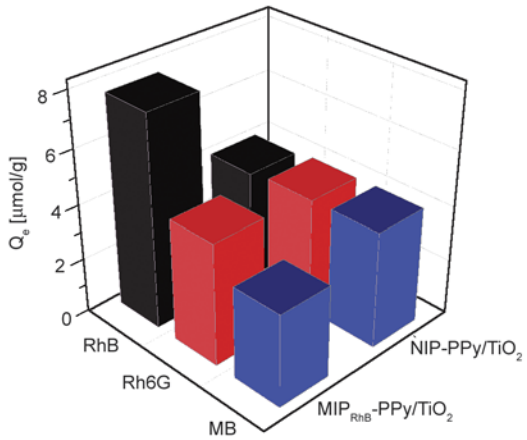

Figure 9. Adsorption amount of MIP$_{RhB}$-PPy/TiO$_2$ and NIP-PPy/TiO$_2$ for RhB, Rh6G and MB

Table 3 Distribution coefficient and selectivity coefficient data of MIP$_{RhB}$-PPy/TiO$_2$ and NIP-PPy/TiO$_2$

Photocatalyst	K_D [L/g]		α	α′	K_D [L/g]		α	α′
	RhB	Rh6G			RhB	MB		
MIP$_{RhB}$-PPy/TiO$_2$	0.096	0.055	1.75	1.82	0.096	0.042	2.29	2.44
NIP-PPy/TiO$_2$	0.050	0.052	0.96		0.050	0.053	0.94	

ity coefficients of NIP-PPy/TiO_2 for RhB relative to Rh6G and MB are lower, 0.96 and 0.94, respectively. This implies that the MIP_{RhB}-PPy/TiO_2 had higher adsorption selectivity for RhB over Rh6G and MB. The relative selectivity coefficients of MIP_{RhB}-PPy/TiO_2 for RhB relative to Rh6G and MB are 1.82 and 2.44, respectively, which are greater than 1 and showed the MIP_{RhB}-PPy/TiO_2 had higher adsorption selectivity than that of the NIP-PPy/TiO_2.

3.6. Photocatalytic activity

The photocatalytic activity of the MIP_{RhB}-PPy/TiO_2 and NIP-PPy/TiO_2 nanocomposites was measured by the degradation of RhB, Rh6G and MB aqueous solutions under visible light irradiation, respectively. As shown in Figure 10a, the MIP_{RhB}-PPy/TiO_2 photocatalysts exhibits the highest photocatalytic activity toward RhB. The degradation efficiency reaches 85% after 120 min irradiation being 2.1 times of that over NIP-PPy/TiO_2 (40%), meanwhile, the degradation efficiency of Rh6G and MB over MIP_{RhB}-PPy/TiO_2 are 63% and 59%, respectively. Figure 10b shows the time-dependent absorption spectra of RhB solution in the presence of MIP_{RhB}-PPy/TiO_2 microspheres. The maximum absorption of RhB suspension shifts from 553 to 522 nm. Meanwhile, it can be seen obviously that the color of the RhB solution changes gradually from fuchsia to colorless after irradiation for 120 min.

Figure 11 gives the kinetic data for the photodegradation of RhB, Rh6G and MB over different photocatalysts in the single systems, which clearly show that all the degradation processes follow a pseudo-first-order kinetics, which was defined as Equation (11):

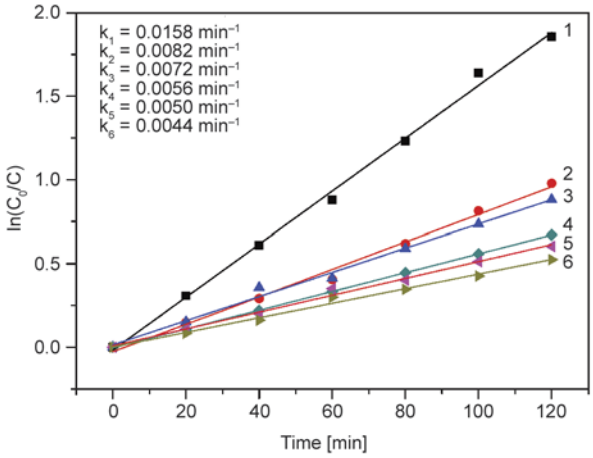

Figure 11. Kinetic datas for the degradation of RhB (1), Rh6G (2), MB (3) over MIP_{RhB}-PPy/TiO_2 and MB (4), Rh6G (5), RhB (6) over NIP-PPy/TiO_2

$$\ln\left(\frac{C_0}{C}\right) = kt \tag{11}$$

where C_0 [mg/L] and C [mg/L] are the concentration of RhB, Rh6G or MB at $t = 0$ [min] and instant t [min], respectively, and k [min^{-1}] is the apparent rate constant.

The values of the apparent rate constant (k) of the pseudo-first-order reaction are listed in Figure 11. As seen in this figure, the k value for the photodegradation of the targeted RhB over MIP_{RhB}-PPy/TiO_2 is 0.0158 min^{-1}, being 3.6 times of that over NIP-PPy/TiO_2 (0.0044 min^{-1}), meanwhile, the k values for the photodegradation of Rh6G and MB over MIP_{RhB}-PPy/TiO_2 are 0.0082 and 0.0072 min^{-1}, being only

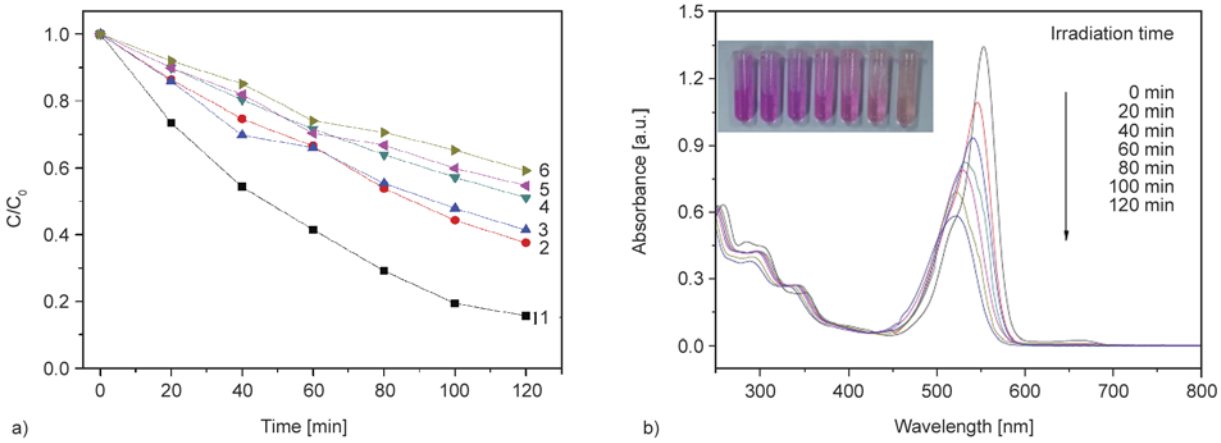

Figure 10. (a) The photodegradation of RhB (1), Rh6G (2), MB (3) over MIP_{RhB}-PPy/TiO_2 and MB (4), Rh6G (5), RhB 6) over NIP-PPy/TiO_2 (b) temporal UV-vis absorption spectral changes during the photocatalytic degradation of MIP_{RhB}-PPy/TiO_2 toward RhB

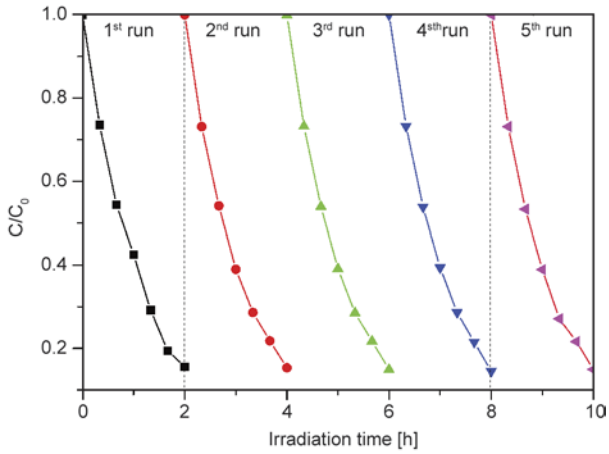

Figure 12. Results of cycling runs of RhB degradation over MIP_{RhB}-PPy/TiO_2

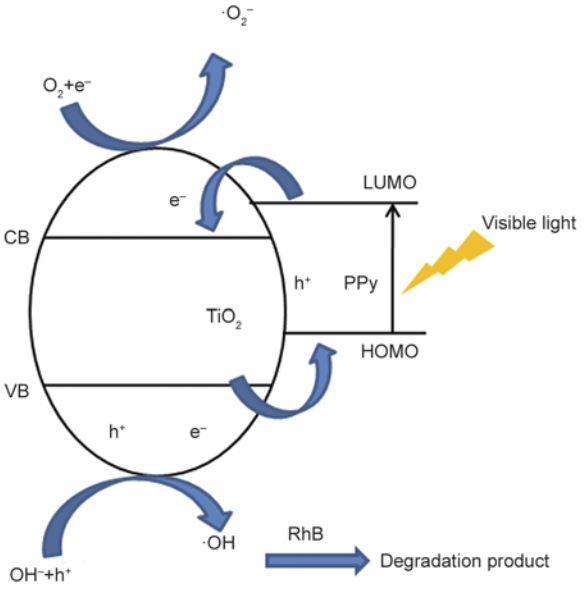

Figure 13. Scheme of the photocatalytic degradation of RhB over the MIP_{RhB}-PPy/TiO_2

52% and 46% of RhB over MIP_{RhB}-PPy/TiO_2, respectively. Moreover, the differences of the *k* values for the photodegradation of RhB, Rh6G and MB over NIP-PPy/TiO_2 are small. The possible explanation for this is that the MIP_{RhB}-PPy/TiO_2 and NIP-PPy/TiO_2 with almost the same element are remarkably different in their space-structure, the non-selective physical adsorption occurred between NIP-PPy/TiO_2 and RhB. In contrast, the MIP_{RhB}-PPy/TiO_2 adsorbed much more RhB than that of NIP-PPy/TiO_2 since MIP_{RhB}-PPy/TiO_2 had generated specific recognition sites in imprinting cavities. Compared with NIP-PPy/TiO_2, MIP_{RhB}-PPy/TiO_2 exhibited higher photocatalytic selectivity toward RhB.

Figure 12 shows the results of cycling runs of RhB degradation over MIP_{RhB}-PPy/TiO_2 The reusability and stability of MIP_{RhB}-PPy/TiO_2 was evaluated by the cycling runs for RhB photodegradation using the same imprinted photocatalyst. The degradation results were shown in Figure 12. It was found that the degradation ratios of RhB were almost kept stable around 80%. The photocatalytic activity does not obviously decline in RhB degradation after five recycling runs. Therefore, it can be inferred that the MIP_{RhB}-PPy/TiO_2 has high reusability and stability.

3.7. Photocatalytic mechanism

The mechanism of the photocatalytic degradation of RhB over the MIP_{RhB}-PPy/TiO_2 nanocomposites was proposed. At first, the RhB molecules can be adsorbed onto the imprinted layer of MIP_{RhB}-PPy/TiO_2 to form a moderately stable complex. When the MIP_{RhB}-PPy/TiO_2 nanocomposites are illuminated under visible light, the electrons of PPy can be excited from the highest occupied molecular orbital (HOMO) to the lowest unoccupied molecular orbital (LUMO). Since the conduction band (CB) of TiO_2 lies below the LUMO level of PPy, the excited electrons can be injected to CB of TiO_2, while holes will be left in HOMO of PPy. The electrons in valence band (VB) of TiO_2 can not only migrate to CB of TiO_2, but also to the HOMO of PPy to recombine with the holes, and simultaneously, holes were generated in the VB of TiO_2. Thus, more and more photo-generated electrons and holes form in TiO_2 nanoparticles. The photo-generated electrons migrate easily to the catalysts surface to react with oxygen to generate superoxide radicals ($\cdot O_2^-$), and the positive charged holes (h^+) can react with OH^- or H_2O to yield hydroxyl radicals (·OH). The resulting radicals are powerful enough to decompose oxidize RhB to the degradation products. The whole process can be clearly described as shown by Equation (12) and Figure 13 ([16, 34]).

$$MIP_{RhB}\text{-PPy/}TiO_2 + RhB \xrightarrow{\text{Adsorption}} MIP_{RhB}\text{-PPy/}TiO_2\text{-RhB} \quad (12)$$

4. Conclusions

A highly selective molecularly imprinted nanocomposites MIP_{RhB}-PPy/TiO_2 was successfully prepared by surface molecular imprinting technique with RhB as template molecule. MIP_{RhB}-PPy/TiO_2 exhibited obvious absorption under visible light. The transient photocurrent responses suggested that MIP_{RhB}-PPy/

TiO_2 could efficiently generate and separate of the electron-hole pairs. MIP_{RhB}-PPy/TiO_2 nanocomposites possessed strong affinity, high adsorption capacity, fast adsorption rate and excellent selectivity for RhB. In comparison with NIP-PPy/TiO_2, MIP_{RhB}-PPy/TiO_2 exhibited higher photocatalytic selectivity toward RhB under visible light. Therefore, the prepared nanocomposites MIP_{RhB}-PPy/TiO_2 has a promising perspective in industrial wastewater treatment.

Acknowledgements

This work was supported by the National Nature Science Foundation of China (No. 21206060)

References

[1] Asuha S., Zhou X. G., Zhao S.: Adsorption of methyl orange and Cr(VI) on mesoporous TiO_2 prepared by hydrothermal method. Journal of Hazardous Materials, **181**, 204–210 (2010).
DOI: 10.1016/j.jhazmat.2010.04.117

[2] Xu S. F., Li J. H., Chen L. X.: Molecularly imprinted core-shell nanoparticles for determination of trace atrazine by reversible addition–fragmentation chain transfer surface imprinting. Journal of Materials Chemistry, **21**, 4346–4351 (2011).
DOI: 10.1039/C0JM03593A

[3] Moon C-J., Lee J-H.: Use of curdlan and activated carbon composed adsorbents for heavy metal removal. Process Biochemistry, **40**, 1279–1283 (2005).
DOI: 10.1016/j.procbio.2004.05.009

[4] Wang G. H., Xu L., Zhang J., Yin T., Han D.: Enhanced photocatalytic activity of TiO_2 powders (P25) via calcination treatment. International Journal of Photoenergy, **2012**, 265760/1–265760/9 (2012).
DOI: 10.1155/2012/265760

[5] Bettinelli M., Dallacasa V., Falcomer D., Fornasiero P., Gombac V., Montini T., Romanò L., Speghini A.: Photocatalytic activity of TiO_2 doped with boron and vanadium. Journal of Hazardous Materials, **146**, 529–534 (2007).
DOI: 10.1016/j.jhazmat.2007.04.053

[6] Li X., Wang L., Lu X.: Preparation of silver-modified TiO_2 via microwave-assisted method and its photocatalytic activity for toluene degradation. Journal of Hazardous Materials, **177**, 639–647 (2010).
DOI: 10.1016/j.jhazmat.2009.12.080

[7] Tian G., Pan K., Fu H., Jing L., Zhou W.: Enhanced photocatalytic activity of S-doped TiO_2–ZrO_2 nanoparticles under visible-light irradiation. Journal of Hazardous Materials, **166**, 939–944 (2009).
DOI: 10.1016/j.jhazmat.2008.11.090

[8] Liu D., Xiao P., Zhang Y., Garcia B. B., Zhang Q., Guo Q., Champion R., Cao G.: TiO_2 nanotube arrays annealed in N_2 for efficient lithium-ion intercalation. Journal of Physical Chemistry C, **112**, 11175–11180 (2008).
DOI: 10.1021/jp801300j

[9] Li Y., Guo M., Peng S., Lu G., Li S.: Formation of multilayer-eosin Y-sensitized TiO_2 via Fe^{3+} coupling for efficient visible-light photocatalytic hydrogen evolution. International Journal of Hydrogen Energy, **34**, 5629–5636 (2009).
DOI: 10.1016/j.ijhydene.2009.05.100

[10] Xu S., Du A. J., Liu J., Ng J., Sun D. D.: Highly efficient CuO incorporated TiO_2 nanotube photocatalyst for hydrogen production from water. International Journal of Hydrogen Energy, **36**, 6560–6568 (2011).
DOI: 10.1016/j.ijhydene.2011.02.103

[11] Shang X., Hu G., He C., Zhao J., Zhang F., Xu Y., Zhang Y., Li J., Chen J.: Regeneration of full-scale commercial honeycomb monolith catalyst (V_2O_5–WO_3/TiO_2) used in coal-fired power plant. Journal of Industrial and Engineering Chemistry, **18**, 513–519 (2012).
DOI: 10.1016/j.jiec.2011.11.070

[12] Su P. G., Huang L. N.: Humidity sensors based on TiO_2 nanoparticles/polypyrrole composite thin films. Sensors and Actuators B: Chemical, **123**, 501–507 (2007).
DOI: 10.1016/j.snb.2006.09.052

[13] Cheng Q., He Y., Pavlinek V., Li C., Saha P.: Surfactant-assisted polypyrrole/titanate composite nanofibers: Morphology, structure and electrical properties. Synthetic Metals, **158**, 953–957 (2008).
DOI: 10.1016/j.synthmet.2008.06.022

[14] Alumaa A., Hallik A., Sammelselg V., Tamm J.: On the improvement of stability of polypyrrole films in aqueous solutions. Synthetic Metals, **157**, 485–491 (2007).
DOI: 10.1016/j.synthmet.2007.05.006

[15] Shaheen S. E., Brabec C. J., Sariciftci N. S., Padinger F., Fromherz T. Hummelen J. C.: 2.5% efficient organic plastic solar cells. Applied Physics Letters, **78**, 841–843 (2001).
DOI: 10.1063/1.1345834

[16] Deng F., Li Y., Luo X., Yang L., Tu X.: Preparation of conductive polypyrrole/TiO_2 nanocomposite via surface molecular imprinting technique and its photocatalytic activity under simulated solar light irradiation. Colloids and Surfaces A: Physicochemical and Engineering Aspects, **395**, 183–189 (2012).
DOI: 10.1016/j.colsurfa.2011.12.029

[17] Li J., Zhang Q., Feng J., Yan W.: Synthesis of PPy-modified TiO_2 composite in H_2SO_4 solution and its novel adsorption characteristics for organic dyes. Chemical Engineering Journal, **225**, 766–775 (2013).
DOI: 10.1016/j.cej.2013.03.011

[18] Jia Y., Xiao P., He H., Yao J., Liu F., Wang Z., Li Y.: Photoelectrochemical properties of polypyrrole/TiO_2 nanotube arrays nanocomposite under visible light. Applied Surface Science, **258**, 6627–6631 (2012). DOI: 10.1016/j.apsusc.2012.03.092

[19] Zhu B., Zhu M., Zhang Q., Cheng L., Li Y., Wang H.: Conducting behaviors of PPy/ITO composites synthesized by polymerization. Synthetic Metals, **160**, 2151–2154 (2010). DOI: 10.1016/j.synthmet.2010.07.045

[20] Zhang C., Li Q., Li J.: Synthesis and characterization of polypyrrole/TiO_2 composite by *in situ* polymerization method. Synthetic Metals, **160**, 1699–1703 (2010). DOI: 10.1016/j.synthmet.2010.06.003

[21] Babazadeh M., Gohari F. R., Olad A.: Characterization and physical properties investigation of conducting polypyrrole/TiO_2 nanocomposites prepared through a one-step '*in situ*' polymerization method. Journal of Applied Polymer Science, **123**, 1922–1927 (2012). DOI: 10.1002/app.34689

[22] Zhang G., Choi W., Kim S. H., Hong S. B.: Selective photocatalytic degradation of aquatic pollutants by titania encapsulated into FAU-type zeolites. Journal of Hazardous Materials, **188**, 198–205 (2011). DOI: 10.1016/j.jhazmat.2011.01.105

[23] Miyayama S., Nishijima K., Kamai T., Chiyoya T., Tsubota T., Ohno T.: Photocatalytic selective oxidation of anionic compounds on TiO_2 photocatalysts modified with quaternary ammonium base groups. Separation and Purification Technology, **58**, 206–210 (2007). DOI: 10.1016/j.seppur.2007.07.030

[24] Inumaru K., Murashima M., Kasahara T., Yamanaka S.: Enhanced photocatalytic decomposition of 4-nonylphenol by surface-organografted TiO_2: A combination of molecular selective adsorption and photocatalysis. Applied Catalysis B: Environmental, **52**, 275–280 (2004). DOI: 10.1016/j.apcatb.2004.04.013

[25] Damin A., Llabrés i Xamena F. X., Lamberti C., Civalleri B., Zicovich-Wilson C. M., Zecchina A.: Structural, electronic, and vibrational properties of the Ti–O–Ti quantum wires in the titanosilicate ETS-10. The Journal of Physical Chemistry B, **108**, 1328–1336 (2004). DOI: 10.1021/jp036902e

[26] Shen X., Zhu L., Li J., Tang H.: Synthesis of molecular imprinted polymer coated photocatalysts with high selectivity. Chemical Communications, **2007**, 1163–1165 (2007). DOI: 10.1039/B615303H

[27] Wang X-J., Xu Z-L., Feng J-L., Bing N-C., Yang Z-G.: Molecularly imprinted membranes for the recognition of lovastatin acid in aqueous medium by a template analogue imprinting strategy. Journal of Membrane Science, **313**, 97–105 (2008). DOI: 10.1016/j.memsci.2007.12.067

[28] Xiao D., Dramou P., Xiong N., He N., Li H., Yuan D., Dai H.: Development of novel molecularly imprinted magnetic solid-phase extraction materials based on magnetic carbon nanotubes and their application for the determination of gatifloxacin in serum samples coupled with high performance liquid chromatography. Journal of Chromatography A, **1274**, 44–53 (2013). DOI: 10.1016/j.chroma.2012.12.011

[29] Duan Z., Yi J., Fang G., Fan L., Wang S.: A sensitive and selective imprinted solid phase extraction coupled to HPLC for simultaneous detection of trace quinoxaline-2-carboxylic acid and methyl-3-quinoxaline-2-carboxylic acid in animal muscles. Food Chemistry, **139**, 274–280 (2013). DOI: 10.1016/j.foodchem.2013.02.007

[30] Shen X., Zhu L., Liu G., Yu H., Tang H.: Enhanced photocatalytic degradation and selective removal of nitrophenols by using surface molecular imprinted titania. Environmental Science and Technology, **42**, 1687–1692 (2008). DOI: 10.1021/es071788p

[31] Zhao P., Hao J.: Tert-butylhydroquinone recognition of molecular imprinting electrochemical sensor based on core–shell nanoparticles. Food Chemistry, **139**, 1001–1007 (2013). DOI: 10.1016/j.foodchem.2013.01.035

[32] Luo X., Deng F., Min L., Luo S., Guo B., Zeng G., Au C.: Facile one-step synthesis of inorganic-framework molecularly imprinted TiO_2/WO_3 nanocomposite and its molecular recognitive photocatalytic degradation of target contaminant. Environmental Science and Technology, **47**, 7404–7412 (2013). DOI: 10.1021/es4013596

[33] Huo P., Lu Z., Liu X., Wu D., Liu X., Pan J., Gao X., Guo W., Li H., Yan Y.: Preparation photocatalyst of selected photodegradation antibiotics by molecular imprinting technology onto TiO_2/fly-ash cenospheres. Chemical Engineering Journal, **189-190**, 75–83 (2012). DOI: 10.1016/j.cej.2012.02.030

[34] Wang D., Wang Y., Li X., Luo Q., An J., Yue J.: Sunlight photocatalytic activity of polypyrrole–TiO_2 nanocomposites prepared by '*in situ*' method. Catalysis Communication, **9**, 1162–1166 (2008). DOI: 10.1016/j.catcom.2007.10.027

eXPRESS Polymer Letters Vol.8, No.11 (2014) 862–868
Available online at www.expresspolymlett.com
DOI: 10.3144/expresspolymlett.2014.87

Nitroxide polymer brushes prepared by surface-initiated ARGET ATRP and their selective oxidation performances

S. J. Liu[1,2*], *Q. Q. Hu*[1], *F. Q. Zhao*[1,2], *X. M. Chu*[1], *P. X. Li*[1], *E. J. Tang*[1]

[1]College of Chemical & Pharmaceutical Engineering, Hebei University of Science and Technology, 050018 Shijiazhuang, PR China
[2]Hebei Provincial Engineering and Technology Research Center of Solid Waste Utilization, 050018 Shijiazhuang, PR China

Received 3 April 2014; accepted in revised form 18 June 2014

Abstract. Polymer brushes with 2,2,6,6-tetramethyl-4-piperidyl methacrylate (TMPM) units, grafted on the cross-linked polystyrene (PS) microspheres, were synthesized *via* surface-initiated ARGET (activators regenerated by electron transfer) ATRP (atom transfer radical polymerization). They were further oxidized to yield nitroxide polymer brushes containing nitroxide radical units (TEMPO). The obtained polymer brushes were characterized by Fourier transform infrared spectroscopy (FT-IR), scanning electron microscopy (SEM), transmission electron microscopy (TEM), electron spin resonance (ESR) and gel permeation chromatography (GPC). The catalytic properties of nitroxide polymer brushes for selective oxidation of benzyl alcohol were investigated. The results showed that the performances were good and the yield was up to 96%. Furthermore, the block brush had similar catalyst properties to non-supported TEMPO in terms of activity and selectivity. It could be recovered by centrifugation. The unity of high catalyst property and easy recovery was achieved.

Keywords: *tailor-made polymers, nitroxide polymer brushes, selective oxidation, ARGET ATRP*

1. Introduction

Poly(2,2,6,6-tetramethylpiperidin-1-oxyl-4-yl methacrylate) (PTMA) is a kind of promising cathode-active materials for organic radical batteries [1–5]. It is a polymer containing methacrylate backbone grafted with 2, 2, 6, 6-tetramethylpiperidin-1-oxyl-4-yl (TEMPO). TEMPO is a stable nitroxide radical. In order to prevent the nitroxide radical polymer dissolving into the electrolytes, Lee and coworkers [3–5] synthesized nitroxide polymer brushes which the PTMA was grafted onto the surface of silica, indium tin oxide and other substrates *via* surface-initiated ATRP, and the electrochemical properties were improved.

Besides, TEMPO is a good catalyst for catalytic selective oxidation of alcohol. However, the price of TEMPO is high, and its residue in the final products may affect the product purity. In the laboratory, product can be purified by column chromatography. However, the implementation is difficult in large-scale industrial production. So measures should be taken to make TEMPO recycled. To solve this problem, TEMPO has been immobilized onto inorganic (such as silica, activated carbon, molecular sieve and aluminum oxide) and organic supports (such as polymers and ionic liquids) affording solid catalysts, which are readily separated from the reaction mixtures. Using polymer as carrier, the grafting of TEMPO was easy, and some supported TEMPO showed new catalytic features compared with the non-supported TEMPO [6–16]. However, these polymer supports had, in general, a detrimental effect on the rates of reaction when compared to unsupported species. Furthermore, the supported amounts and

*Corresponding author, e-mail: sjliu16@163.com

location were also difficult to control. While the PTMA brush with TEMPO groups, it can be seen as a polymer brush supported TEMPO catalyst system. With the help of special designed brush structure and preparation method, the above problems may be solved.

Compared with the traditional ATRP method, ARGET ATRP uses significantly reduced copper catalyst concentration (down to ppm levels) and also imparts a degree of oxygen tolerance to the reaction [17]. These advantages make it a potentially more industrially attractive technique. ARGET ATRP has proven to be a very efficient tool in the preparation of polymer brushes. The used substrates include cellulose [18], polymer microspheres [19], silica [20], carbon nanotubes [21], etc. The used monomers include methyl methacrylate (MMA), styrene (St), methyl glycidyl ester of acrylic (GMA), etc. Recently, synthesis of tert-butyl methacrylate/2-(dimethylamino ethyl) methacrylate based densely grafted brushes by ATRP/AGET ATRP was reported by Gromadzki *et al.* [22]. Stimuli-responsive polyampholyte brushes were obtained by quantitative hydrolysis of tert-butyl methacrylate units. To the best of our knowledge, grafting nitroxide polymer brushes on cross-linked PS microspheres *via* ARGET ATRP and using them as catalysts for selective oxidation of alcohols have not yet been reported.

In this paper, polymer brushes with TMPM units on the cross-linked PS microspheres, were synthesized *via* surface-initiated ARGET ATRP. Then piperidyl was oxidized by m-chloroperoxybenzoic acid (mCPBA) into nitroxide radical. The nitroxide polymer brushes were produced. These nitroxide polymer brushes were used as catalysts for selective oxidation of benzyl alcohol. With the insolubility of cross-linked PS microsphere matrix and the solubility of linear nitroxide polymer brushes, the high catalytic property and easy recovery performance were achieved.

2. Materials and methods

2.1. Materials

α-Bromoisobutyryl bromide (98%), copper (II) bromide ($CuBr_2$, 99%), Tin(II) 2-ethylhexanoate ($Sn(EH)_2$, 95%) and N,N,N′,N″,N″-pentamethyldiethylenetriamine (PMDETA, 99%), were obtained from Aladdin Industrial Corporation (Shanghai, China) and used as received. m-Chloroperoxybenzoic acid (mCPBA, 75%) purchased from J&K Chemical (Beijing, China) was recrystallized in methanol before use. 2,2,6,6-Tetramethyl-4-piperidyl methacrylate (TMPM, 98%) were purchased from Tokyo Chemical Industry Co., Ltd. (Tokyo, Japan). Other monomers including styrene (St, 99%), divinylbenzene (DVB, 55%), hydroxyethyl methacrylate (HEMA, 96%) and methyl methacrylate (MMA, 99%) were offered by Aladdin Industrial Corporation (Shanghai, China). These monomers were passed through a column of neutral aluminum oxide prior to use to remove the inhibitor. Other reagents were from Sinopharm Chemical Reagent Company (China) and used without further purification.

2.2. Synthesis of nitroxide polymer brushes on cross-linked PS microspheres

In this study, we prepared two nitroxide polymer brushes: the homopolymer brush of PTMA and the block polymer brush of P(MMA-b-TMA). The preparation process of P(MMA-b-TMA) brush was illustrated in Figure 1.

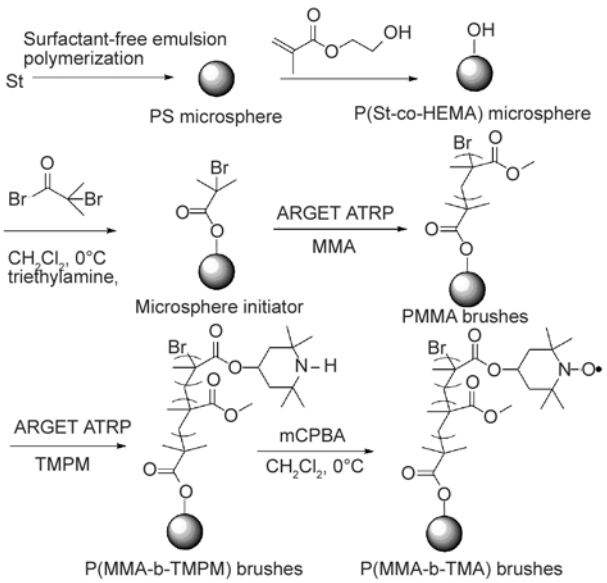

Figure 1. Synthesis of P(MMA-b-TMA) brushes on PS microspheres

2.2.1. Preparation of cross-linked P(St-co-HEMA) microspheres by soap-free emulsion polymerization

The cross-linked P(St-co-HEMA) microspheres were prepared by a soap-free emulsion polymerization in a 1000 mL round-bottom flask equipped with a mechanical stirrer and reflux condenser at N_2 atmosphere. 27 g St, 1.3 g DVB, 0.054 g NaOH, 0.054 g $NaHCO_3$ and 500 mL distilled water were

added to the reactor. When the temperature rose to 75°C, initiator solutions (0.5 g potassium persulfate dissolved in 40 mL water) was added to initiate the polymerization. 2.7 g HEMA was added 5 hours later. After 3 hours' polymerization, the cross-linked P(St-co-HEMA) microspheres were obtained by centrifuging and drying.

2.2.2. Immobilization of ATRP initiator on cross-linked P(St-co-HEMA) microspheres

In an ice bath, α-bromoisobutyryl bromide (1.8 g, 8 mmol) was added to a dispersion of microspheres (5 g) and triethylamine (0.9 g, 9 mmol) in CH_2Cl_2 (100 mL). The reaction was quenched by the addition of methanol after 5 hours of gentle stirring at ambient temperature. The microspheres were centrifuged, washed with CH_2Cl_2, methanol and dried at ambient conditions.

2.2.3. Synthesis of PTMPM brush *via* surface-initiated ARGET ATRP

In nitrogen atmosphere, anisole (30 mL) and TMPM (5 g, 22.2 mmol) were added to a 50 mL three-necked flask. After TMPM was dissolved, added $CuBr_2$ (4.5 mg, 0.02 mmol) and PMDETA (0.083 mL, 0.4 mmol) at 40°C. Then the macromolecular initiator (1.25 g, containing 0.4 mmol Br) was added. When the system completely decentralized and the temperature rose to 80°C, $Sn(EH)_2$ (0.13 mL, 0.4 mmol) was added to initiate the reaction. After 105 min, the polymerization was stopped by exposing the solution to air. The PTMPM brush was obtained by centrifugation, washing with anisole, and dried in a vacuum oven at 60°C to constant weight.

The synthesis of block copolymer brush of P(MMA-b-TMPM) was similar to the above process. Firstly PMMA brush was prepared, and then P(MMA-b-TMPM) block brush was obtained through using PMMA brush as the macromolecular initiator and TMPM as the monomer.

2.2.4. Synthesis of nitroxide polymer brushes

PTMPM brush (1.654 g) was dispersed in 60 mL of CH_2Cl_2. Then, 20 mL CH_2Cl_2 solution of mCPBA (1 g, 5.9 mmol) was dropped at 0°C. After 1 h, the mixture was poured into 120 mL n-hexane, and the orange precipitate appeared. Then the pink solid product was washed and ultrasonicated again with dimethyl formamide (DMF) three times and dried in a vacuum oven for 24 hours at 60°C to give PTMA brush. With similar process, the P(MMA-b-TMA) brush was obtained.

2.2.5. Basic hydrolysis of polymer brush

50 mL of a 1 M KOH/ethanol solution was added to 100 mg of polymer brush in 200 mL of tetrahydrofuran (THF). The mixture was refluxed at 80°C for 72 hrs, followed by filtration and then redissolved into THF. The resultant polymer was precipitated by the addition of acidified methanol.

2.2.6. Characterization of polymer brushes

The particle size of polymer microsphere was measured by laser particle size analyzer (Zetasizer Malvern Nano S90, Malvern Instruments Ltd, United Kingdom). The Br content of macromolecular initiator was estimated by Automatic Elemental Analyzer (Chncorder-MF-3, United States). The monomer conversion of polymerization was given by gravimetry method. The morphology of polymer brush was characterized by using TEM (Jeol 100CX-II, Jeol Co., Japan) and SEM (S-4800-I, HITACHI, Japan). After polymer brushes cut from the substrate surface by hydrolysis, the number molecular weight (M_n) and dispersity index (D) were determined using THF (0.8 mL/min) as the mobile phase at 45°C by GPC (Waters GPCV 2000 with a combined refractive index and viscosity detector, United States). A universal calibration method was performed using series of narrow linear polystyrene standards. Conversion of PTMA brush from PTMPM brush was estimated by electron spin resonance (ESR, Bruker EMX-10, United States) [3].

2.3. General process for benzyl alcohol oxidation

8.6 mL of NaClO aqueous solution (0.121 $g \cdot mL^{-1}$) and 8.6 mL of $NaHCO_3$ aqueous solution (0.05 $g \cdot mL^{-1}$) were added to a solution of benzyl alcohol (1.2 mL, 11.5 mmol) in 10 g of CH_2Cl_2 containing 1% mol of polymer brush supported TEMPO [PTMA 0.091 g or P(MMA-b-TMA) 0.065 g] and 10% mol of KBr (0.137 g, 1.15 mmol). The reaction mixture was stirred at 0°C for 3 mins. Then, $Na_2S_2O_3$ was added to stop the reaction. The organic phase was separated, dried over $MgSO_4$, and finally analyzed by gas chromatography (GC). The process was illustrated in Figure 2.

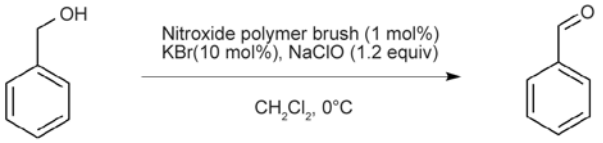

Figure 2. Oxidation of benzyl alcohol by the nitroxide polymer brush

2.4. General procedure for the recovery of P(MMA-b-TMA) brush

The P(MMA-b-TMA) brush was retrieved and circulated use. The brushes in aqueous phase were deposited by filtration, washing with DMF and drying. Repeated the above operation (see section 2.3) 5 times to study the catalytic properties of recycled brushes.

3. Results and discussion

3.1. Synthesis of cross-linked PS microspheres with ATRP initiator

The cross-linked surface-hydroxylated PS microspheres, P(St-co-HEMA), were prepared by soap-free emulsion polymerization. From the SEM image in Figure 3a, it was seen that P(St-co-HEMA) had the particle size of about 400 nm, in accordance with the dynamic light scattering result (425 nm). Through the O-acylation reaction of the surface hydroxyl groups of P(St-co-HEMA) with α-bromoisobutyryl bromide, the ATRP initiator was immobilized. The content of Br in these particles was about 0.32 mmol/g, which was estimated by the elemental analysis result. These microspheres were used as macromolecular initiators to prepare polymer brushes.

3.2. Synthesis of nitroxide polymer brushes

3.2.1. Homopolymer brush of PTMPM

The PTMPM brush was prepared by surface-initiated ARGET ATRP. The SEM image (Figure 3b) showed that PTMPM brushes/PS nanoparticles had a slight adhesion due to the presence of polymer brushes. Similar phenomenon was reported by Lin *et al.* [3] when they grafted nitroxide polymer brushes on silica nanoparticles. Its FT-IR spectrum (ATR, cm^{-1}) could be seen in Figure 4: 972 (m), 1152 (vs, vas (OCC=O)), 1236 (s, vas (CC=O)), 1378 (m, δs (CH_3)), 1452 (m, d (CH_2)), 1724(vs, v (C=O)), 2960 (m, v(CH)), 3332 (m), 3423 (m, v (NH)).

TEM images (Figure 5a, 5b) indicated that the brushes showed a core-shell structure. The core was PS matrix with a diameter of about 400 nm and the shell was a layer of TMPM polymer chains. Particle size of PTMPM homopolymer brush was about 500 nm. The adhesion among the particles may be caused by the intertwining of brushes. Therefore, the PTMPM brush was successfully prepared.

Grafting density (chains nm^{-2}) of polymer brush was calculated according to the Equation (1):

$$\text{grafting density} = \frac{W}{M \cdot S} \cdot N_A \cdot 10^{-18} \quad (1)$$

where W was the grafting amount of polymer brush [g] polymer brush/g matrix; M was the number

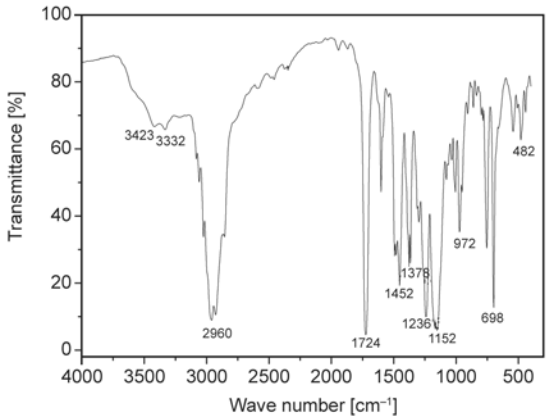

Figure 4. FT-IR spectrum for PTMPM brushes/P(St-co-HEMA) microspheres

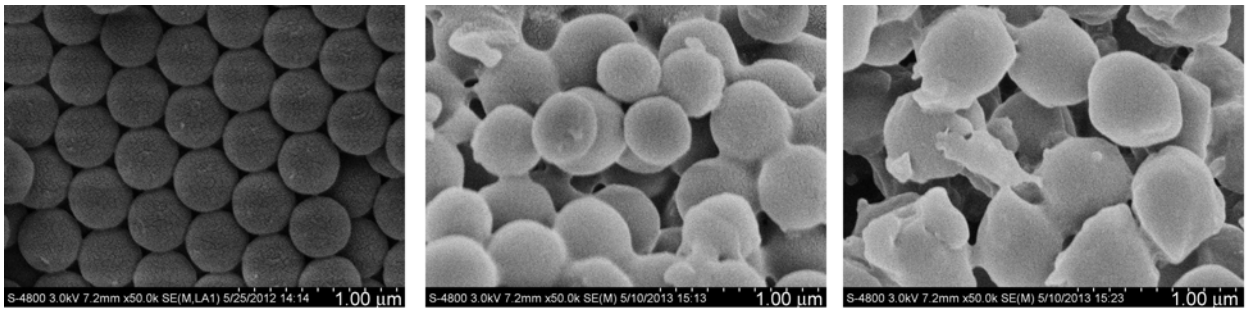

Figure 3. SEM micrographs for the bare P(St-co-HEMA) microspheres (a), PTMPM brushes/P(St-co-HEMA) microspheres (b) and P(MMA-b-TMPM) brushes/P(St-co-HEMA) microspheres (c)

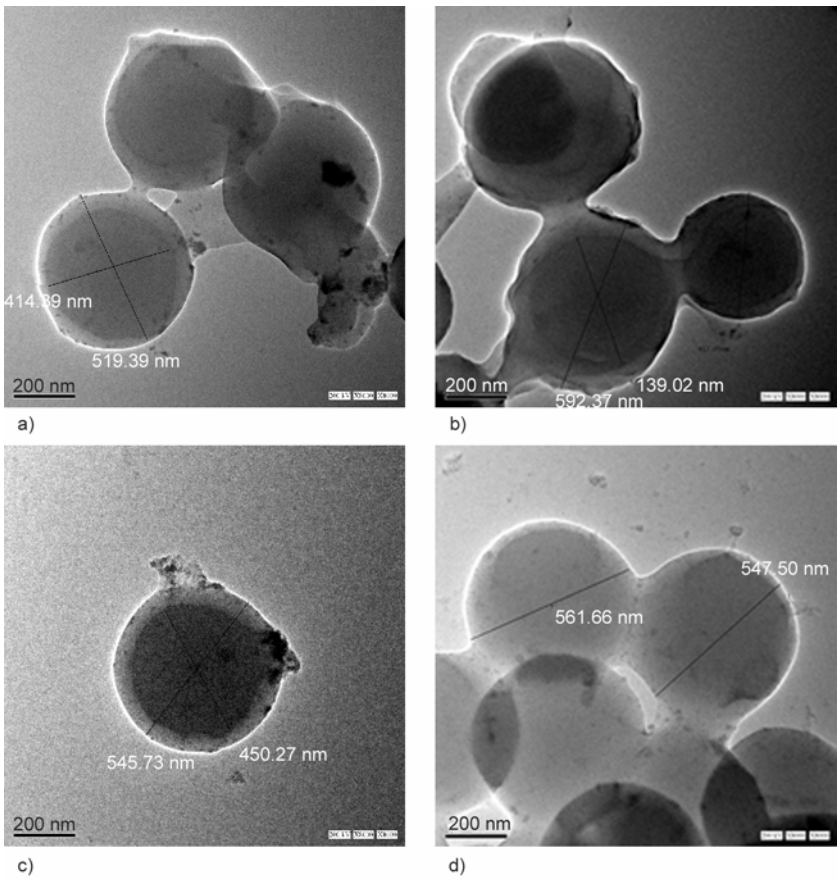

Figure 5. TEM micrographs of the prepared polymer brushes: PTMPM brushes/P(St-co-HEMA) microspheres, (a) and (b); P(MMA-b-TMPM) brushes/P(St-co-HEMA) microspheres, (c) and (d)

average molecular weight of the polymer brush [g/mol]. S was the specific surface area [$m^2 \cdot g^{-1}$]. N_A was Avogadro's number.

For the PTMPM brush, the grafting amount was 0.75 g TMPM brush/g substrate. Brushes were cut down from PS matrix by hydrolysis. It was measured that M_n = 16 000 g/mol and dispersity index (D) = 1.25. The grafting density was about 3.3 chains nm^{-2}. This grafting density was higher than that on silica nanoparticles, which was about 1 chains nm^{-2} [3].

3.2.2. Block copolymer brush of P(MMA-b-TMPM)

The block copolymer brush of P(MMA-b-TMPM) was synthesized with the process as shown in Figure 1. From the SEM micrograph in Figure 3c, particles with P(MMA-b-TMPM) brushes had an irregular shape and were non-spherical. The long brushes may be intertwined with each other. It was seen from the TEM images (Figure 5c, 5d) that, the particles with block brushes also showed a core-shell structure.

The grafting amount of block copolymer brush of P(MMA-b-TMPM) was 0.69 g TMPM brush/g substrate. Its M_n was 22 000 g/mol and D was 1.41. The grafting density was about 3.8 chains nm^{-2}.

3.2.3. Preparation of nitroxide polymer brushes

The piperidyl groups of PTMPM and P(MMA-b-TMPM) brushes were oxidized by mCPBA into nitroxide radical, and two nitroxide polymer brushes (PTMA and P(MMA-b-TMA)) were obtained.

Because FT-IR spectra of PTMA was similar with PTMPM (the absorption peak of N–O· was very weak) [3], so the spectrum could not be used to judge whether the reaction occurred. But during the course of the experiment, the phenomenon was obvious that the system changed from white to orange. The commercial TEMPO was orange. Furthermore, the conversion for TEMPO of the nitroxide polymer brushes were measured by ESR [3]. The conversion was about 95% after the oxidation. The nitroxide polymer brushes prepared in this work showed a high level of TEMPO immobilization, 3.1 $mmol \cdot g^{-1}$ for PTMA and 3.6 $mmol \cdot g^{-1}$ for P(MMA-b-TMA). This density level is considerably higher than that of the TEMPO polymer grafted on silica (up to 2.1 $mmol \cdot g^{-1}$) [23].

3.3. The performance of nitroxide polymer brushes for catalytic oxidation of benzyl alcohol

With NaClO as the oxidant, the nitroxide polymer brushes as catalysts, benzyl alcohol was selectively oxidized to benzaldehyde. The catalyst performance of nitroxide polymer brushes was compared with non-supported TEMPO. GC results showed that the system possessed excellent selectivity using non-supported TEMPO, PTMA brush and P(MMA-b-TMA) brush as catalysts. No characteristic peaks of benzoic acid were found. The yield of benzaldehyde was, 95, 91 and 96%, respectively. Block copolymer brush of P(MMA-b-TMA) had similar results with non-supported TEMPO. It may be that the special structure of block brushes made TEMPO groups mainly distributed in the outer of particles, which was helpful to fully contact with the reactants.

Recycling performance of the P(MMA-b-TMA) brush was investigated after the filtration recovery. The yield results for 5 cycles, were shown in Figure 6. It was found that the yield did not fall significantly after 5 cycles. Furthermore, benzoic acid was not detected. The high catalytic activities and preservation of activity upon recycling of these brushes may be attributed to enhanced regeneration of the nitroxyl species as a result of intramolecular synproportionation [10]. The oxidation for other primary alcohols and seconday alcohols is under work.

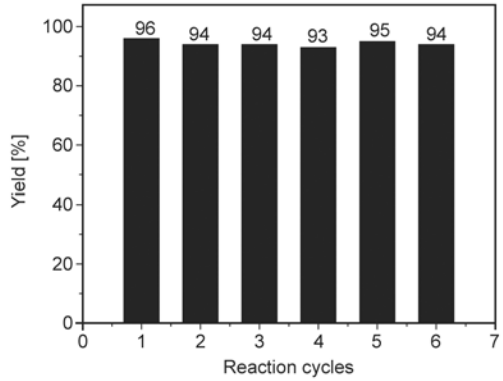

Figure 6. Recyclability of P(MMA-b-TMA) brushes in the oxidation of benzyl alcohol to benzaldehyde

4. Conclusions

The surface-hydroxylated cross-linked PS microspheres were prepared by soap-free emulsion polymerization, and then ATRP initiator was supported on them. Using these microspheres as macromolecular initiators, the homopolymer brush of PTMPM and block copolymer brush of P(MMA-b-TMPM) were synthesized *via* surface-initiated ARGET ATRP, and the grafting density was 3.3 and 3.8 chains nm^{-2} respectively. PTMPM and P(MMA-b-TMPM) brushes were further oxidized by mCPBA to yield nitroxide polymer brushes of PTMA and P(MMA-b-TMA) with TEMPO groups. With NaClO as oxidant, selective oxidation of benzyl alcohol to benzaldehyde as template reaction, the catalytic performances of nitroxide polymer brushes were studied. The results showed that the brushes had excellent catalytic properties, and the P(MMA-b-TMA) brush demonstrated an equivalent catalytic performance with the non-supported TEMPO. The catalyst system was easy to recycle, and the yield did not fall significantly after 5 cycles.

Acknowledgements

This study was supported by Natural Science Foundation of China (NO. 21304030), Natural Science Foundation of Hebei Province (NO. B2012208017) and Outstanding Youth Fund in Hebei Province Department of Education (NO. YQ2013001). Here we expressed the heartfelt thanks for the support.

References

[1] Janoschka T., Teichler A., Krieg A., Hager M. D., Schubert U. S.: Polymerization of free secondary amine bearing monomers by RAFT polymerization and other controlled radical techniques. Journal of Polymer Science Part A: Polymer Chemistry, **50**, 1394–1407 (2012). DOI: 10.1002/pola.25907

[2] Hauffman G., Rolland J., Bourgeois J-P., Vlad A., Gohy J-F.: Synthesis of nitroxide-containing block copolymers for the formation of organic cathodes. Journal of Polymer Science Part A: Polymer Chemistry, **51**, 101–108 (2013). DOI: 10.1002/pola.26279

[3] Lin H-C., Li C-C., Lee J-T.: Nitroxide polymer brushes grafted onto silica nanoparticles as cathodes for organic radical batteries. Journal of Power Sources, **196**, 8098–8103 (2011). DOI: 10.1016/j.jpowsour.2011.05.037

[4] Wang Y-H., Hung M-K., Lin C-H., Lin H-C., Lee J-T.: Patterned nitroxide polymer brushes for thin-film cathodes in organic radical batteries. Chemical Communications, **47**, 1249–1251 (2011). DOI: 10.1039/c0cc02442b

[5] Lin C-H., Chou W-J., Lee J-T.: Three-dimensionally ordered macroporous nitroxide polymer brush electrodes prepared by surface-initiated atom transfer polymerization for organic radical batteries. Macromolecular Rapid Communications, **33**, 107–113 (2012). DOI: 10.1002/marc.201100548

[6] Dijksman A., Arends I. W. C. E., Sheldon R. A.: Polymer immobilised TEMPO (PIPO): An efficient catalyst for the chlorinated hydrocarbon solvent-free and bromide-free oxidation of alcohols with hypochlorite. Chemical Communications, **2000**, 271–272 (2000). DOI: 10.1039/A909690F

[7] Dijksman A., Arends I. W. C. E., Sheldon R. A.: A comparison of the activity of polymer immobilised TEMPO (PIPO) with MCM-41 and silica supported TEMPO as heterogeneous catalysts for the oxidation of alcohols. Synlett, **2001**, 0102–0104 (2001). DOI: 10.1055/s-2001-9708

[8] Ferreira P., Hayes W., Phillips E., Rippon D., Tsang S. C.: Polymer-supported nitroxyl catalysts for selective oxidation of alcohols. Green Chemistry, **6**, 310–312 (2004). DOI: 10.1039/B406829G

[9] Ferreira P., Phillips E., Rippon D., Tsang S. C., Hayes W.: Poly(ethylene glycol)-supported nitroxyls: Branched catalysts for the selective oxidation of alcohols. The Journal of Organic Chemistry, **69**, 6851–6859 (2004). DOI: 10.1021/jo0490494

[10] Ferreira P., Phillips E., Rippon D., Tsang S. C.: Catalytic oxidation of alcohols using molecular oxygen mediated by poly(ethylene glycol)-supported nitroxyl radical. Applied Catalysis B: Environmental, **61**, 206–211 (2005). DOI: 10.1016/j.apcatb.2005.05.006

[11] Pozzi G., Cavazzini M., Quici S., Benaglia M., Dell'Anna G.: Poly(ethylene glycol)-supported TEMPO: An efficient, recoverable metal-free catalyst for the selective oxidation of alcohols. Organic Letters, **6**, 441–443 (2004). DOI: 10.1021/ol036398w

[12] Benaglia M., Puglisi A., Holczknecht O., Quici S., Pozzi G.: Aerobic oxidation of alcohols to carbonyl compounds mediated by poly(ethylene glycol)-supported TEMPO radicals. Tetrahedron, **61**, 12058–12064 (2005). DOI: 10.1016/j.tet.2005.07.107

[13] Gilhespy M., Lok M., Baucherel X.: Polymer-supported nitroxyl radical catalysts for the hypochlorite and aerobic oxidation of alcohols. Catalysis Today, **117**, l14–119 (2006). DOI: 10.1016/j.cattod.2006.05.039

[14] Gilhespy M., Lok M., Baucherel X.: Polymer-supported nitroxyl radical catalyst for selective aerobic oxidation of primary alcohols to aldehydes. Chemical Communications, **2005**, 1085–1086 (2005). DOI: 10.1039/B415902K

[15] Tanyeli C., Gümüs A.: Synthesis of polymer-supported TEMPO catalysts and their application in the oxidation of various alcohols. Tetrahedron Letters, **44**, 1639–1642 (2003). DOI: 10.1016/S0040-4039(03)00003-0

[16] Kashiwagi Y., Ikezoe H., Ono T.: Oxidation of alcohols with nitroxyl radical resins under two-phase conditions. Synlett, **2006**, 69–72 (2006). DOI: 10.1055/s-2005-922775

[17] Braunecker W. A., Matyjaszewski K.: Controlled/living radical polymerization: Features, developments, and perspectives. Progress in Polymer Science, **32**, 93–146 (2007). DOI: 10.1016/j.progpolymsci.2006.11.002

[18] Hansson S., Östmark E., Carlmark A., Malmström E.: ARGET ATRP for versatile grafting of cellulose using various monomers. ACS Applied Materials and Interfaces, **1**, 2651–2659 (2009). DOI: 10.1021/am900547g

[19] Jonsson M., Nyström D., Nordin O., Malmström E.: Surface modification of thermally expandable microspheres by grafting poly(glycidyl methacrylate) using ARGET ATRP. European Polymer Journal, **45**, 2374–2382 (2009). DOI: 10.1016/j.eurpolymj.2009.05.002

[20] Cheesman B. T., Willott J. D., Webber G. B., Edmondson S., Wanless E. J.: pH-responsive brush-modified silica hybrids synthesized by surface-initiated ARGET ATRP. ACS Macro Letters, **1**, 1161–1165 (2012). DOI: 10.1021/mz3003566

[21] Aitchison T. J., Markovic M-G., Saunders M., Fredericks P., Valiyaveettil S., Matisons J. G., Simon G. P.: Polymer brushes on multiwalled carbon nanotubes by activators regenerated by electron transfer for atom transfer radical polymerization. Journal of Polymer Science Part A: Polymer Chemistry, **49**, 4283–4291 (2011). DOI: 10.1002/pola.24872

[22] Gromadzki D., Štěpánek P., Makuška R.: Synthesis of densely grafted copolymers with *tert*-butyl methacrylate/2-(dimethylamino ethyl) methacrylate side chains as precursors for brush polyelectrolytes and polyampholytes. Materials Chemistry and Physics, **137**, 709–715 (2013). DOI: 10.1016/j.matchemphys.2012.09.012

[23] Saito K., Hirose K., Okayasu T., Nishide H., Hearn M. T. W.: TEMPO radical polymer grafted silicas as solid state catalysts for the oxidation of alcohols. RSC Advances, **3**, 9752–9756 (2013). DOI: 10.1039/C3RA41823E

eXPRESS Polymer Letters Vol.8, No.11 (2014) 869–879
Available online at www.expresspolymlett.com
DOI: 10.3144/expresspolymlett.2014.88

Towards the understanding of the molecular weight dependence of essential work of fracture in semi-crystalline polymers: A study on poly(ε-caprolactone)

F. Tuba[1,2*], *L. Oláh*[2], *P. Nagy*[1]

[1]Department of Polymer Engineering, Faculty of Mechanical Engineering, Budapest University of Technology and Economics, Műegyetem rkp. 3., 1111 Budapest, Hungary
[2]Audi Hungaria Motor Kft., Kardán utca 1., 9027 Győr, Hungary

Received 16 February 2014; accepted in revised form 23 June 2014

Abstract. The plane-stress ductile fracture of poly(ε-caprolactone) (PCL) has been investigated as a function of molecular weight and related crystalline structure. Because of the interacting effects in semi-crystalline polymers a separate study of a given structural parameter is rather challenging. Nevertheless, this polymer seems to be a good model material to study the effect of molecular weight on the essential work of fracture, as the interactions between the separate parameters, at room temperature, are negligible. The molecular characteristics of PCL were determined by size exclusion chromatography. To confirm the entangled molecular structure of studied polymers rheological measurements were performed. The crystalline morphology has been characterized by differential scanning calorimetry and wide angle X-ray diffraction. Quasi-static tensile tests and essential work of fracture tests were performed to study the mechanical behavior. Based on the experimental observations an empirical model has been proposed to outline the molecular weight and crystallinity dependence of the essential work of fracture in this semi-crystalline polymer.

Keywords: *biodegradable polymers, mechanical properties, poly(ε-caprolactone) (PCL), essential work of fracture (EWF), molecular weight dependence*

1. Introduction

Although often disregarded, fracture toughness is one of the most important aspects of material characteristics in engineering applications. Due to their stress concentrating effect, micro- and nanoscale cracks could induce catastrophic failure well below the load bearing ability of the material. To avoid this, effective flaw assessment methods have to be developed [1]. For the analysis of thick, rather brittle materials standardized test methods are available (ASTM E1820-11, ISO 12135). These are applicable under small-scale yielding conditions, i.e. up to a ligament yielding parameter – the ratio of the applied and the yield load – of 0.5. For ductile materials this parameter is usually above 0.8, thus the linear elastic and adjusted methods generally underestimate the fracture resistance [1]. Additionally, thin-walled structures generally do not meet the thickness requirements of standardized methods, and the empirical equations describing geometry dependent plane-stress fracture resistance cannot treat the effects of ligament yielding. However, thin-walled elements are frequently used from simple packaging applications to lightweight-constructions of industrial areas like automotive, aerospace, shipbuilding, piping, etc.

Therefore, over the last decades several concepts have been developed to characterize the fracture of

*Corresponding author, e-mail: ferenc.tuba@audi.hu

ductile thin-walled geometries [1–3]. One of these is the essential work of fracture method (EWF), which became widespread as its test set-up is less complex and the restrictions of method are easier to fulfill compared to *J*-integral [4]. Originally the EWF method was developed for the analysis of ductile metals, and to describe elastic-plastic behavior from crack initiation through stable crack propagation under plane-stress conditions. The theory says that by testing geometrically similar specimens one can split the total fracture work (W_f) into a dissipative work of outer screening plastic zone (W_p), and into an essential one (W_e) that is required for the formation of the new crack surfaces in the inner fracture process zone. If the specimen is under quasi plane-stress conditions, the entire ligament (L) yields before crack initiation, and the plastic zone is confined, then the plastic work is proportional to the plastic volume ($\beta \cdot B \cdot L^2$), while the essential one is proportional to fracture area ($B \cdot L$). Since both fracture works are assumed to be proportional to the initial cross section ($B \cdot L$) and to the ligament length (L); the total work of fracture can be partitioned into the specific essential (w_e) and non-essential (w_p) fracture terms (Equation (1)):

$$\frac{W_f}{B \cdot L} = w_e + \beta \cdot w_p \cdot L \tag{1}$$

where β [–] is a plastic zone shape dependent factor. It should be also noted that since in plane-stress the thickness has to be vanishingly small, the measured w_e and w_p are not true material constants, but functions of sheet thickness (B) [3, 5, 6].

In polymers, because of their particular macromolecular and visco-elastic nature, further questions have arisen. One problem is that one can only talk of true plastic deformation when there are no frozen in stresses [7]. As the majority of 'plastic' deformation in polymers is reversible at elevated temperatures, the question has to be reformulated, and one has to focus on the magnitude of reversibility and minimize the frozen in stresses. To achieve this, a polymer is needed, which can be easily deformed, has a low elastic modulus and yield stress; i.e. the crystals have low plastic resistance. By these characteristics the void formation and the cavitation can be diminished or cavitation will not appear at all [8]. Additionally, below glass transition temperature ($T < T_g$) the constrained elastic deformations are favored, and problems like cold-drawing [9, 10], physical aging [11] or free-volume decrease [12] of amorphous phase, interfere with the obtained results. Other viscous effects, like strain-rate dependence (see e.g. [9, 10, 13–15]) or strain-induced crystallization [16] can also frustrate the final consequences. Despite all of these, for amorphous polymers and for thermoplastic elastomers several tendencies have been deduced and partly explained; for details see [11, 17].

The influencing parameters of EWF for semi-crystalline thermoplastics, however, remain still uncertain. The reason is that several factors influence the structure and amount of crystalline phase and these are strongly interrelated. These include [18]: molecular structure, molecular weight and its distribution; crystalline phase and structure; the amount, order and orientation of crystalline fraction; spherulite size; lamellae thickness; chain branching; number and density of tie molecules; etc.

By starting with molecular structure and related glass transition temperature, the investigated materials can be divided into two groups. In studies performed (i) below glass transition temperature (see e.g. [19–22]) the previously mentioned entropy-elastic deformations dominate the failure, thus similar observations can be made than in case of amorphous thermoplastics and elastomers [17]. The other group of investigations includes materials, which were tested (ii) above their glass transition temperature, like polyethylenes [23, 24], polypropylenes [19, 20, 25–28], polyesters [21], poly(vinylidene-fluoride) [29], etc. In these polymers the cold-drawing in the amorphous glass is less significant and the effect of crystallinity can be emphasized.

The molecular weight dependence has been studied by Sheng *et al*. [27] on ethylene-propylene block copolymers with crystallinity change of less than 5%. They found that we increases linearly with the number average molecular weight (M_n). $\beta \cdot w_p$ was chiefly influenced by the amount of high molecular weight component; the increase of long-chain length fraction led to reduced ductility.

Mouzakis *et al*. [28] studied the effect of stereoregularity on the crystallinity and fracture properties of elastomeric polypropylene. It was found that we increases, but $\beta \cdot w_p$ decreases with decreasing crystallinity. Nevertheless, it should be noted that the molecular characteristics of samples were not presented.

Barry and Delatycki [30] showed in high density polyethylene that the thicker crystalline lamellae and the more ordered crystalline structure results in increased resistance to crack initiation. Conversely, the crack growth resistance decreased with increasing concentration of side chains.

Gupta *et al*. [24] studied the effect of side chain length on the deformation mechanisms of linear low density polyethylenes of similar molecular characteristics and crystallinity. They found that the longer the side chain the higher the essential work of fracture, which was explained by an anchoring effect of longer chain segments.

Channel and Clutton [31] studied the effect of molecular weight and chain branching in a series of polyethylenes under impact conditions and found that fracture toughness (G_c) increases linearly with increasing molecular weight. It was stated that the increase in molecular weight increases the number of tie molecules, that is accompanied by increased toughness [18].

Based on this literature overview it can be deduced that the raise in tie molecule density and lamellae thickness seem to increase the resistance to crack initiation and the value of w_e. The effect of crystallinity on w_e and the influencing factors of plastic work of fracture ($\beta \cdot w_p$) are, however, more obscure. This study is addressed to describe the fracture behavior of poly(ε-caprolactone) (PCL) as a function of molecular weight and crystalline morphology. As PCL at room temperature is well above its glass transition temperature ($T_g \approx -60$°C [32]), its amorphous phase has high compliance, which minimizes the magnitude of frozen in stresses, entropy-elastic deformation. Additionally, the reported problems like the orientation, physical aging [11, 33] or free-volume decrease [12] of amorphous glass phase do not interfere with the obtained results. The deformation in this state and at low deformation rates is assumed to be composed from the viscoplastic deformation of amorphous regions and the elasto-plastic deformation of crystalline spherulites.

To initiate the unloosening of crystallites one has to reach a critical stress, where the irreversible deformation starts. Men *et al*. [34] has shown that this critical stress is in connection with the intrinsic stability of crystals, which is related to their theoretical equilibrium melting temperature. The low melting temperature of PCL leads to the deformation of crystallites at lower stresses, compared to other semi-crystalline polyolefins, polyesters and this also helps to minimize the cold-drawing and orientation of amorphous network.

The micromechanical deformation of spherulitic crystalline phase, however, also has various subregions [35]. The crystalline lamellae first breaks into smaller blocks and those that are diagonally to the loading direction start to rotate and slip. As the deformability of crystalline lamellae is one order of magnitude smaller in the folding direction than perpendicular to it [7], the tearing of tie molecules is the dominant process in the equatorial regions, while in the polar directions the less stable structure promotes the unloosing of lamellar build-up.

The phase transition of crystalline parts also influences the fracture properties as it was reported by Ferrer-Balas *et al*. [25] for polypropylene. PCL, in contrast, has a stable orthorhombic ($P2_12_12_1$) crystalline structure with non-planar chain packing conformation in the crystalline lamellae [36, 37], thus these phase transitions have no effect on the fracture behavior either.

Summarily, PCL owing to its low melting and glass transition temperature, low yield stress, linear molecular and stable orthorhombic crystalline structure is in favorable state at room temperature to test the effect of molecular weight and crystalline phase on the essential work of fracture parameters of semi-crystalline polymers.

2. Experimental

2.1. Applied materials

For the studies four different poly(ε-caprolactone) (Perstorp Caprolactones, Perstorp UK Ltd, UK) samples were used. The molecular characteristics – number average molecular weight (M_n) and polydispersity (M_w/M_n) – were determined after compression moulding by size exclusion chromatography according to ISO 16014 in tetrahydrofuran at 35°C with a Waters chromatograph (Waters Corp., USA). The obtained results are listed in Table 1. The polydispersity values are comparable, thus the obtained results based on a specific molecular weight are comparable.

Table 1. Molecular characteristics of the examined PCLs

Name	Capa 6250	Capa 6400	Capa 6500	Capa 6800
M_n [kg/mol]	31.1	39.8	61.8	85.1
M_w/M_n [–]	1.6	1.6	1.7	1.9

M_n – number average molecular weight
M_w – weight average molecular weight

2.2. Sample processing

Tensile test specimens (ISO 527 type 1BA) and sheets with a thickness (B) of 0.5 mm were hot pressed using a COLLIN P-200E-type (Dr. Collin GmbH, Germany) compression molding machine at pressure of 5 MPa and temperature of 100°C. The samples were pre-heated for 5 minutes without load, followed by a 5 minute-hold under load and by water-cooling to room temperature with a rate of 10°C/min.

The fracture tests were performed on double edge notched tensile (DENT, Figure 1) specimens. Samples with a width (W) of 40 mm and length (H) of 80 mm (clamped length 40 mm) were machined from the sheets (B = 0.5 mm). The ligament lengths (L) varied between 4 and 13 mm and were prepared by aligned razor blades. The ligament lengths were measured by an optical microscope (Olympus BX 51M, Olympus Corp., Japan) prior testing.

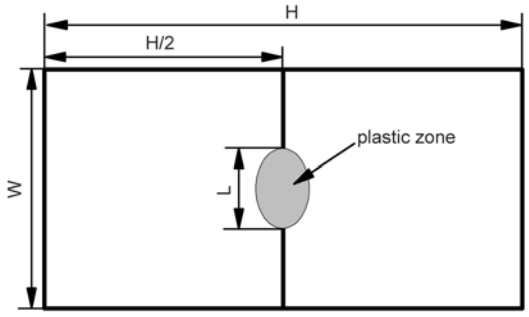

Figure 1. Geometry of DENT specimens

2.3. Analytical techniques

The rheological properties of PCL melts were determined using a plate-plate rheometer (AR2000; TA Instruments, USA) at 100°C in the shear-rate range of 0.01 and 5 1/s. The zero-shear viscosity (η_0) was determined from the shear-rate versus dynamic-viscosity curves by assuming Newtonian behavior.

Wide-angle X-ray diffraction (WAXD) measurements were performed on compression molded sheets and on the deformed ligament region of DENT specimens. The patterns were recorded on X'pert PRO MPD (PANalytical B.V., The Netherlands) X-ray diffractometer equipped with an X'Celerator detector and using Cu K_α radiation (λ = 0.1542 nm).

Differential scanning calorimetry (DSC) was carried out on the samples by a Mettler-Toledo DSC1 (Mettler-Toledo GmbH, Switzerland). The purge gas was nitrogen (30 mL/min), while liquid nitrogen was used for the cooling. The measurements were carried out between –30 and 100°C with a heating and cooling rate of 10°C/min. The results were evaluated according to ISO 11357-3 standard. The crystallinity of the samples was calculated by taking the enthalpy of fusion of the 100% crystalline polymer as ΔH_0 = 142.5 J/g [38].

The tensile and fracture tests were performed at ambient conditions (24±1°C, RH = 40±5%) on a Zwick Z020 (Zwick GmbH, Germany) universal testing machine. The crosshead speed was set to 10 mm/min, the displacement values were calculated from crosshead travel, while the force values were recorded by a 20 kN loading cell. For the determination of tensile properties five dumb-bell specimens were tested for each material. For the linear regression of EWF data at least 20 specimens were used.

2.4. EWF method and the data limitation of concept

Based on Equation (1) the linear regression of specific work of fracture ($w_f = W_f/(L \cdot B)$) versus ligament length (L) plots yields in the specific essential work of fracture (w_e) – ordinate intercept – and in the plastic work of fracture (βw_p) – the slope of the fitted line. However, Equation (1) is only valid if the prerequisites of EWF method are met. Under mode I load – tests on double edge notched tensile specimens (DENT; Figure 1.) – these conditions are:

- full ligament yielding prior to crack initiation,
- quasi plane-stress conditions during crack propagation,
- confined plastic zone,
- geometrical similarity of specimens.

There are several empirical and theoretical criteria that help to ensure the above mentioned conditions (see e.g. [4, 11, 39, 40]), but the adequacy of these criteria still remains a relevant issue [41–43]. In this paper – based on previous studies [41–43] – the following prerequisites have been used:

- necking of the fracture process zone
- self-similarity of load-displacement curves (see Figure 2),
- a lower ligament limit, which was determined as outlined in our previous paper [43] to ensure quasi plane-stress conditions and steady-state crack propagation,
- a confined plastic zone was ensured by the condition $L < \mathrm{Min}(W/3, x_p)$ [11], where x_p is the esti-

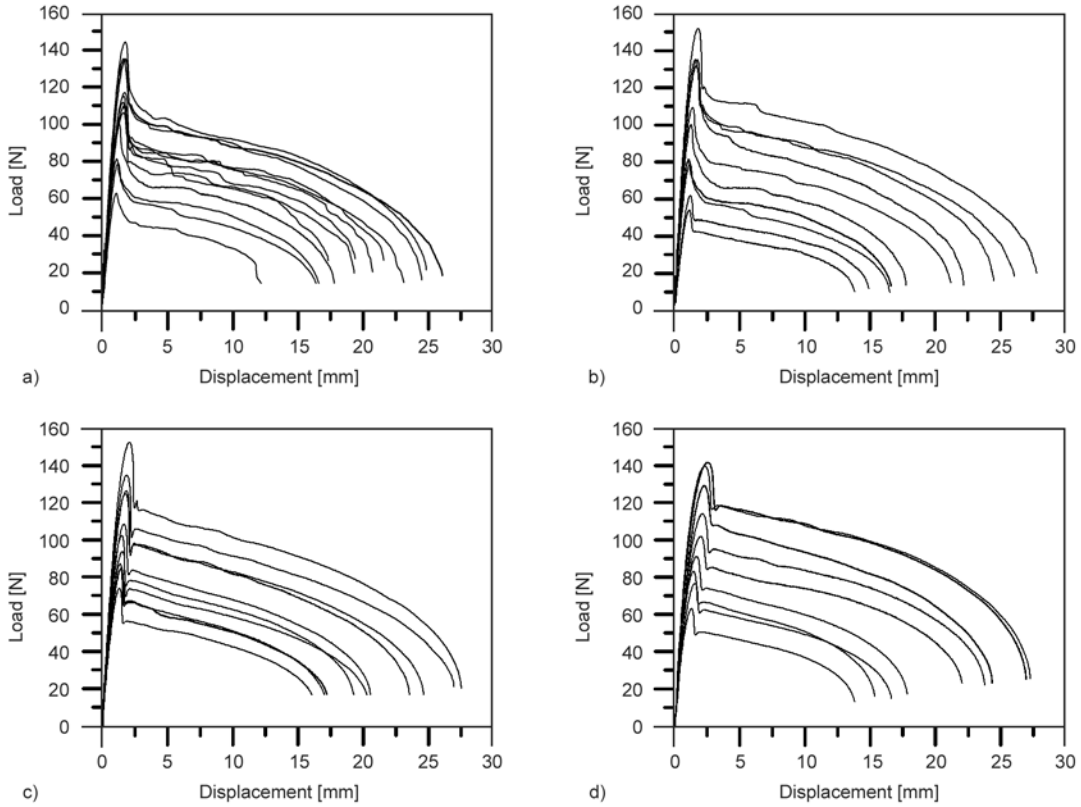

Figure 2. Characteristic load-displacement curves of the studied DENT samples: (a) Capa 6250, (b) Capa 6400, (c) Capa 6500 and (d) Capa 6800

mated size of the plastic zone based on Cotterell's study [4], and
– ligament yielding was verified by the method described in [42].

3. Results and discussion

3.1. Morphology of amorphous and crystalline phase

The zero-shear viscosity (η_0) of polymer melts is proportional to the molecular weight (M_n), i.e. to the number of backbone atoms [44]. This dependence can be described by Equation (2):

$$\eta_0 \propto M_n \alpha \tag{2}$$

where α is an exponential factor having a value of $1 < \alpha < 2.5$ for polymers below a critical molecular weight (M_c) [45], and $\alpha = 3.4$ for materials above their M_c.

This critical molecular weight has been interpreted as the molecular weight required for the formation of entanglements [44]. Based on Equation (2) the $\log \eta_0$ versus $\log M_n$ plot shown in Figure 3 yields in $\alpha = 3.41$ ($R^2 = 0.98$), which confirms the presence of entangled amorphous network in the studied materials.

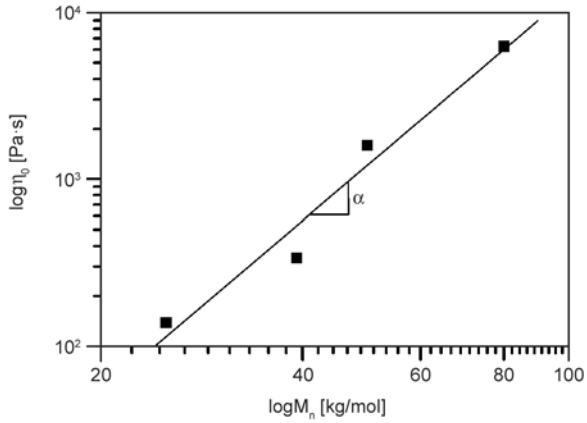

Figure 3. Zero-shear-viscosity as a function of number average molecular weight for PCL samples

The WAXD plots (Figure 4) indicate that the PCLs of different molecular weight have the same crystalline structure prior to mechanical testing so the results are comparable and are not influenced by artifacts resulting from different crystalline arrangements.

As it was shown by Skoglund and Fransson [46] bulk PCL crystallizes in spherulitic morphology

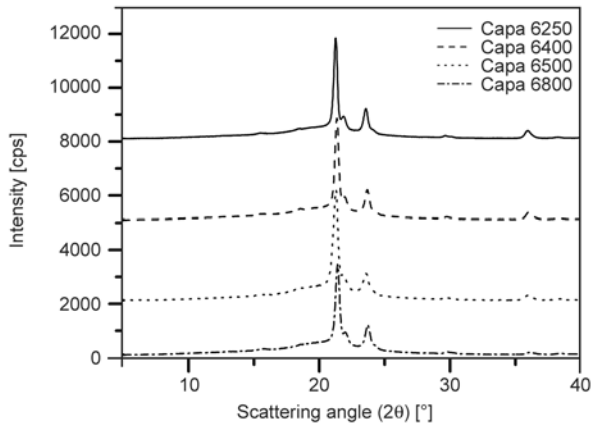

Figure 4. WAXD plots of PCLs with different molecular characteristics

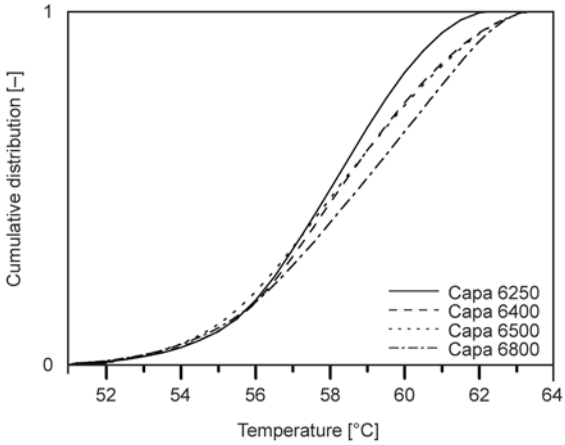

Figure 6. Cumulative distribution of crystalline lamellae with different melting temperatures

independent of the crystallization procedure. They also reported that the crystallization is nucleation controlled and the kinetics is slower for higher molecular weight samples. The slower kinetics can be explained with the retarded segmental mobility of the longer chains. As a result of this the crystallinity decreases with increasing M_n. The crystallization peak temperature was 29±1°C for the materials investigated, thus the degree of supercooling can be taken as constant. In Figure 5 it is observable that the obtained crystallinity values are in good agreement with the results of Skoglund and Franson [46] and Pitt *et al*. [47]. At high molecular weights the crystallinity is about 40%, rising to around 75% as the M_n decreases to ~10 kg/mol.

According to the Thomson-Gibbs equation [48] the melting temperature (T_m) of a crystallite is related to its lamellar thickness (D) (Equation (3)):

$$T_m \propto T_m^0\left(1 - \frac{1}{D}\right) \tag{3}$$

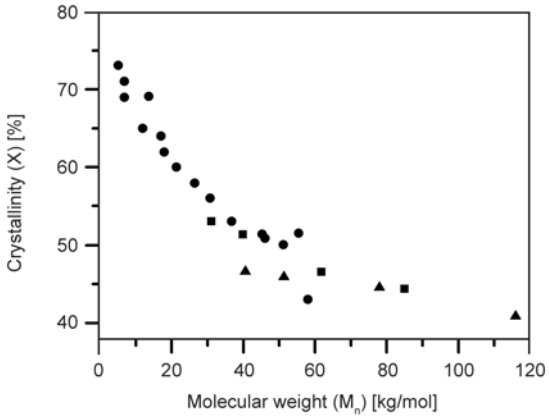

Figure 5. Relationship between the crystallinity and the molecular weight of PCL (● – Pitt *et al*. [47], ▲ – Skoglund and Franson [46] ■ – this study)

As T_m^0 is practically independent of molecular weight for the examined materials – it was shown by Chen *et al*. [49] that above $M_n \approx 20$ kg/mol the theoretical equilibrium melting point (T_m^0) of PCL can be taken as constant –, the lamellar thickness distribution can be estimated from the DSC melting endotherms as shown in Figure 6. The above mentioned difference in folding kinetics did not result in a considerable deviation of melting temperatures, i.e. lamellae thickness.

As it is shown in Figure 7 neither the onset (T_{on}) and end temperatures (T_{end}) nor the peak temperatures (T_{mp}) differ significantly ($p < 0.05$). Only the amount of crystalline phase (X) decreases with increasing molecular weight, which is a result of retarded chain mobility of longer molecules.

To summarize, PCL seems to be a rational model material to investigate the effect of molecular weight induced crystallinity changes on the fracture properties. The change in molecular characteristics influences the amount of crystalline fraction and the

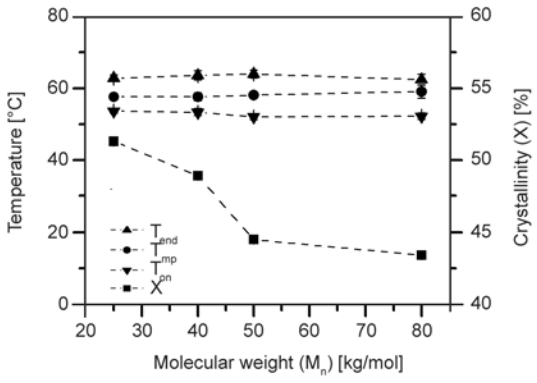

Figure 7. Melting characteristics of PCL as a function of molecular weight

density of tie molecules, entanglements only. The crystalline structure, order and lamellae thickness appear to be independent of examined molecular weight range, while there is no preferred orientation in the crystalline structure due to the sample processing method.

Nevertheless, the reduced segmental mobility of longer molecules led to decreasing crystallinity.The increase in molecular weight also increases the entanglement density of amorphous phase. Additionally the longer molecules could cross several crystalline lamellae, thus the tie molecule density of higher molecular weight samples also increases. As a consequence, the interconnectivity of amorphous and crystalline 'networks' grows with increasing molecular weight.

3.2. Mechanical properties

In PCL the low glass transition temperature and the less stable crystalline structure result in highly ductile deformation under ambient conditions. Owing to the relatively slow deformation rate, the tensile specimens did not fail up to an elongation of 200%. As the specimen end regions yielded at these high deformations, the elongation at break and engineering break stress values could not be determined (see ISO 527).

As it is shown in Table 2, the Young's modulus (E) and yield stress (σ_Y) values decrease, while the elongation at yield (ε_Y) rises with increasing molecular weight. The descending modulus, yield stress as well as the growing elongation at yield values are indicative of a less rigid, more compliant structure. This can be explained by the influence of crystallinity, i.e. by the amount of stiff crystalline phase. As the studied PCL is well above its glass transition temperature the amorphous phase has mainly stress transferring role and the load is chiefly carried by the interconnected crystalline network. However, to support this hypothesis one has to eliminate the influence of the amount of crystalline phase.

By normalizing the measured tensile properties with crystallinity (Figure 8) it is observable that above 40 kg/mol the normalized tensile modulus

Table 2. Tensile characteristics of the examined materials

Name	Capa 6250	Capa 6400	Capa 6500	Capa 6800
E [MPa]	429±41	348±19	310±41	295±4
σ_Y [MPa]	16.7±0.7	14.5±0.1	13.2±0.4	12.8±0.2
ε_Y [%]	9.6±0.7	11.9±0.3	12.2±1.2	14.7±0.3

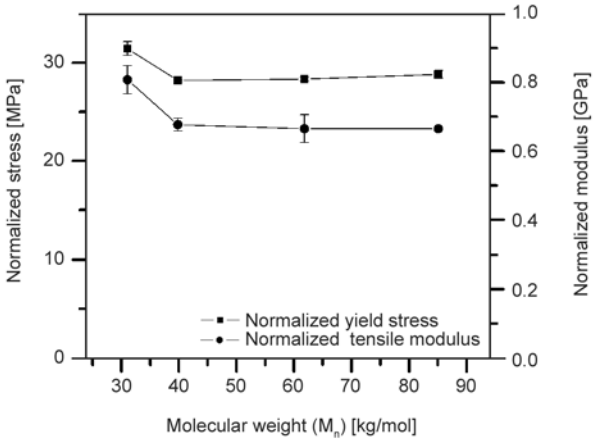

Figure 8. Normalized tensile properties as a function of number average molecular weight

(E/X) and yield stress (σ_Y/X) values are independent of molecular weight ($p < 0.05$). This observation suggests that during tensile tests the molecule length, the number of entanglements and tie molecules in amorphous regions do not influence the deformability of crystalline phase.

The only exception is the low molecular weight sample (Capa 6250). It should be noted, however, that this polymer can be annealed at room temperature. This process is rather fast, and several hours of 'annealing' – delay between the measurements of crystallinity and mechanical properties – may lead to significant changes in the crystalline structure, crystallinity and mechanical properties [50]. Therefore, this point is treated as an artefact.

After yielding, the unloosing of crystalline structure led to decreasing crystallinity as it is shown on the WAXD plots of Figure 9. The broadening of WAXD peaks also suggests the deformation of crystalline structure [51].

From the full-width-at-half-maximum (FWHM) values of reflections of (110) plane [37] one can derive information about the mean lateral dimension of the crystallites. As the Scherrer-equation says the mean lateral dimension of the crystallites of a polycrystalline sample is inversely proportional to the full-width-at-half-maximum of a diffraction peak (at a given θ scattering angle and λ wavelength). In Capa 6250 only a slight increase of FWHM was observed – negligible rearrangement of crystallites during the deformation –, however, in higher molecular weight samples the change was more significant (Figure 9b). The mean lateral dimension values were only the third of their initial value, which suggests more intense deformations, crystalline-

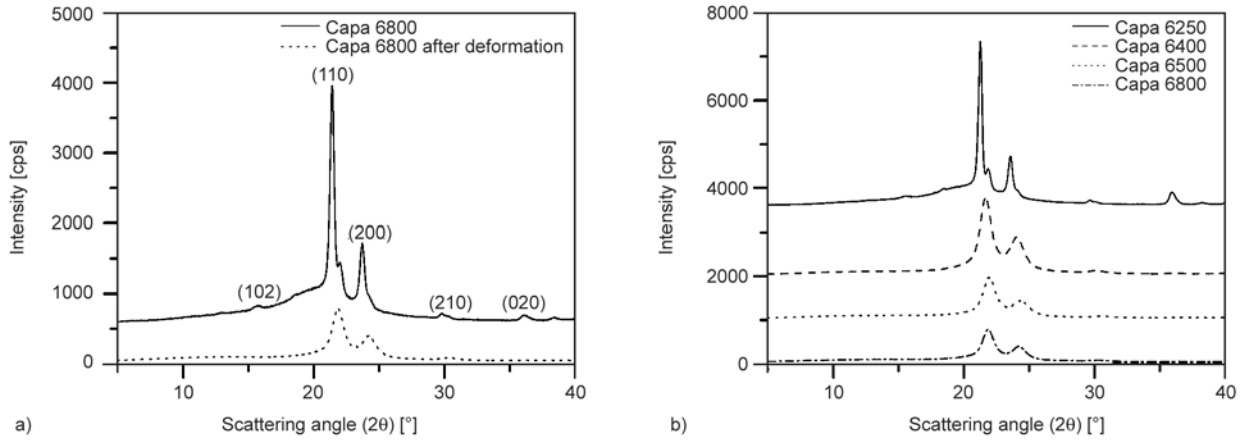

Figure 9. WAXD plots of (a) undeformed and deformed Capa 6800 and (b) deformed PCLs as a function of molecular weight (DENT specimens)

size-refinement and the unloosing of crystalline domains.

Table 3 summarizes the obtained work of fracture parameters for different molecular weight PCLs. All samples fulfilled the requirements outlined in Section 2.4. As a result of enhanced tie molecule and entanglement density (Figure 3) the essential work of fracture terms increase with molecular weight. Additionally, the longer molecules are able to form more secondary bonds, thus the initiation of unloosing and tearing of polymer chain from crystalline lamellae also consumes more energy and raises the essential work of fracture.

After plotting the essential work of fracture values as a function of molecular weight the data lie on a line with positive intercept ($R^2 = 0.9670$), as it was observed by Sheng *et al*. [27] during EWF tests on polyethylene-polypropylene block copolymers, or by Channel and Clutton [31] during impact fracture tests. The goodness of fit can be further improved after incorporating the effect of crystallinity in a same way as done in tensile tests. The regression coefficient of normalized essential work of fracture versus molecular weight line increases to a remarkable $R^2 = 0.9954$ (Figure 10). This correlation can be described by Equation (4):

Table 3. Effect of molecular weight on fracture parameters and the parameters of linear fit

Name	w_e [kJ/m^2]	$\beta \cdot w_p$ [MJ/m^3]	R^2 [–]	SD [kJ/m^2]
Capa 6250	45.7±3.2	19.9±0.4	0.9901	5.2
Capa 6400	48.3±4.4	27.6±0.5	0.9951	6.3
Capa 6500	50.5±5.1	21.9±0.6	0.9891	6.7
Capa 6800	55.9±2.2	16.5±0.2	0.9955	3.4

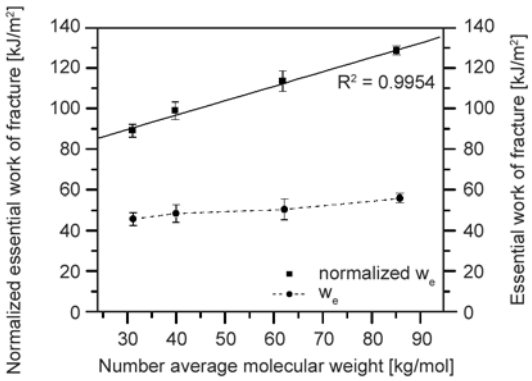

Figure 10. Essential work of fracture versus number average molecular weight plots of PCL

$$w_e = (w_{e0} + a \cdot M_n) \cdot X \quad (4)$$

where w_{e0} [kJ/m^2] is the intrinsic essential work of fracture, which could be a material dependent parameter, a [kJ·mol/kg·m^2] is a variable depending on the entanglement and tie molecule density of a specific material, M_n [kg/mol] is the number average molecular weight and X [–] is the crystallinity. For PCL the constant values are $a = 0.713$ kJ·mol/kg·m^2 and $w_{e0} = 68.7$ kJ/m^2.

The dissipative component originates mainly from the various slips and rotations of crystalline blocks and from the unloosing of chain segments in the outer dissipative volume of the fracture ($\beta \cdot B \cdot L^2$). The related work of fracture parameter ($\beta \cdot w_p$) has a maximum between $M_n = 40$ and 60 kg/mol. This observation could be explained by the opposing effects of crystalline build up, crystallinity and amorphous phase entanglement density, respectively.

At low molecular weights, the less entangled amorphous network, the shorter tie molecules facilitate the rotation and slip of crystalline blocks, while the

higher crystallinity – stiffer network – hinder the energy dissipative deformations (small $\beta \cdot w_p$ values). As a result, the unloosing of crystalline network was nearly absent in the Capa 6250 sample (see Figure 9b). With growing molecular weight the crystallinity drops, the compliance of crystalline phase increases, it can be deformed easier and $\beta \cdot w_p$ also increases (Capa 6400 and 6500). This observation is in contrast with the findings of Mouzakis *et al*. [28]; however the molecular charateristics of the samples studied are not known.

On the other hand, at high molecular weights the crystallinity remains nearly constant (for M_n higher than ~60 kg/mol, see Figure 5), but the rising entanglement density of amorphous network acts as a barrier for the energy dissipative mechanisms, leading to the decrease of $\beta \cdot w_p$ (Capa 6800), similarly as found by Sheng *et al*. [27].

4. Conclusions

The molecular weight and crystallinity dependence of essential work of fracture of semi-crystalline poly(ε-caprolactone) (PCL) have been characterized in this study. Based on wide angle X-ray diffraction and differential scanning calorimetric measurements, the crystalline structure and lamellae thickness distribution were found to be independent of molecular weight, only the crystallinity decreased as a result of slower kinetics of longer molecules.

The tensile mechanical properties were mainly governed by the amount of load-carrying crystalline phase; the amorphous regions acted chiefly as stress transferring zones. The Young's modulus and yield stress of samples decreased with increasing molecular weight and crystallinity, but after normalizing with crystallinity they had a constant value.

The fracture behavior was studied by the essential work of fracture method, which is suitable for the description of the fracture of thin ductile materials under quasi plane stress conditions. The plastic deformation and unloosening of crystalline structure has been confirmed by wide angle X-ray diffraction measurements. The essential work of fracture – work required for the generation of new crack-surfaces – increased with increasing molecular weight as a result of increasing tie molecule length and density. After normalizing with crystallinity linear correlation was found between the normalized essential work of fracture and number average molecular weight.

The decrease of tie molecule density and the raise of either the crystallinity or the entanglement density of amorphous network acted as a barrier in relation to the plastic fracture work – dissipated energy in the plastic zone. As a result the non-essential work of fracture had a maximum between M_n = 40 and 60 kg/mol, where these counteractive effects were in balance.

Acknowledgements

The authors are indebted to János Madarász (Department of Inorganic and Analytical Chemistry, Budapest University of Technology and Economics) for his help in the X-ray diffraction measurements. This work is connected to the scientific program of the 1Development of quality-oriented and harmonized R+D+I strategy and functional model at BME1 (Project ID: TÁMOP-4.2.1/B-09/1/KMR-2010-0002) and the 'Talent care and cultivation in the scientific workshops of BME' (Project ID: TÁMOP - 4.2.2.B-10/1--2010-0009) projects.

References

[1] Zerbst U., Heinimann M., Donne C. D., Steglich D.: Fracture and damage mechanics modelling of thin-walled structures – An overview. Engineering Fracture Mechanics, **76**, 5–43 (2009). DOI: 10.1016/j.engfracmech.2007.10.005

[2] Schwalbe K-H., Newman Jr J. C., Shannon Jr J. L.: Fracture mechanics testing on specimens with low constraint–standardisation activities within ISO and ASTM. Engineering Fracture Mechanics, **72**, 557–576 (2005). DOI: 10.1016/j.engfracmech.2004.04.006

[3] Cotterell B., Reddel J. K.: The essential work of plane stress ductile fracture. International Journal of Fracture, **13**, 267–277 (1977). DOI: 10.1007/BF00040143

[4] Cotterell B., Pardoen T., Atkins A. G.: Measuring toughness and the cohesive stress–displacement relationship by the essential work of fracture concept. Engineering Fracture Mechanics, **72**, 827–848 (2005). DOI: 10.1016/j.engfracmech.2004.10.002

[5] Hill R.: On discontinuous plastic states, with special reference to localized necking in thin sheets. Journal of the Mechanics and Physics of Solids, **1**, 19–30 (1952). DOI: 10.1016/0022-5096(52)90003-3

[6] Pardoen T., Marchal Y., Delannay F.: Thickness dependence of cracking resistance in thin aluminium plates. Journal of the Mechanics and Physics of Solids, **47**, 2093–2123 (1999). DOI: 10.1016/S0022-5096(99)00011-3

[7] Kausch H. H.: Polymer fracture. Springer Verlag, Heidelberg (1978).

[8] Pawlak A., Galeski A.: Plastic deformation of crystalline polymers: The role of cavitation and crystal plasticity. Macromolecules, **38**, 9688–9697 (2005). DOI: 10.1021/ma050842o

[9] Karger-Kocsis J., Czigány T., Moskala E. J.: Deformation rate dependence of the essential and non-essential work of fracture parameters in an amorphous copolyester. Polymer, **39**, 3939–3944 (1998). DOI: 10.1016/S0032-3861(98)00029-9

[10] Karger-Kocsis J., Moskala E. J.: Molecular dependence of the essential and non-essential work of fracture of amorphous films of poly(ethylene-2,6-naphthalate) (PEN). Polymer, **41**, 6301–6310 (2000). DOI: 10.1016/S0032-3861(99)00866-6

[11] Bárány T., Czigány T., Karger-Kocsis J.: Application of the essential work of fracture (EWF) concept for polymers, related blends and composites: A review. Progress in Polymer Science, **35**, 1257–1287 (2010). DOI: 10.1016/j.progpolymsci.2010.07.001

[12] Gámez-Pérez J., Velazquez-Infante J. C., Franco-Urquiza E., Pages P., Carrasco F., Santana O. O., Maspoch M. L.: Fracture behavior of quenched poly(lactic acid). Express Polymer Letters, **5**, 82–91 (2011). DOI: 10.3144/expresspolymlett.2011.9

[13] Maspoch M. L., Gámez-Pérez J., Karger-Kocsis J.: Effects of thickness, deformation rate and energy partitioning on the work of fracture parameters of uPVC films. Polymer Bulletin, **50**, 279–286 (2003). DOI: 10.1007/s00289-003-0169-5

[14] Ching E. C. Y., Li R. K. Y., Mai Y-W.: Effects of gauge length and strain rate on fracture toughness of polyethylene terephthalate glycol (PETG) film using the essential work of fracture analysis. Polymer Engineering and Science, **40**, 310–319 (2000). DOI: 10.1002/pen.11164

[15] Ching E. C. Y., Poon W. K. Y., Li R. K. Y., Mai Y-W.: Effect of strain rate on the fracture toughness of some ductile polymers using the essential work of fracture (EWF) approach. Polymer Engineering and Science, **40**, 2558–2568 (2000). DOI: 10.1002/pen.11386

[16] Chen H., Karger-Kocsis J., Wu J.: Effects of molecular structure on the essential work of fracture of amorphous copolyesters at various deformation rates. Polymer, **45**, 6375–6382 (2004). DOI: 10.1016/j.polymer.2004.07.007

[17] Chen H., Wu J.: Understanding the underlying physics of the essential work of fracture on the molecular level. Macromolecules, **40**, 4322–4326 (2007). DOI: 10.1021/ma062567r

[18] Karger-Kocsis J.: Dependence of the fracture and fatigue performance of polyolefins and related blends and composites on microstructural and molecular characteristics. Macromolecular Symposia, **143**, 185–205 (1999). DOI: 10.1002/masy.19991430115

[19] Ferrer-Balas D., Maspoch M. L., Mai Y-W.: Fracture behaviour of polypropylene films at different temperatures: Fractography and deformation mechanisms studied by SEM. Polymer, **43**, 3083–3091 (2002). DOI: 10.1016/S0032-3861(02)00102-7

[20] Ferrer-Balas D., Maspoch M. L., Martinez A. B., Ching E., Li R. K. Y., Mai Y-W.: Fracture behaviour of polypropylene films at different temperatures: Assessment of the EWF parameters. Polymer, **42**, 2665–2674 (2001). DOI: 10.1016/S0032-3861(00)00603-0

[21] Hashemi S., Arkhireyeva A.: Influence of temperature on work of fracture parameters in semi-crystalline polyester films. Journal of Macromolecular Science Part B: Physics, **41**, 863–880 (2002). DOI: 10.1081/MB-120013070

[22] Hashemi S.: Temperature dependence of work of fracture parameters in polybutylene terephthalate (PBT). Polymer Engineering and Science, **40**, 1435–1446 (2000). DOI: 10.1002/pen.11273

[23] Pegoretti A., Castellani L., Franchini L., Mariani P., Penati A.: On the essential work of fracture of linear low-density-polyethylene. I. Precision of the testing method. Engineering Fracture Mechanics, **76**, 2788–2798 (2009). DOI: 10.1016/j.engfracmech.2009.05.013

[24] Gupta P., Wilkes G. L., Sukhadia A. M., Krishnaswamy R. K., Lamborn M. J., Wharry S. M., Tso C. C., DesLauriers P. J., Mansfield T., Beyer F. L.: Does the length of the short chain branch affect the mechanical properties of linear low density polyethylenes? An investigation based on films of copolymers of ethylene/1-butene, ethylene/1-hexene and ethylene/1-octene synthesized by a single site metallocene catalyst. Polymer, **46**, 8819–8837 (2005). DOI: 10.1016/j.polymer.2005.05.137

[25] Ferrer-Balas D., Maspoch M. L., Martinez A. B., Santana O. O.: Influence of annealing on the microstructural, tensile and fracture properties of polypropylene films. Polymer, **42**, 1697–1705 (2001). DOI: 10.1016/S0032-3861(00)00487-0

[26] Karger-Kocsis J.: Toward understanding the morphology-related crack initiation and propagation behavior in polypropylene systems as assessed by the essential work of fracture approach. Journal of Macromolecular Science Part B: Physics, **38**, 635–646 (1999). DOI: 10.1080/00222349908248127

[27] Sheng B-R., Li B., Xie B-H., Yang W., Feng J-M., Yang M-B.: Influences of molecular weight and crystalline structure on fracture behavior of controlled-rheology-polypropylene prepared by reactive extrusion. Polymer Degradation and Stability, **93**, 225–232 (2008). DOI: 10.1016/j.polymdegradstab.2007.09.011

[28] Mouzakis D. E., Gahleitner M., Karger-Kocsis J.: Toughness assessment of elastomeric polypropylene (ELPP) by the essential work of the fracture method. Journal of Applied Polymer Science, **70**, 873–881 (1998).
DOI: 10.1002/(SICI)1097-4628(19981031)70:5<873::AID-APP6>3.0.CO;2-Q

[29] Wallner G. M., Major Z., Maier G. A., Lang R. W.: Fracture analysis of annealed PVDF films. Polymer Testing, **27**, 392–402 (2008).
DOI: 10.1016/j.polymertesting.2008.01.006

[30] Barry D. B., Delatycki O.: The effect of molecular structure and polymer morphology on the fracture resistance of high-density polyethylene. Polymer, **33**, 1261–1265 (1992).
DOI: 10.1016/0032-3861(92)90772-O

[31] Channell A. D., Clutton E. Q.: The effects of short chain branching and molecular weight on the impact fracture toughness of polyethylene. Polymer, **33**, 4108–4112 (1992).
DOI: 10.1016/0032-3861(92)90613-2

[32] Wunderlich B.: Thermal analysis of polymeric materials. Springer, Berlin (2005).

[33] Bárány T., Ronkay F., Karger-Kocsis J., Czigány T.: In-plane and out-of-plane fracture toughness of physically aged polyesters as assessed by the essential work of fracture (EWF) method. International Journal of Fracture, **135**, 251–265 (2005).
DOI: 10.1007/s10704-005-3947-2

[34] Men Y., Rieger J., Strobl G.: Role of the entangled amorphous network in tensile deformation of semicrystalline polymers. Physical Review Letters, **91**, 095502/1–095502/4 (2003).
DOI: 10.1103/PhysRevLett.91.095502

[35] Michler G. H.: Kunststoff-Mikromechanik. Hanser, München (1992).

[36] Hu H., Dorset D. L.: Crystal structure of poly(iε-caprolactone). Macromolecules, **23**, 4604–4607 (1990).
DOI: 10.1021/ma00223a017

[37] Zhang Y., Leblanc-Boily V., Zhao Y., Prud'homme R.E.: Wide angle X-ray diffraction investigation of crystal orientation in miscible blend of poly(ε-caprolactone)/poly(vinyl chloride) crystallized under strain. Polymer, **46**, 8141–8150 (2005).
DOI: 10.1016/j.polymer.2005.06.114

[38] Crescenzi V., Manzini G., Calzolari G., Borri C.: Thermodynamics of fusion of poly-β-propiolactone and poly-ε-caprolactone. comparative analysis of the melting of aliphatic polylactone and polyester chains. European Polymer Journal, **8**, 449–463 (1972).
DOI: 10.1016/0014-3057(72)90109-7

[39] Marchal Y., Walhin J-F., Delannay F.: Statistical procedure for improving the precision of the measurement of the essential work of fracture of thin sheets. International Journal of Fracture, **87**, 189–199 (1997).
DOI: 10.1023/A:1007482121146

[40] Clutton E.: Essential work of fracture. European Structural Integrity Society, **28**, 177–195 (2001).
DOI: 10.1016/S1566-1369(01)80033-9

[41] Tuba F., Oláh L., Nagy P.: Essential work of fracture study of polymers: A novel criterion for the validation of tested ligament range. Journal of Materials Science, **46**, 7901–7904 (2011).
DOI: 10.1007/s10853-011-5778-z

[42] Tuba F., Oláh L., Nagy P.: On the valid ligament range of specimens for the essential work of fracture method: The inconsequence of stress criteria. Engineering Fracture Mechanics, **99**, 349–355 (2013).
DOI: 10.1016/j.engfracmech.2012.12.011

[43] Tuba F., Oláh L., Nagy P.: The role of ultimate elongation in the determination of valid ligament range of essential work of fracture tests. Journal of Materials Science, **47**, 2228–2233 (2012).
DOI: 10.1007/s10853-011-6033-3

[44] Macosko C. W.: Rheology: Principles, measurements and applications. Wiley-VCH, Weinheim (1994).

[45] Izuka A., Winter H. H., Hashimoto T.: Molecular weight dependence of viscoelasticity of polycaprolactone critical gels. Macromolecules, **25**, 2422–2428 (1992).
DOI: 10.1021/ma00035a020

[46] Skoglund P., Fransson Å.: Continuous cooling and isothermal crystallization of polycaprolactone. Journal of Applied Polymer Science, **61**, 2455–2465 (1996).
DOI: 10.1002/(SICI)1097-4628(19960926)61:13<2455::AID-APP25>3.0.CO;2-1

[47] Pitt C. G., Chasalow F. I., Hibionada Y. M., Klimas D. M., Schindler A.: Aliphatic polyesters. I. The degradation of poly(ε-caprolactone) in vivo. Journal of Applied Polymer Science, **26**, 3779–3787 (1981).
DOI: 10.1002/app.1981.070261124

[48] Bodor G.: Structural investigation of polymers. Ellis Horwood, New York (1991).

[49] Chen H-L., Li L-J., Ou-Yang W-C., Hwang J. C., Wong W-Y.: Spherulitic crystallization behavior of poly(ε-caprolactone) with a wide range of molecular weight. Macromolecules, **30**, 1718–1722 (1997).
DOI: 10.1021/ma960673v

[50] Tuba F.: Fracture tougness – microstructure relationships in biodegradable medical polymers. PhD Thesis in 'Department of Polymer Engineering, Budapest University of Technology and Economics', Budapest (2012).

[51] Dinnebier R. E., Billinge S. J. L.: Powder diffraction – Theory and practice. The Royal Society of Chemistry, Cambridge (2008).